University of California
Santa Barbara

Heterogeneous integration for silicon nitride photonics

A dissertation submitted in partial satisfaction
of the requirements for the degree

Doctor of Philosophy
in
Electrical and Computer Engineering

by

Chao Xiang

Committee in charge:

Professor John E. Bowers, Chair
Professor Larry A. Coldren
Professor Jonathan Klamkin
Doctor Paul A. Morton

June 2021

The Dissertation of Chao Xiang is approved.

Professor Larry A. Coldren

Professor Jonathan Klamkin

Doctor Paul A. Morton

Professor John E. Bowers, Committee Chair

May 2021

Heterogeneous integration for silicon nitride photonics

by

Chao Xiang

To my beloved family.

Acknowledgements

It has been an incredible PhD journey in Santa Barbara. I want to express my sincere thanks to my supervisor Prof John Bowers, my committee members Prof. Larry Coldren, Prof. Jonathan Klamkin, Dr. Morton and the Bowers Group. And I want to thank Dr. Gordon Keeler and DARPA for the generous funding support (DODOS and Morton STTR projects) which made this thesis possible.

Curriculum Vitæ

Chao Xiang

Education

2021	Ph.D. in Electrical and Computer Engineering (Expected), University of California, Santa Barbara.
2015	M.Phil. in Information Engineering, the Chinese University of Hong Kong.
2012	B.E. in Optoelectronic Engineering, Huazhong University of Science and Technology.

Publications

Journal Articles

1. C. Xiang, J. Guo, W. Jin, J. Peters, W. Xie, L. Chang, B. Shen, H. Wang, Q.-F. Yang, L. Wu, *et. al.*, *High-performance lasers for fully integrated silicon nitride photonics*, *arXiv preprint arXiv:2104.08414* (2021)

2. C. Xiang, J. Liu, J. Guo, L. Chang, R. N. Wang, W. Weng, J. Peters, W. Xie, Z. Zhang, J. Riemensberger, *et. al.*, *Laser soliton microcombs on silicon*, *arXiv preprint arXiv:2103.02725* (2021)

3. C. Xiang, W. Jin, J. Guo, C. Williams, A. M. Netherton, L. Chang, P. A. Morton, and J. E. Bowers, *Effects of nonlinear loss in high-Q Si ring resonators for narrow-linewidth III-V/Si heterogeneously integrated tunable lasers*, *Optics Express* **28** (2020), no. 14 19926–19936

4. C. Xiang, W. Jin, J. Guo, J. D. Peters, M. J. Kennedy, J. Selvidge, P. A. Morton, and J. E. Bowers, *Narrow-linewidth III-V/Si/Si_3N_4 laser using multilayer heterogeneous integration*, *Optica* **7** (Jan, 2020) 20–21

5. C. Xiang, P. A. Morton, and J. E. Bowers, *Ultra-narrow linewidth laser based on a semiconductor gain chip and extended Si_3N_4 Bragg grating*, *Optics Letters* **44** (2019), no. 15 3825–3828

6. C. Xiang, M. L. Davenport, J. B. Khurgin, P. A. Morton, and J. E. Bowers, *Low-loss continuously tunable optical true time delay based on Si_3N_4 ring resonators*, *IEEE Journal of Selected Topics in Quantum Electronics* **24** (2017), no. 4 1–9

7. C. Xiang, M. A. Tran, T. Komljenovic, J. Hulme, M. Davenport, D. Baney, B. Szafraniec, and J. E. Bowers, *Integrated chip-scale Si_3N_4 wavemeter with narrow free spectral range and high stability*, *Optics Letters* **41** (2016), no. 14 3309–3312

8. N. Margalit, C. Xiang, S. M. Bowers, A. Bjorlin, R. Blum, and J. E. Bowers, *Perspective on the future of silicon photonics and electronics*, *Applied Physics Letters* (in press)

9. T. C. Briles, S.-P. Yu, L. Chang, C. Xiang, J. Guo, D. Kinghorn, G. Moille, K. Srinivasan, J. E. Bowers, and S. B. Papp, *Hybrid InP and SiN integration of an octave-spanning frequency comb*, *APL Photonics* **6** (2021), no. 2 026102

10. Z. Du, C. Xiang, T. Fu, M. Chen, S. Yang, J. E. Bowers, and H. Chen, *Silicon nitride chirped spiral Bragg grating with large group delay*, *APL Photonics* **5** (2020), no. 10 101302

11. L. Stern, W. Zhang, L. Chang, J. Guo, C. Xiang, M. A. Tran, D. Huang, J. D. Peters, D. Kinghorn, J. E. Bowers, *et. al.*, *Ultra-precise optical-frequency stabilization with heterogeneous III-V/Si lasers*, *Optics Letters* **45** (2020), no. 18 5275–5278

12. B. Shen, L. Chang, J. Liu, H. Wang, Q.-F. Yang, C. Xiang, R. N. Wang, J. He, T. Liu, W. Xie, *et. al.*, *Integrated turnkey soliton microcombs*, *Nature* **582** (2020), no. 7812 365–369

13. L. Chang, W. Xie, H. Shu, Q.-F. Yang, B. Shen, A. Boes, J. D. Peters, W. Jin, C. Xiang, S. Liu, *et. al.*, *Ultra-efficient frequency comb generation in AlGaAs-on-insulator microresonators*, *Nature communications* **11** (2020), no. 1 1–8

14. Y. Wan, S. Zhang, J. C. Norman, M. Kennedy, W. He, S. Liu, C. Xiang, C. Shang, J.-J. He, A. C. Gossard, *et. al.*, *Tunable quantum dot lasers grown directly on silicon*, *Optica* **6** (2019), no. 11 1394–1400

Conference Proceedings

1. C. Xiang, W. Jin, J. Guo, P. Morton, and J. E. Bowers, *Temperature stable III-V/Si/Si_3N_4 heterogeneous integrated laser*, in *ECS Meeting Abstracts*, no. 26, p. 1832, IOP Publishing, 2020 [Invited]

2. C. Xiang, W. Jin, J. Guo, J. D. Peters, M. Kennedy, J. Selvidge, P. A. Morton, and J. E. Bowers, *Temperature stable, narrow linewidth heterogeneously integrated semiconductor laser with Si_3N_4 cavity*, in *CLEO: Science and Innovations*, pp. STu3M–6, Optical Society of America, 2020

3. C. Xiang, P. A. Morton, and J. E. Bowers, *1550 nm laser with 320 Hz Lorentzian linewidth based on semiconductor gain chip and extended Si_3N_4 bragg grating*, in *CLEO: Science and Innovations*, pp. SW4N–6, Optical Society of America, 2019

4. C. Xiang, P. A. Morton, J. Khurgin, C. Morton, and J. E. Bowers, *Widely tunable Si_3N_4 triple-ring and quad-ring resonator laser reflectors and filters*, in *2018 IEEE 15th International Conference on Group IV Photonics (GFP)*, pp. 1–2, IEEE, 2018

5. C. Xiang, P. A. Morton, and J. E. Bowers, *Ultra-narrow linewidth laser based on a semiconductor gain chip and extended Si_3N_4 Bragg grating*, *Optics Letters* **44** (2019), no. 15 3825–3828

6. C. Xiang, M. L. Davenport, J. B. Khurgin, P. A. Morton, and J. E. Bowers, *Tunable optical delay line based on Si_3N_4 ring resonators*, in *2017 IEEE Photonics Conference (IPC)*, pp. 119–120, IEEE, 2017

7. C. Xiang, M. A. Tran, T. Komljenovic, J. Hulme, M. Davenport, D. Baney, B. Szafraniec, and J. E. Bowers, *Integrated chip-scale wavemeter with 300 MHz free spectral range*, in *CLEO: Science and Innovations*, pp. SM3G–3, Optical Society of America, 2016

8. B. Shen, L. Chang, J. Liu, H. Wang, Q.-F. Yang, C. Xiang, R. N. Wang, J. He, T. Liu, W. Xie, *et. al.*, *Integrated turnkey soliton microcombs operated at CMOS frequencies*, in *2020 Conference on Lasers and Electro-Optics (CLEO)*, pp. 1–2, IEEE, 2020

9. L. Chang, W. Xie, H. Shu, Q.-F. Yang, B. Shen, A. Boes, J. D. Peters, W. Jin, C. Xiang, S. Liu, *et. al.*, *Ultra-efficient frequency comb generation in AlGaAs-on-insulator microresonators*, in *CLEO: Science and Innovations*, pp. STu3H–8, Optical Society of America, 2020

10. T. Briles, L. Chang, C. Xiang, J. Guo, D. Kinghorn, J. Stone, S. Yu, G. Moille, K. Srinivasan, J. Bowers, *et. al.*, *Semiconductor laser integration for octave-span Kerr-soliton frequency combs*, in *2020 Conference on Lasers and Electro-Optics (CLEO)*, pp. 1–2, IEEE, 2020

11. J. E. Bowers, L. Chang, D. Huang, A. Malik, A. Netherton, M. Tran, W. Xie, and C. Xiang, *Terabit transmitters using heterogeneous III-V/Si photonic integrated circuits*, in *Optical Fiber Communication Conference*, pp. W3F–1, Optical Society of America, 2020

12. T. C. Briles, J. R. Stone, S. B. Papp, G. Moille, K. Srinivasan, L. Chang, C. Xiang, J. Guo, and J. E. Bowers, *Generation of octave-spanning microresonator solitons with a self injection-locked DFB laser*, in *2019 IEEE Avionics and Vehicle Fiber-Optics and Photonics Conference (AVFOP)*, pp. 1–2, IEEE, 2019

Abstract

Heterogeneous integration for silicon nitride photonics

by

Chao Xiang

Silicon nitride (Si_3N_4), as a CMOS compatible material that is widely used in modern IC technology, is emerging as the backbone in a variety of photonic applications including nonlinear photonics, microwave photonics and so on. The next-generation advanced photonic integrated circuits using ultra-low-loss Si_3N_4 waveguides requires a higher integration level. However, current Si_3N_4-based devices are still restricted to stand-alone passive devices, due to the significant difficulties of laser integration.

Heterogeneous silicon photonic integration has achieved success in datacenter interconnects by providing efficient III-V gain to passive silicon photonic circuits. The past decade also witnessed dramatic progress in the performances of silicon photonic devices including III-V/Si lasers. One important reason is the reduced optical loss of silicon compared with monolithic III-V waveguides and further developments require heterogeneous integration with ultra-low-loss Si_3N_4 waveguides.

In this thesis, I will discuss the approach to heterogeneously integrate III-V gain with Si_3N_4 photonic circuits using a novel multilayer integration structure. This approach results in the first-generation of heterogeneously integrated lasers on (Si_3N_4) with high temperature stability. With optimization, this integration platform results in high-performance lasers with high power and low noise for fully integrated silicon nitride photonics and is promising to enable Hertz-level linewidth integrated lasers. Moreover, the integration techniques also enabled the first heterogeneously integrated laser soliton microcombs with full electrical control on a monolithic silicon substrate. The demon-

strated devices represent state-of-the-art performances of heterogeneous integration. The results in this thesis would open up a new regime of integrated photonics research and enable a whole new class of devices with unprecedented capabilities.

Contents

List of Figures

Chapter 1

Introduction

Integrated photonics has come a long way since it offers miniaturization of optical functionalities into a compact form factor, allowing for the improvement in performance as well as the reduction in terms of size, weight, power consumption and cost (SwAP+C). The photonic integration relies heavily on the choice of substrate material as different material groups are not natively compatible with each other and the choice of substrate largely determines the capability of the photonic device capabilities on chip. Indium phosphide (InP) and gallium arsenide (GaAs) substrates are widely deployed for decades for the first-generation of integrated photonic devices as they offer the capability of a wide variety of optical functions natively integrated such as lasers, modulators and photodetectors. Advanced photonic integrated circuits based on InP and GaAs are extensively used in applications including telecommunications, microwave photonics, free space laser communications and so on[1–3].

However, an important issue with InP or GaAs substrates is the high substrate cost. As a comparison, silicon is a very low cost substrate and it breeds the modern integrated circuits (IC) technology. It holds great promises to enable low-cost, large volume photonic integrated circuits. Over the development for past two decades, silicon photonics has

now become a technology that is successful in datacenter optical interconnects with a fast growing pace. In other applications including LIDAR and optical communications, silicon photonic products are also showing great advantages as the performance and integration level keeps improving over the years, meanwhile, with cost going lower and lower.

In this chapter, I will introduce the background and motivation of silicon photonics and as one step further, briefly discuss the developments of heterogeneous integration and silicon nitride photonics which form the basis of this dissertation.

1.1 Silicon and silicon nitride photonics

Silicon photonics is defined as making photonics integrated circuits (PICs) on silicon using standard CMOS facilities. This highlights one important advantage of silicon photonics - it is compatible and beneficial from existing mature CMOS fabrication facilities which were developed for electronics IC (EIC) industry. Same as state-of-the-art EIC industry, Si PICs can be made from 300-mm diameter Si substrate wafers which enables large volume and low cost production of Si PICs. In addition, as a natural fit, Si PICs can be beneficial of advanced packaging technologies developed for EIC industry. Nowadays, the co-packaging of PICs and EICs propels a giant leap in network switch capacity and this is of critical importance in datacenter applications as the power consumption becomes the bottleneck using traditional copper wire based electrical interconnects. Co-packaged silicon PICs with EICs, represents the next-generation technology in this area. Figure 1 shows the evolution of datacom transceivers through five generations of technology. Datacom transceivers using silicon photonics have rapidly moved from product introductions to multi-million units per year and drives the developments of high-capacity optical interconnect applications.

One important feature of silicon photonics is its offers a low loss and compact silicon waveguide which together with silicon dioxide cladding, enabling dB/cm-scale optical loss and laying the basis for low-cost, high-density and high-volume Si PICs[4–7]. This also offers the improvement in device performance, compared with InGaAsP based III-V waveguides. Si modulators (MZM or ring modulator), SiGe photodetectors, Si (de)multiplexers, etc are standardized in multiple CMOS photonics foundries across the globe and the silicon photonics ecosystem is growing rapidly, similar as how silicon electronics disrupted the EIC technology in the last century. As the integration level and data rates grows, target power requirements have dropped from thousands of pJ/bit to sub-pJ/bit over the past decade.

Moving towards petabyte per second network switch capacity, Si PICs with integrated lasers are projected to meet the requirement on optical interconnect link capacity in the coming decade through 3D co-packing with electronics (Fig. 1.1). As silicon is an indirect-bandgap material, lasers are not available for the early generations of Si PICs. Individual, off-chip III-V laser chips are required in Si PIC products. This situation was disrupted since the heterogeneous integration technology of III-V materials developed since the year 2006[8]. High-performance lasers with wafer-scale processes enabled large-scale integration of lasers seamlessly with Si photonic devices[9–11]. This enables scaling from one laser per PIC to potentially thousands of lasers per PIC, and thus enabling Pbps-scale data connections.

In addition to silicon, silicon nitride (Si_3N_4), which is a COMS-compatible material, also finds widely use in modern IC technology. Silicon nitride photonics is emerging in recent years as advanced photonic devices require better performance than is available from traditional Si or InGaAsP waveguides. The typical optical loss from Si_3N_4 waveguide is 10x and 100x times lower than typical Si or InGaAsP waveguide. Si_3N_4-based waveguides also offers a wide transparency from the visible to the infrared, a low

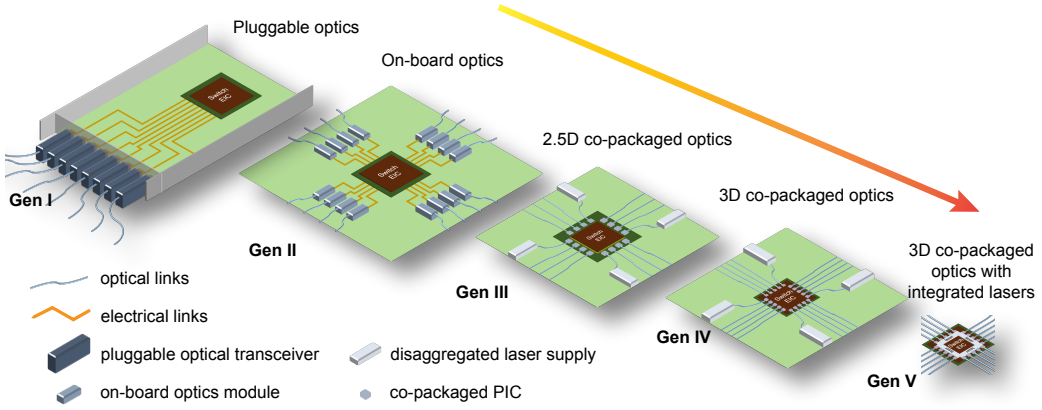

Figure 1.1: The development of co-packaging systems used in data center applications the generations of optics. The evolution of network switching and optical I/O convergence leads to 3D co-packaged optics with integrated lasers on chip. ©AIP publishing.

thermo-optic coefficient and absence of nonlinear absorption loss, which are ideal for many photonic applications[12–14]. For example, Si_3N_4 forms the backbone of chip-scale nonlinear photonics[15], high-fidelity integrated microwave photonics systems[16] and ultra-broadband integrated photonic circuits[17]. As a result, Si_3N_4-based photonic components, benefiting from the superior passive properties of Si_3N_4 material, represent the state-of-the-art performance of integrated photonics, including frequency comb generators[18–20], optical gyroscopes[21] and so on.

However, Si_3N_4 photonic applications are largely restricted with passive devices. This is mainly due to two reasons. First of all, Si_3N_4 is a dielectric material and has no direct energy-bandgap. So no efficient nonradiative carrier recombination is available in Si_3N_4, which is the basis of semiconductor lasers. Secondly, the refractive index of Si_3N_{4x} is around 2 depending on the silicon content. As a comparison, InP or GaAs III-V epis normally has the slab mode index of 3.4. So in a similar way as heterogeneous InP/Si integration, InP/Si would be very challenging to facilitate efficient mode transition between III-V and Si layers, even with extreme tapering of III-V layer (2 µm thick).

Lasers are essential and key components in silicon nitride photonics. In this thesis,

I will describe the utilization of multilayer heterogeneous integration to enable efficient high-performance lasers for fully integrated silicon nitride photonics. As one step further, based on multilayer heterogeneous integration, lasers are fully integrated with nonlinear Si_3N_4 High-Q ring resonators which gave birth to the first heterogeneously integrated laser soliton microcomb devices on silicon.

1.2 Properties of silicon nitride in photonics

As a CMOS compatible material, Si_3N_4 is widely deployed in modern IC technology. In photonics, Si_3N_4 has following properties that are advantageous in many applications:

1. Low index contrast with SiO_2 cladding
    - Enabling lower scattering loss than Si waveguides
    - Low phase error than Si interferometers
2. Broadband transparency
    - From visible to mid-IR applications
3. Negligible nonlinear absorption
    - High power handling capability for nonlinear applications
4. Low thermo-optic coefficient
    - Low thermorefractive noise
    - High temperature stability

While there is no direct bandgap or electro-optic effect in Si_3N_4, Si_3N_4 has superior passive properties and finds wide use in low loss time delay lines for microwave photonics, broadband sensing applications and nonlinear photonics. The Si_3N_4 waveguide

core dimension is important in determining its application scenario. For example, thick Si_3N_4 layer (normally > 700 nm thick) is required to yield anomaly dispersion which is required for bright soliton frequency comb generation but Si_3N_4 layer is highly stressed so stress-release issues need to be solved in thick Si_3N_4 layer deposition. Practical methods include photonic Damascene process [22] and two-step Si_3N_4 deposition with mechanical isolation trenches[23]. For thin thickness Si_3N_4 films the cracking issue is greatly resolved at the expensive of less mode confinement and lower nonlinearity. This type of Si_3N_4 waveguide structure will be used in this thesis for narrow-linewidth laser demonstrations in Chapter 3 and 4. The thick Si_3N_4 waveguide using photonic Damascene process is used in Chapter 5 for heterogeneously integrated optical frequency comb generation.

1.3 Integration approaches

There are three integration approaches in photonics depending on the usage of substrate. Monolithic integration includes homoepitaxial or heteroepitaxial growth of III-V or Si and processing on a common (monolithic) substrate. The scale is wafer scale and the cost and scale difference mainly results from the substrates. Recent progress in QDs grown on Si substrates endows high-performance laser sources at cost-effective Si substrates (up to 300-mm diameter). Hybrid integration refers to hybrid packaging of individual chips with separate substrates through optical coupling. Flip chip bonding can be considered as a method of hybrid packaging and this integration normally happens at device level or die level. Heterogeneous integration, on the other hand, leverages wafer bonding technology to combine materials and create layered structures that cannot be directly grown or formed together. The integration is also at wafer scale and supports parallel processing of a large number of devices.

Figure 1.2 summarizes the scale and cost comparisons between the different integra-

tion approaches. Optical packaging with optical alignment is often occupies over 90% of the total cost. And the alignment process is time consuming and limits the overall device throughput. Flip-chip bonding of lasers onto pre-fabricated Si photonic circuits also requires fine optical alignment.

As a comparison, monolithic or heterogeneous integration offers a device fabrication manner that is done on wafer scale and doesn't require sophisticated optical packaging. Particularly for heterogeneous integration, although it also cooperates the original wafers from separate substrates similar as hybrid packaging, the bonding doesn't require fine alignment and the process is on blank films without patterns. As a result, the device alignment is determined by optical lithography accuracy thus low coupling loss from the laser to Si waveguide can be achieved.

Currently, many Si photonics companies rely on hybrid packaging to build optical transceiver modules with disaggregated III-V lasers. It comes with a high cost of pack-

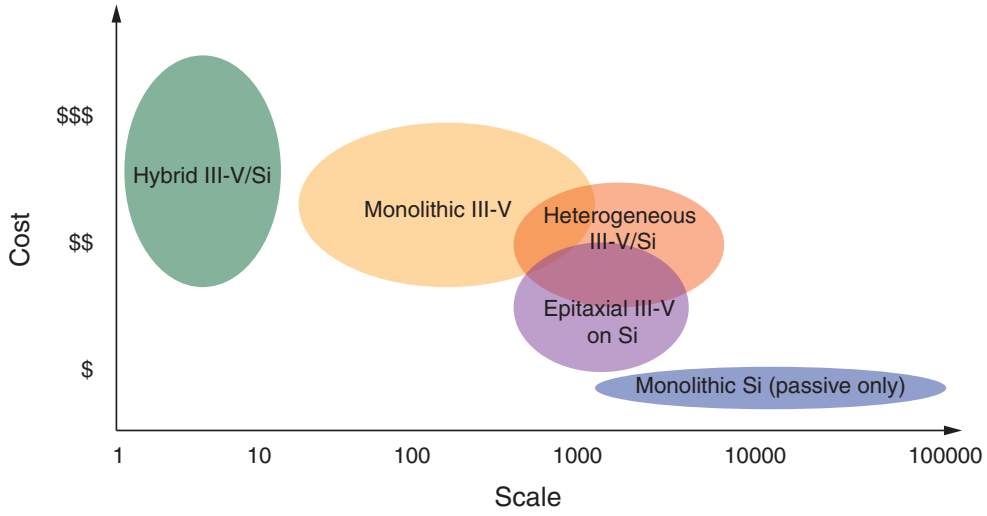

Figure 1.2: A comparison of scale an cost for different integration approaches including hybrid III-V/Si integration, monolithic III-V integration, heterogeneous III-V/Si integration, heteroepitaxial III-V-on-Si integration and monolithic Si integration (passive only).

aging and large coupling loss, but the laser chip and Si photonics chip can be attained from well established III-V and Si fabrication facilities. There is a trend to incorporate Si circuits into the laser cavity and this works pretty well for widely-tunable lasers based on Si coupled ring resonators [24–27].

One advantage of hybrid integration is the capability to optimize the actives and passives separately without sacrificing for process compatibility. Thus the best-in-class passives can find widespread use in a hybrid integrated system. Recent progress of utilizing ultra low loss Si_3N_4 waveguide ring resonators in an external cavity laser enables 40-Hz fundamental linewidth with high output power [28]. Ultra-low loss Si_3N_4 waveguide enables ultra-high-Q resonators with $Q > 200$ million and is used to suppress the laser frequency noise using self-injection locking. Record fundamental linewidth of 1.2 Hz is achieved [29].

With monolithic substrates, the high cost for optical packaging separate chips can be eliminated. The choice of substrate then becomes important in the overall cost. Si substrates with up to 300-mm diameter offers the lowest cost and largest integration scale. Heteroepitaxial growth of III-V QDs thus potentially offers the lowest cost for active photonic devices, but significant work has to be done to efficiently integrated lasers with Si photonic circuits for wider deployments of QD based lasers.

As a comparison, heterogeneous integration allows the use of large Si handle substrate and offers intrinsic advantage of active-passive integration due to evanescent coupling. Wafer bonding also supports versatile materials to be integrated and enables the adoption of best-in-class materials to fulfill advanced and complex optical functionalities. And this integration technique will be the main target of this thesis.

1.4 Accomplishments in this thesis

The integration of ultra low loss Si_3N_4 waveguide provides a new paradigm to improve active devices performance and enable new class of integrated devices. The key results in this thesis include:

1. Record low-loss tunable time delay line based on Si_3N_4 ring resonators
2. Ultra-narrow linewidth hybrid-integrated laser with Si_3N_4 extended Bragg grating
3. First demonstration of narrow-linewidth,temperature-stable III-V/Si/Si_3N_4 laser
4. High-power, low-noise semiconductor laser heterogeneously integrated with Si_3N_4 cavity
5. First demonstration of heterogeneously integrated soliton microcombs

One important parameter of the laser performance - the optical linewidth - is one focus of the demonstrations. The narrow laser linewidth resulting from the hybrid integration with Si_3N_4 DBR cavity, heterogeneous integration with Si_3N_4 cavity and ultra-high-Q Si_3N_4 ring resonators also represent the current record performance among the approaches used. These progress in semiconductor laser linewidth reduction is summarized in Fig. 3.1.

Another importance of the demonstration is that, with an addition of on-chip high-performance laser heterogeneouly integrated with Si_3N_4, fully-integrated silicon nitride photonic become realistic for the first time ever. This thesis shows the prototype of Hertz-level linewidth integrated semiconductor laser and fully electrically initialed and controlled soliton microcombs. These devices wil have a wide spread applications in microwave photonics, optical sensing, terabit-per-second high-capacity optical interconnects and so on. More details will be covered in Chapter 4 and 5.

1.5 Thesis outline

This thesis focuses on the development of heterogeneous integration for silicon nitride photonics. Chapter 2 describes a series of passive photonic devices on silicon nitride platform, including grating based devices (low-κ grating, spiral grating) for narrow-linewidth lasers and ring-resonator based devices for optical time delay line and laser reflectors/filters. Chapter 3 first introduces the design of narrow-linewidth lasers. One important advantage of Si_3N_4 over Si in terms of nonlinear loss will also be covered. Based on Si_3N_4 Bragg grating, a hybrid-integrated laser with ultra-narrow linewidth is demonstrated. In addition to hybrid integration verifying the grating design for high-performance lasers, the method to heterogeneously integrate the Si_3N_4 waveguide with III-V gain material on a monolithic Si substrate is discussed in Chapter 4. The result is a III-V/Si/Si_3N_4 multilayer heterogeneous integration structure. Chapter 4 also covers the developments of the first heterogeneously integrated Si_3N_4 laser with high temperature stability and high-performance lasers with high output power and low noise which are ideal for fully integrated silicon nitride photonics, In Chapter 5, the III-V/Si/Si_3N_4 integration is extended to another Si_3N_4 platform which is featured with nonlinear frequency comb applications. In this work, the development and results on the first integrated laser soliton microcomb device will be discussed. The details of the heterogeneous III-V/Si/Si_3N_4 laser fabrication process will be included in Appendix A.

References

[1] L. A. Coldren, S. W. Corzine, and M. Mashanovitch, *Diode lasers and photonic integrated circuits*. Wiley, 2012.

[2] R. Nagarajan, C. H. Joyner, R. P. Schneider, J. S. Bostak, T. Butrie, A. G. Dentai, V. G. Dominic, P. W. Evans, M. Kato, M. Kauffman, *et. al.*, *Large-scale photonic integrated circuits*, *IEEE Journal of Selected Topics in Quantum Electronics* **11** (2005), no. 1 50–65.

[3] J. Klamkin, H. Zhao, B. Song, Y. Liu, B. Isaac, S. Pinna, F. Sang, and L. Coldren, *Indium phosphide photonic integrated circuits: Technology and applications*, in *2018 IEEE BiCMOS and Compound Semiconductor Integrated Circuits and Technology Symposium (BCICTS)*, pp. 8–13, IEEE, 2018.

[4] B. Jalali and S. Fathpour, *Silicon photonics*, *J. Lightwave Technol.* **24** (2006), no. 12 4600–4615.

[5] G. T. Reed and A. P. Knights, *Silicon photonics: an introduction*. John Wiley & Sons, 2004.

[6] R. Soref, *The past, present, and future of silicon photonics*, *IEEE Journal of selected topics in quantum electronics* **12** (2006), no. 6 1678–1687.

[7] L. Pavesi *et. al.*, *Silicon photonics*, vol. 94. Springer Science & Business Media, 2004.

[8] A. W. Fang, H. Park, O. Cohen, R. Jones, M. J. Paniccia, and J. E. Bowers, *Electrically pumped hybrid AlGaInAs-silicon evanescent laser*, *Optics Express* **14** (2006), no. 20 9203.

[9] T. Komljenovic, M. Davenport, J. Hulme, A. Y. Liu, C. T. Santis, A. Spott, S. Srinivasan, E. J. Stanton, C. Zhang, and J. E. Bowers, *Heterogeneous silicon photonic integrated circuits*, vol. 34. IEEE, Jan., 2016.

[10] T. Komljenovic, D. Huang, P. Pintus, M. A. Tran, M. L. Davenport, and J. E. Bowers, *Photonic Integrated Circuits Using Heterogeneous Integration on Silicon*, *Proceedings of the IEEE* **106** (Dec., 2018) 2246–2257.

[11] R. Jones, P. Doussiere, J. B. Driscoll, W. Lin, H. Yu, Y. Akulova, T. Komljenovic, and J. E. Bowers, *Heterogeneously Integrated InP/Silicon Photonics: Fabricating Fully Functional Transceivers*, *IEEE Nanotechnology Magazine* **13** (Apr., 2019) 17–26.

[12] M. J. Heck, J. F. Bauters, M. L. Davenport, D. T. Spencer, and J. E. Bowers, *Ultra-low loss waveguide platform and its integration with silicon photonics*, *Laser & Photonics Reviews* **8** (2014), no. 5 667–686.

[13] J. F. Bauters, M. J. R. Heck, D. D. John, J. S. Barton, C. M. Bruinink, A. Leinse, R. G. Heideman, D. J. Blumenthal, and J. E. Bowers, *Planar waveguides with less than 0.1 db/m propagation loss fabricated with wafer bonding*, *Opt. Express* **19** (Nov, 2011) 24090–24101.

[14] C. Xiang, W. Jin, J. Guo, C. Williams, A. M. Netherton, L. Chang, P. A. Morton, and J. E. Bowers, *Effects of nonlinear loss in high-Q Si ring resonators for narrow-linewidth III-V/Si heterogeneously integrated tunable lasers*, *Optics Express* **28** (2020), no. 14 19926–19936.

[15] J. Liu, A. S. Raja, M. H. P. Pfeiffer, C. Herkommer, H. Guo, M. Zervas, M. Geiselmann, and T. J. Kippenberg, *Double inverse nanotapers for efficient light coupling to integrated photonic devices*, *Opt. Lett.* **43** (Jul, 2018) 3200–3203.

[16] C. G. Roeloffzen, L. Zhuang, C. Taddei, A. Leinse, R. G. Heideman, P. W. van Dijk, R. M. Oldenbeuving, D. A. Marpaung, M. Burla, and K.-J. Boller, *Silicon nitride microwave photonic circuits*, *Optics Express* **21** (2013), no. 19 22937–22961.

[17] P. Muñoz, G. Micó, L. A. Bru, D. Pastor, D. Pérez, J. D. Doménech, J. Fernández, R. Baños, B. Gargallo, R. Alemany, *et. al.*, *Silicon nitride photonic integration platforms for visible, near-infrared and mid-infrared applications*, *Sensors* **17** (2017), no. 9 2088.

[18] B. Stern, X. Ji, Y. Okawachi, A. L. Gaeta, and M. Lipson, *Battery-operated integrated frequency comb generator*, *Nature* **562** (2018), no. 7727 401–405.

[19] A. S. Raja, A. S. Voloshin, H. Guo, S. E. Agafonova, J. Liu, A. S. Gorodnitskiy, M. Karpov, N. G. Pavlov, E. Lucas, R. R. Galiev, A. E. Shitikov, J. D. Jost, M. L. Gorodetsky, and T. J. Kippenberg, *Electrically pumped photonic integrated soliton microcomb*, *Nature Communications* **10** (2019), no. 1 680.

[20] B. Shen, L. Chang, J. Liu, H. Wang, Q.-F. Yang, C. Xiang, R. N. Wang, J. He, T. Liu, W. Xie, J. Guo, D. Kinghorn, L. Wu, Q.-X. Ji, T. J. Kippenberg, K. Vahala, and J. E. Bowers, *Integrated turnkey soliton microcombs*, *Nature* **582** (2020), no. 7812 365–369.

[21] S. Gundavarapu, G. M. Brodnik, M. Puckett, T. Huffman, D. Bose, R. Behunin, J. Wu, T. Qiu, C. Pinho, N. Chauhan, J. Nohava, P. T. Rakich, K. D. Nelson, M. Salit, and D. J. Blumenthal, *Sub-hertz fundamental linewidth photonic integrated brillouin laser*, *Nature Photonics* **13** (2019), no. 1 60–67.

[22] M. H. P. Pfeiffer, A. Kordts, V. Brasch, M. Zervas, M. Geiselmann, J. D. Jost, and T. J. Kippenberg, *Photonic damascene process for integrated high-q microresonator based nonlinear photonics*, *Optica* **3** (2016), no. 1 20–25.

[23] K. Luke, A. Dutt, C. B. Poitras, and M. Lipson, *Overcoming Si_3N_4 film stress limitations for high quality factor ring resonators*, *Opt. Express* **21** (Sep, 2013) 22829–22833.

[24] N. Fujioka, T. Chu, and M. Ishizaka, *Compact and low power consumption hybrid integrated wavelength tunable laser module using silicon waveguide resonators*, *Journal of lightwave technology* **28** (2010), no. 21 3115–3120.

[25] N. Kobayashi, K. Sato, M. Namiwaka, K. Yamamoto, S. Watanabe, T. Kita, H. Yamada, and H. Yamazaki, *Silicon photonic hybrid ring-filter external cavity wavelength tunable lasers*, *Journal of Lightwave Technology* **33** (2015), no. 6 1241–1246.

[26] H. Guan, A. Novack, T. Galfsky, Y. Ma, S. Fathololoumi, A. Horth, T. N. Huynh, J. Roman, R. Shi, M. Caverley, *et. al.*, *Widely-tunable, narrow-linewidth iii-v/silicon hybrid external-cavity laser for coherent communication*, *Optics Express* **26** (2018), no. 7 7920–7933.

[27] Y. Gao, J.-C. Lo, S. Lee, R. Patel, L. Zhu, J. Nee, D. Tsou, R. Carney, and J. Sun, *High-power, narrow-linewidth, miniaturized silicon photonic tunable laser with accurate frequency control*, *Journal of Lightwave Technology* **38** (2020), no. 2 265–271.

[28] Y. Fan, A. van Rees, P. J. Van der Slot, J. Mak, R. M. Oldenbeuving, M. Hoekman, D. Geskus, C. G. Roeloffzen, and K.-J. Boller, *Hybrid integrated inp-Si_3N_4 diode laser with a 40-hz intrinsic linewidth*, *Optics Express* **28** (2020), no. 15 21713–21728.

[29] W. Jin, Q.-F. Yang, L. Chang, B. Shen, H. Wang, M. A. Leal, L. Wu, M. Gao, A. Feshali, M. Paniccia, *et. al.*, *Hertz-linewidth semiconductor lasers using cmos-ready ultra-high-q microresonators*, *Nature Photonics* (2021) 1–8.

Chapter 2

Silicon nitride passive devices

Silicon nitride waveguide enabling ultra low optical loss is its fundamental advantage in many photonic applications that waveguide loss plays a critical role in the device performance. These devices include narrow linewidth lasers[1], high-Q nonlinear photonics[2], microwave photonics[3] and so on. In this chapter I will cover the low loss silicon nitride waveguide and a series of passive devices developments on it.

2.1 Silicon nitride waveguide

The silicon nitride waveguide used in this thesis is mostly thin-core Si_3N_4 waveguide with 90 nm thick and 2.8 µm wide. Figure 2.1 shows the thin-core Si_3N_4 waveguide cross setcion. This waveguide geometry is designed such that the waveguide offers high polarization extinction ratio and for the fundamental TE mode, $\sim$ 90 % mode power resides in the top SiO_2 upper cladding and the buried oxide under cladding. So in order to obtain a low propagation loss, the quality of the top and bottom cladding oxide is important. In order to achieve a low absorption loss, high temperature anneal is required to drive off the residue hydrogen of the Si_3N_4 and SiO_2 material due to

the precursors $SiCl_2H_2$ and NH_3 used in the stoichiometric LPCVD process for Si_3N_4 (low pressure chemical vapor deposition) and SiH_4 in PECVD process for SiO_2 (plasma-enhanced chemical vapor deposition). After PECVD SiO_2 deposition, a 1050 °C annealing is performed for longer than 8 hours to drive out the hydrogen residue. Tetraethyl orthosilicate (TEOS) is nowadays widely used as a high-quality precursor material.

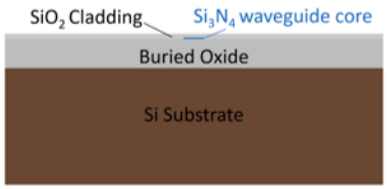

Figure 2.1: Thin-core Si_3N_4 waveguide cross section

The waveguide core is selected to be 90 nm, in order to minimize the sidewall scattering loss, which is a major loss contributor for typical silicon-on-insulator waveguides and thick-Si_3N_4 waveguides. During process, the Si_3N_4 core is etched using $CHF_3/CH_4/O_2$ based SiO_2 etch, thus the full waveguide etch can tolerate waveguide over etch as long as the waveguide is cladded with high-quality SiO_2 cladding without air gaps. The 90-nm thickness can be further reduced to around 40 nm to allow for guided TE0 mode and further loss reduction as the loss is distributed further into the cladding material. This resulted in record low loss among any integrated planar photonic waveguides (< 0.1 dB/m)[4; 5]. However, this requires a larger bend radii to reduce the bending radiation loss and the bending radius has to be above 5 mm. So we choose 90 nm thickness as a balance of achievable optical propagation loss (< 5 dB/m) and reasonable bending radius (> 600 µm) for photonic integration for this thesis (2.2). In order to further reduce the loss, the upper cladding can be replaced by wafer-bonded thermal oxide with very high quality. And experiments have seen that multiple depositions and anneal runs during the cladding deposition are beneficial in further purifying the hydrogen contamination and lower the loss[6]. The buried oxide (BOX) layer needs to be thick enough to avoid

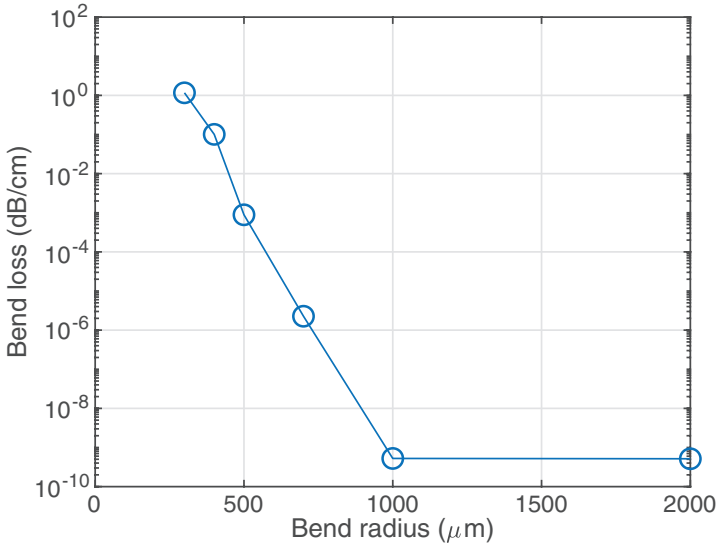

Figure 2.2: Simulated waveguide bending loss versus the bend radius for the 90-nm thick thin-core Si_3N_4 waveguide .

substrate leakage, but will degrade the heat dissipation efficiency in certain applications. In this thesis the BOX is mostly 15 µm thick for passive devices and for heterogeneous devices on thin-core Si_3N_4, the BOX is kept at 8 µm thick.

With this loss value, the affordable waveguide length can be increased to meters or even tens of meters scale in spiral waveguide shape, and resonant structures like ring resonators can create optical path length on this scale, but with much reduced device footprint. This offers a compelling solution in direct on chip laser noise reduction which helps enable narrow linewidth lasers and its integration with lasers is the main focus of this thesis.

2.1.1 Wavemeter

One integrated device that is enabled by low loss Si_3N_4 waveguide is integrated wavemeter based on unbalanced MZI (Mach–Zehnder interferometer) [7]. Wavemeters are widely used in laser systems to linearize the laser sweep rate, but mostly built using

bulk fibers. Fiber-based wavemeter has the drawback of polarization stability. In order to reduce the sensitivity, polarization maintaining (PM) fiber can be used but this increases the overall cost significantly. And the fiber-based wavemeter still suffers from sensitivity to vibrations, temperature variations and are relatively bulky in size. As a comparison, Si_3N_4 waveguides have a high aspect ratio and have very high polarization extinction, up to 75 dB [8] making the Mach-Zehnder style interferometer extremely polarization stable.

Chip-scale integration can improve stability while lowering costs, reducing size, and reducing weight. Furthermore, in terms of wavelength control and potential correction or stabilization, it is critical to use a chip-scale solution for an on-chip tunable laser source. We develop a chip-scale Mach-Zehnder interferometer based on the Si_3N_4 waveguide platform, which is low-loss. The use of the Si_3N_4 waveguide platform has a number of advantages including a high polarization extinction ratio and low propagation loss. For the unbalanced MZI configuration, the 62.1 cm long delay line takes up 3.5 mm x 6.5 mm of space using a spiral shaped waveguide, and the total chip size, which includes two wavemeter designs, is approximately 8 mm x 13 mm. Figure 2.3 depicts both designs. The wavemeter A is an UMZI design and the wavemeter B is an UMZI with an optical hybrid. to extract the optical phase information and having four outputs. This helps to increase the accuracy of wavemeter reading[7].

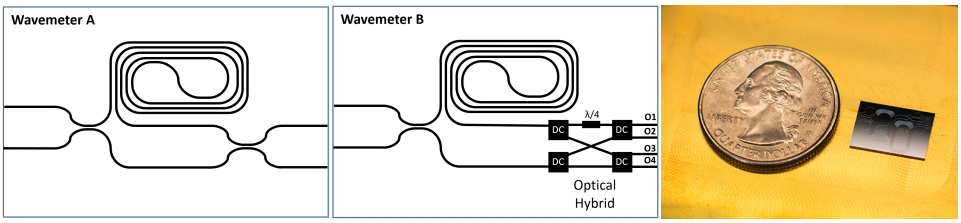

Figure 2.3: Designs of integrated wavemeter with A: UMZI design and B: UMZI plus optical hybrid for phase retrieval. Right picture shows a wavemeter chip comprising two designs and its size comparison with an US quarter coin. ©OSA publishing

The optical hybrid, as shown in Figure 2.3, consists of four 50/50 directional couplers with waveguide interconnections in between. The uppermost branch, in particular, has a λ /4 optical delay centered on the center wavelength of 1550 nm. The so-called I (in-phase) and Q (quadrature) channels are formed by a selective combination of the ports that have a 90^o phase change with each other. A complex representation of the output signal can thus be found using I and Q. The wavelength is represented by the phase of that signal and scaled by FSR (free spectral range). Wavemeter measurement precision can also be improved by having many outputs in wavemeter B design compared to A design and as a result I will focus on this type in the discussion.

The directional couplers in the UMZI were designed to compensate for higher propagation loss in the longer arm, but due to higher than expected propagation loss, some fringes have lower extinction ratios. As shown in Fig. 2.4a, the FSR is found to be 2.4 pm and clear fringes are obtained (corresponding to 300 MHz). This small FSR is ideal for wavelength monitoring and correction with high precision. Meanwhile, a phase change between the output ports can be seen in the wavelength response. The outputs O2 and O3 can, for example, be used as I and Q to demodulate phase and, as a result, the wavelength of the input signal. About 1550 nm, the wavemeter has an extinction ratio of up to 18 dB, and both the extinction ratio and the phase shift between the outputs are relatively robust again temperature changes. As a result, wavelength estimation is independent of temperature. Figure 2.4b shows that the port with the highest extinction ratio (O4) retains a nearly constant ER of 17.5 dB over a temperature range of 15 to 50 °C, confirming the benefits from using temperature-insensitive Si_3N_4 and SiO_2 material. At 1550 nm, Si_3N_4 has a low thermo-optic coefficient ($dn/dT = (2.45 \pm 0.09) \times 10^{-5}$) (RIU/°C) in our wavemeter configuration, which is an order of magnitude lower than Si.

Aside from the extinction ratio, the phase shift of output ports is also relatively unaffected by temperature changes (Figure. 2.5). At 27 °C, 15 °C, and 50 °C, respectively,

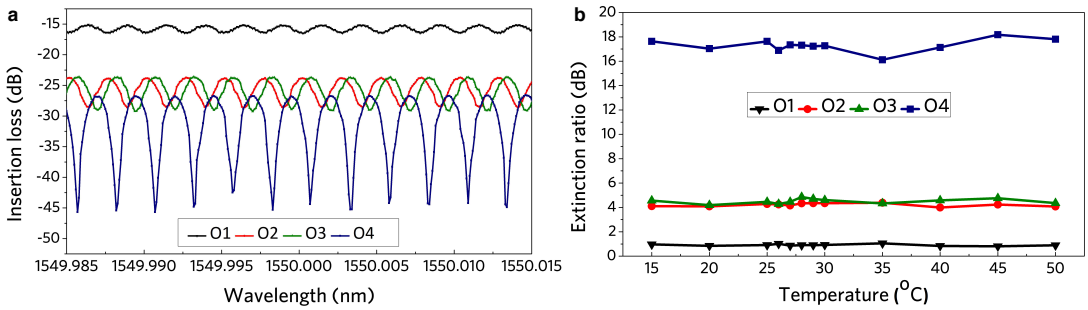

Figure 2.4: a. Measured response of the wavemeter design B for 4 ports around 1550 nm at room temperature. b. Extinction ratio versus temperature for different wavemeter output ports near 1550 nm. ©OSA publishing

Figure 4(a), (b), and (c) display the normalized wavelength response of all four outputs on a linear scale. The red curves are the best fits of the sine function to the corresponding results, with relative phase shifts of 0°, 180°, 90°, and -90°, respectively. The phase response is consistent with the design, based on the excellent fit of experimental results. Furthermore, the fit is repeatable at various temperatures. Although the optical hybrid is dependent on the accuracy of the $\lambda/4$ optical delay, which can be affected by temperature, the integrated Si_3N_4 platform allows for largely temperature insensitive operation.

Another advantage of integrated chip-based optical wavemeters over fiber-based systems is their increased robustness to vibration, temperature fluctuations, and much improved stability. The operation of the fiber-based unbalanced Mach-Zehnder interferometer (UMZI), which is used to make the most common fiber-based wavemeter, is inherently unstable over time. We conducted a stability comparison test in the setup shown in Fig. 2.6a to compare its stability to our wavemeter chip. The output of a Brillouin single-frequency narrow-linewidth fiber laser source was split into two branches and fed into the fiber UMZI and our wavemeter chip, respectively. An optical variable attenuator (VOA) was used before the fiber UMZI to equalize output powers from the fiber UMZI and the chip. Since the fiber UMZI does not have an output optical hybrid, the interferometers'

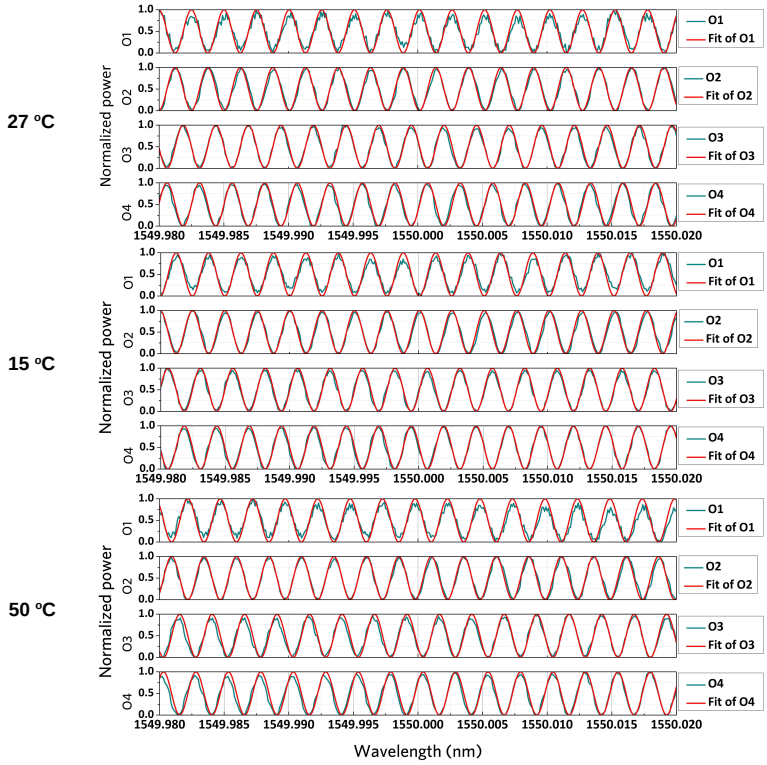

Figure 2.5: At temperatures of 27 °C, 15 °C, 50 °C, normalized output power was measured at various ports of wavemeter. Red curves are sine best fits with phase differences of 0°, 180°, 90°, and -90° from port O1. ©OSA publishing

stability is dictated by power fluctuations. Since the fibers in the setup do not sustain polarization, two polarization controllers are used in both branches, as shown in Fig. 2.6a. We used a tunable laser source with an output power of 0 dBm to calculate the wavelength response of the fiber-UMZI (with attenuator) and chip wavemeter (at port O4) prior to the stability test.

Figure 2.6b shows that the fiber UMZI has an FSR of around 800 MHz and an extinction ratio of around 20 dB. Figure 2.6c depicts the effects of the stability test. The output power difference of the chip wavemeter is less than 0.7 dB, while the output power of the fiber UMZI varies by 16.5 dB. The comparison clearly shows that the fiber UMZI is more susceptible to uncontrollable environmental instabilities, while the integrated wavemeter

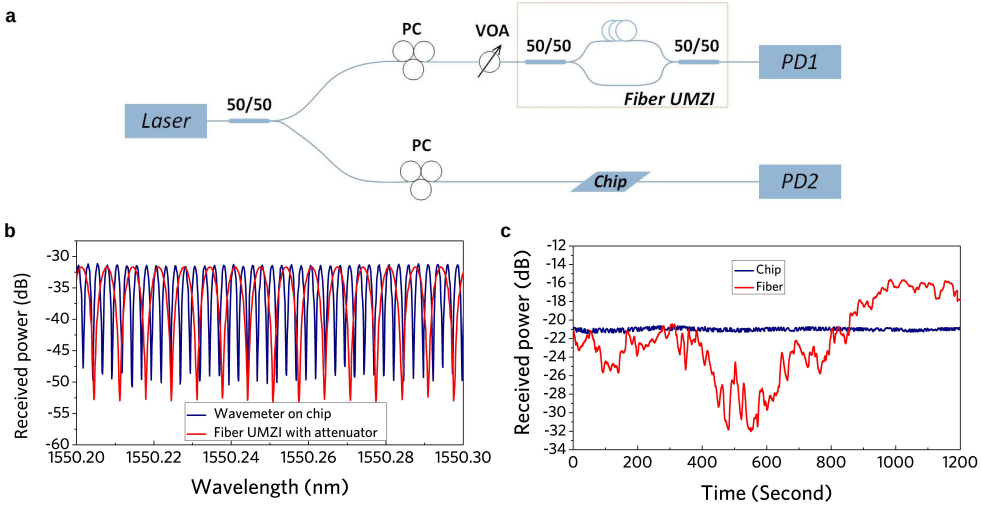

Figure 2.6: At temperatures of 27 °C, 15 °C, 50 °C, normalized output power was measured at various ports of wavemeter. Red curves are sine best fits with phase differences of 0°, 180°, 90°, and -90° from port O1. ©OSA publishing

is far more stable, as anticipated. The Si_3N_4 based wavemeter can be integrated with photodetectors and ultimately with tunable lasers, using the heterogeneous integration techniques developed in this thesis. More details on the integration can be found in following chapters.

The demonstration of integrated Si_3N_4 is a good example of how integrated photonics can improve the photonic device stability over fiber-based devices. When the optical loss is reduced to dB/m scale, a lot of photonic devices which used to be solely on fiber-based systems can be mitigated to chip-based platforms. Ultra low loss Si_3N_4 thus offers compelling solutions for many similar devices.

2.2 Grating-based devices

Waveguide Bragg gratings are widely used in lasers, filters and optical signal processing. Similar as fiber Bragg gratings (FBGs), the grating length and coupling constant κ

are of critical importance as they determines the optical signal delay and thus filtering bandwidth and grating reflectively. A long and narrow-bandwidth grating filter requires low loss and low κ waveguide grating, and the grating insertion loss directly relates to the waveguide loss.

There are several advantages in making low loss, low κ grating on our low-loss thin-core Si_3N_4 platform. The low waveguides loss enables grating length increase without significantly increase the overall loss. Secondly, the optical mode is loosely confided, which offers a lot of room in waveguide perturbation control and κ design. Additionally, the effective modal index if Si_3N_4 waveguide is around 1.47, so based first order Bragg grating condition the grating pitch Λ is around 500 nm for a telecommunication C-band $\lambda_{\text{Bragg}}(\lambda_{\text{Bragg}} = 2n_{\text{eff}}\Lambda)$. This resolution is fully compatible with 248-nm deep ultraviolet (DUV) stepper we are using for optical lithography, instead of using electron beam lithography (EBL) like for Si Bragg gratings. This eliminates the stitching errors in EBL for long gratings and helps maintain a high grating uniformity.

This section will cover Si_3N_4 based grating designs, fabrication and measurements.

2.2.1 Low κ grating

The Si_3N_4 low κ grating is based on same Si_3N_4 waveguide core geometry (Fig. 2.7a). The waveguide perturbation is intended to be weak so a long grating length is possible. So instead of sidewall etch, Si_3N_4 waveguide core is kept unperturbed and Si_3N_4 grating posts are placed on the sides of Si_3N_4 waveguide core (Fig. 2.7b). Figure 2.7c shows SEM image of the fabricated Si_3N_4 low κ Bragg grating.

The grating κ calculation is done by simulating the effective modal index of Si_3N_4 waveguide mode with Si_3N_4 core only (n_{eff1}) and Si_3N_4 waveguide mode with Si_3N_4 post

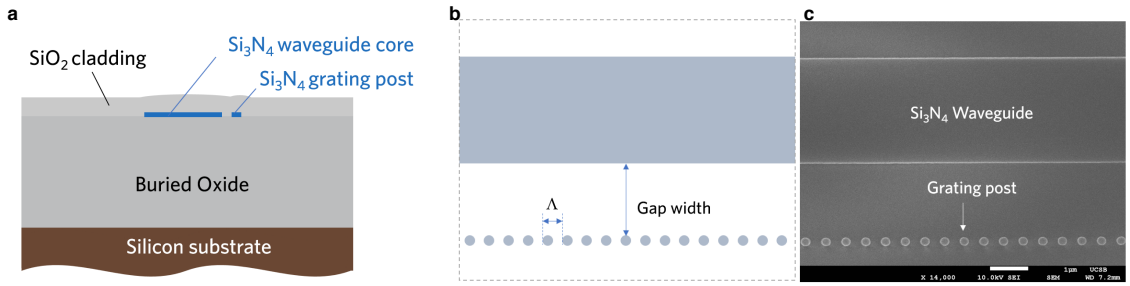

Figure 2.7: a. Cross-sectional view of Si_3N_4 post grating. b. Top-view schematic if Si_3N_4 post grating. c. SEM image of a fabricated Si_3N_4 post grating. ©OSA publishing

(n_{eff2}). The overall effective index of grating is thus determined by

$$n_{\text{eff}} = ff \cdot n_{\text{eff1}} + (1 - ff) \cdot n_{\text{eff2}} \tag{2.1}$$

where ff is the grating fill factor of unperturbed Si_3N_4 waveguide. The grating pitch Λ is thus determined by

$$\Lambda = \frac{\lambda_0}{2n_{\text{eff}}} \tag{2.2}$$

where λ_0 is the Bragg wavelength. The grating κ is calcultated by

$$\kappa = \frac{n_{\text{eff2}} - n_{\text{eff1}}}{n_{\text{eff}} \cdot \Lambda} = \frac{2\Delta n}{\lambda_0} \tag{2.3}$$

Using the method, the grating κ calculation for the grating shown in Fig. 2.7a is plotted in Fig. 2.8. The grating post width is kept at 250 µm in the calculation.

It's clearly evidenced that a large gap width corresponds to a lower κ value. So based on the target grating length, grating bandwidth and grating reflection, the gap width can be tailored to provide desired κ values. Also, it can be noted the double-sided post grating provides a two-times large κ value for the same gap width, as expected.

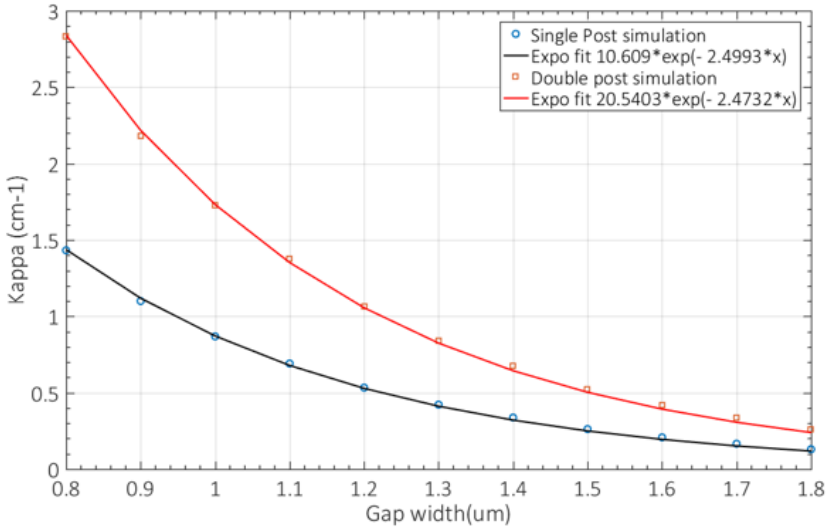

Figure 2.8: Si_3N_4 post grating κ calculation for 2-sided and 1-sided configuration as a function of the gap width.

2.2.2 Spiral grating

As the Si_3N_4 grating lithography is performed with the Si_3N_4 waveguide, grating structures with spiral shapes can be enabled surpassing the physical length limit of mask plate reticle (27 mm). For a spiral grating, one issue to overcome is the bending-dependent modal index change. It is common that for a tighter waveguide bend, the index will decrease due to less mode confinement in the waveguide core. For our thin-core Si_3N_4 waveguide, the mode is loosely confined and the bending radius needs to be kept above approximately 800 µm. We kept the radius change to be small to minimize the effects from radius dependent index change.

For our spiral grating, the first application is for narrow band laser cavity feedback. Thus the grating bandwidth needs to be narrow enough to counteract the narrow cavity mode spacing. The grating loss also plays an important role here since for grating length over 1 centimeter, dB/cm scale loss would result in dB scale loss, significantly degrading the overall power reflectivity and thus the feedback required for lasing. It affects the laser

threshold, laser output power and laser linewidth. Figure 2.9 summarized the influence of waveguide loss on the grating reflectivity, assuming a grating length of 40 mm. It can be noted in order to minimize the insertion loss induced grating reflectivity drop for such a long grating, the waveguide loss is ideally kept below 10 dB/m.

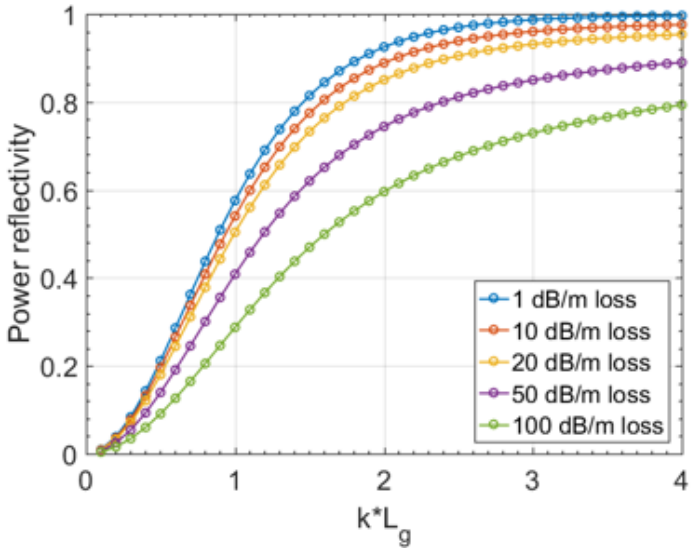

Figure 2.9: Si_3N_4 post grating κ calculation for 2-sided and 1-sided configuration as a function of the gap width.

The longitudinal mode spacing can be calculated by

$$\Delta\lambda = \frac{\lambda^2}{2(n_g L_g + n_{Si} L_{Si} + n_a L_a)} \tag{2.4}$$

where $n_g = 1.57$ and L_g are group index and length of the grating, $n_{Si} = 3.8$ and $L_{Si} = 1mm$ are group index and length of the Si passive waveguide, $n_a = 3.8$ and $L_a = 2.5mm$ are group index and length of the III-V/Si active section. The grating reflection is measured using LUNA Optical Vector Analyzer (OVA) and results are shown in Fig. 2.10. The 40-mm long spiral has a diameter around 7 mm and the 20-mm long spiral has a diameter of around 3.6 mm. Both gratings shown here have a fixed design of $\kappa \cdot L_g = 0.2$.

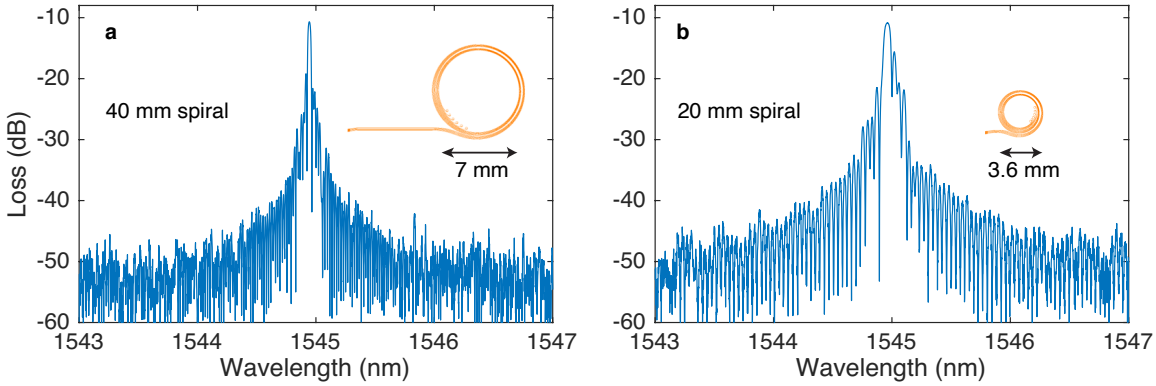

Figure 2.10: Measured grating reflection spectrum for Si_3N_4 grating with a. 40 mm long design and b. 20 mm long design, with a fixed design $\kappa \cdot L_g = 0.2$. The round trip coupling loss is around 10 dB.

Table 2.1 summarizes the performances of the 40-mm long and 20-mm long spiral grating. It can be seen at a same $\kappa \cdot L_g = 0.2$ value for target feedback, the 40-mm ling grating provides narrower filter bandwidth and also higher side lobe suppression, which are advantageous for narrow-linewidth laser applications.

	40-mm spiral grating	20-mm spiral grating
Side lobe suppression	8.5 dB	4.7 dB
3dB bandwidth	25 pm	58 pm

Table 2.1: A summary of the 40-mm long and 20-mm long grating performance.

For each grating length, the grating κ is varied by tailoring the gap with. This results in different grating response and total power reflectivity. Figure 2.11 summarizes the measured grating reflection spectra for different $\kappa \cdot L_g$ designs. It's clearly evident that the strong κ corresponds to a wide grating reflection bandwidth and higher power reflectivity (until reaching unity reflectivity). And overall, a longer grating offers much narrower reflection bandwidth, at the expense of a larger device footprint.

Si_3N_4 provides a platform that enables high-accuracy control waveguide Bragg grating properties. A long Bragg grating can not only offer low κ narrow bandwidth reflection, but also can be used to provide large group delay for optical signals, such as dispersion

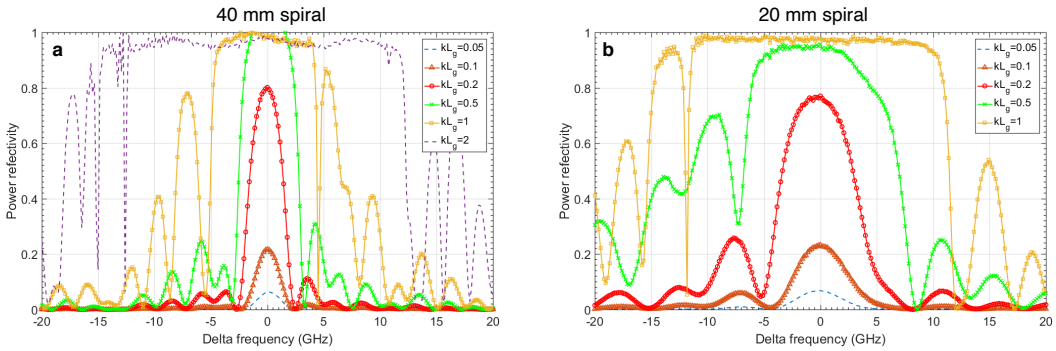

Figure 2.11: Measured grating reflection spectrum for Si_3N_4 grating with a. 40 mm long design and b. 20 mm long design, with a different designs of $\kappa \cdot L_g$.

compensation for mode-locked lasers, and dispersive medium for optical signal processing. Compared with narrow-band low κ grating, large-group-delay grating requires a wide bandwidth instead, while a long grating length with low loss is still preferred [9].

Instead of placing posts along the waveguide core for a low κ, for a large group delay grating, large κ is desired and the waveguide perturbation is achieved by introducing waveguide width difference along the waveguide propagation direction, forming sidewall 'teeth' structures. Figure 2.12 plots the design of sidewall spiral Bragg grating. The Si_3N_4 waveguide is bent from 1.4 mm radius to 800 µm radius. The waveguide core width is $w_0 = 2.8\mu m$ and $w_1 = 3\mu m$. The waveguide spacing between neighboring waveguides are is µm. The grating period is chirped from 531.5 nm to 528.1 nm from the start to the end of the grating. Another chirping effect from the radius change (1400 µm to 800 µm) results in $dn/dz = 3 \times 10^{-5}$.

The grating response is measured using LUNA OVA. The grating length is 13.8 cm and the estimated loss is about 9.5 dB/m so the total 13.8cm long grating results in 2.6 dB insertion loss. The grating reflection and group delay spectra are shown in Fig. 2.13. The red curve (experimental results) and blue curve (simulation results) matched well. 1440 ps group delay with linear wavelength dependence is achieved across a 9.2 nm

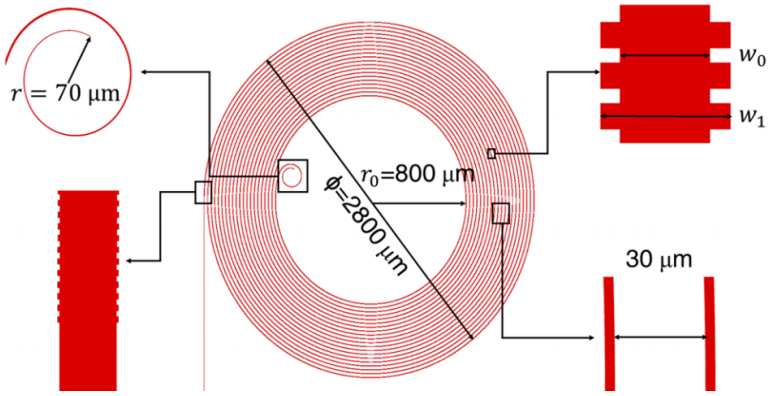

Figure 2.12: Design schematics of the sidewall spiral Bragg grating with large group delay. ©AIP publishing

wide bandwidth. This represents the state-of-the-art performance of large group delay integrated Bragg gratings.

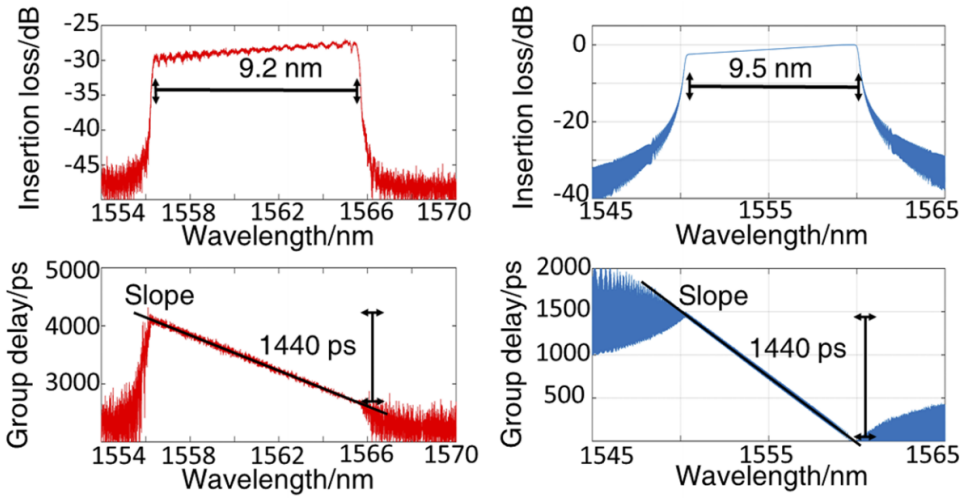

Figure 2.13: Reflection and group delay measurements of the sidewall spiral Bragg grating with large group delay (red) and corresponding simulation results (blue). ©AIP publishing

2.3 Ring-resonators-based devices

Low loss waveguides enable high-Q ring resonator. High-Q ring resonators find wide applications in nonlinear photonics, photonic signal processing and tunable laser. Cas-

caded ring resonators offer a practical route to dynamically control the ring resonator transmission. Optical power transmission and delay response can be controlled at the same time with ring resonance tuning. Here, the deign, measurement and applications for types of cascaded ring resonator devices will be discussed [10].

2.3.1 Tunable time delay lines

Optical signals with frequencies in the hundreds of THz range have a huge amount of bandwidth for carrying microwave signals that modulate the optical carrier's envelope. The optical carrier frequency is just a small percentage of the microwave modulation signal. The photonic system must have a bandwidth greater than the microwave signal of interest because modulation can cause a frequency offset between the carrier wave and the sideband.

In microwave photonic applications, such as phased-array antennas, optical true time delay (TTD) is a critical component[11]. Optical TTD ensures that the wideband frequency components in RF/microwave signals with a broad bandwidth have the same diffraction angle. This prevents phase delay devices from squinting their beams and allows the array to operate without distortion. A tunable TTD is needed for RF beamforming at different diffraction angles in practical electronically scanned phased-array systems. Because of their small scale, enhanced stability, and ease of integration with a laser source and other main functional elements, integrated on-chip optical TTDs are preferred[3].

There are many methods for creating an on-chip tunable optical TTD. The Balanced SCISSOR principle has successfully established a way to achieve a widely tunable optical delay with wide bandwidth and low distortion using side-coupled integrated spaced sequence of resonators (SCISSOR) based devices[12]. The Balanced SCISSOR scheme,

in contrast to cascaded optical switch-based delay lines, which have a small tuning phase scale, provides a continuously tunable delay [13]. Furthermore, since SCISSOR devices use optical resonances, they might be able to reduce the size of TTD devices as compared to those made up of waveguides of equal optical duration. This, however, normally comes at the cost of a limited optical bandwidth while higher frequency signals are often preferred in phased array antenna designs due to wider signal bandwidth support, and more directional beams for a given antenna size.

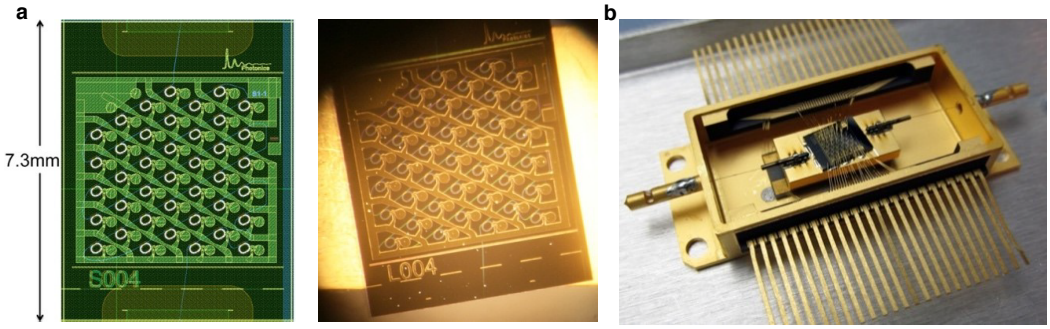

Figure 2.14: a. Photographs of the first-generation 40-microresonator TTD device. b. Packaged microresonator TTD device. ©IEEE publishing

It should be noted that the frequency band between the carrier wave and signal sideband(s) carries no information, so processing the carrier and sideband(s) separately would be advantageous. The separate carrier tuning scheme was proposed and investigated in previous works [14]. This method takes a single sideband signal, provides a TTD for the sideband (with a large signal), and separately provides carrier phase tuning (with a narrowband signal) such that the overall signal appears to have passed through a wideband TTD system. This method improves the performance of optical TTD devices significantly, especially in systems with high modulation frequencies. The improvement is measured in terms of the ratio of sideband bandwidth to sideband frequency; for example, using the separate carrier tuning scheme, a 1 GHz signal bandwidth on a 60 GHz

sideband will result in a 60x improvement in the TTD figure of merit. Since this scheme significantly reduces the bandwidth requirements to the sideband signal of interest, it allows for a much greater feasible delay range for the same delay x bandwidth product. This opens up the possibility of using more refined optical microresonators in optical TTD applications.

Increasing the number of rings in Balanced SCISSOR TTD devices is the approach to get a longer tunable time delay. However, since delay is always proportional to total optical loss, this delay loss is the TTD device's ultimate limiting factor. Furthermore, since sensed RF power increases as the square of optical power, any X dB of optical loss results in 2X dB of RF loss, making loss reduction critical in microwave photonics.

A first-generation of TTD devices based on low loss Si_3N_4 waveguides from the LioniX BV foundry were shown in Fig. 2.14[10]. It uses double strip Si_3N_4 waveguide and can enable around 10 dB/m optical loss with sharp bending radius[15]. However it lacks a clear path for laser and modulator integration. Here we use the developed 90-nm thick thin-core single strip Si_3N_4 waveguide for the new-generation of Si_3N_4 low loss continuously tunable time delay lines.

Figure 2.15 depicts a schematic image of the Si_3N_4 ring based SCISSOR TTD. It has eight racetrack-style ring resonators, all of which are the same size. The straight segment is 380 µm long and the ring radius is 1 mm. An adiabatic bend is used to link the arc ring waveguide and the straight section in order to prevent an abrupt connection. Meanwhile, the bus waveguide leaving the coupling region has the same adiabatic portion.

The ring resonator's total diameter is 7427 µm. To prevent thermal crosstalk, eight rings are mounted in pairs on opposite sides of the bus waveguide. In the coupling field, they have the same gap width as the bus waveguide. The thermal tuners are positioned next to the ring resonator to avoid the coupling region. The fabricated ring resonator is shown in Fig. 2.15b. The calculated waveguide group index is 1.57, and the ring FSR is

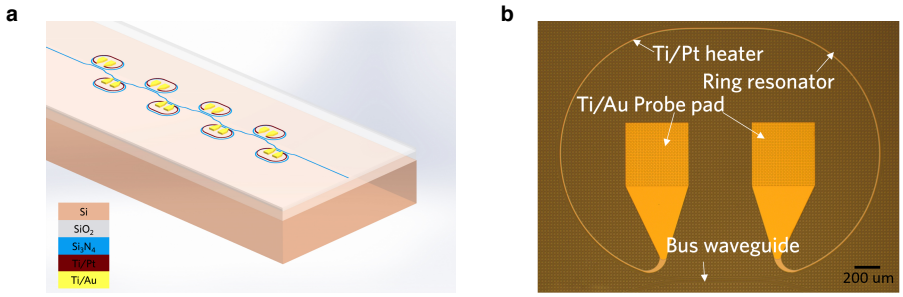

Figure 2.15: a. Schematic illustration of the 8-ring SCISSOR device on 90-nm thick thin-core Si_3N_4 waveguide platform. b. Microscope image of the fabricated Si_3N_4 racetrack ring resonator with tuning heater. ©IEEE publishing

25 GHz.

Figure 2.16 depicts the operation theory of this Balanced SCISSOR tunable TTD, which displays the measured group delay for an 8-ring unit with a coupling constant of 0.8 and the Balanced SCISSOR tuning scheme. The rings are divided into two groups, one of which is blue shifted and the other red shifted during resonance tuning. The group delay indicates a single peak with a broad group delay value but narrower bandwidth when there is no frequency detuning between the two sets of rings. The group delay at the middle frequency decreases as the rings are divided in frequency. The bandwidth of the delay is increased for higher frequency detuning, and the delay form is more flattened. The delay decreases as detuning increases, eventually approaching zero when the detuning value is greater than 7 GHz.

The only variable parameter after the ring resonator dimension is the ring resonator coupling constant κ, which is chosen by changing the coupler gap width. When it comes to ring resonators, it is crucial in deciding the ring spectral shape. Higher finesse is accomplished with smaller κ values, resulting in a narrower bandwidth with longer delay and, sadly, greater loss. Since the TTD system is made up of cascaded identical ring resonators, the overall response will be dependent on the ring coupler when all the rings

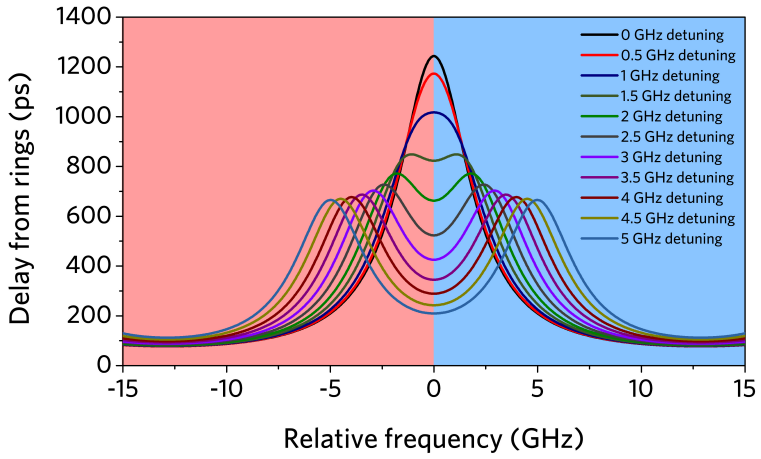

Figure 2.16: Calculated group delay frequency response under varied balanced SCISSOR rings frequency detuning. ©IEEE publishing

are aligned. The dependency of peak delay and delay full width half maximum (FWHM) on κ values is shown in Fig. 2.17.

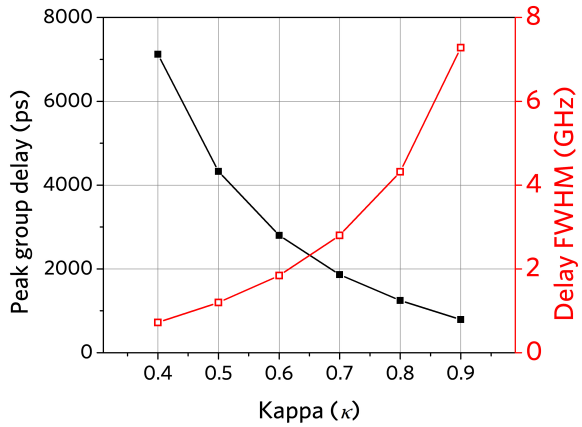

Figure 2.17: Calculated group delay and delay FWHM dependence on the ring coupler κ. ©IEEE publishing

A Luna Optical Vector Analyzer (OVA) is used to characterize the devices. To ensure TE mode operation for all measurements, a polarization controller, polarizer, and polarization maintaining fiber are used. Figure 2.18 shows the measured group delay frequency dependence for the TTD design with $\kappa = 0.715$ when all rings' resonances are aligned. The ring couplers in this unit have a gap width of 2.1 µm. With a 3 GHz FWHM, a

peak delay of 1800 ps is reached. This delay spectrum matches the theoretical estimate very well. Figure 2.18b shows the corresponding normalized transmission calculation. Except for small Fabry-Pérot ripples from chip facet, the loss is only around 1.6 dB at center frequency, and the TTD loss spectrum is proportional to the delay spectrum. A low loss of 0.89 dB/ns is measured using this resonance dip and peak delay value. Since the group index is 1.57, the total loss contribution, including propagation loss, radiation loss, and excess coupler loss, is 4.65 dB/m. The ultra-low loss Si_3N_4 waveguide, as well as the careful nature of adiabatic connections and ring couplers, contribute to this low loss value.

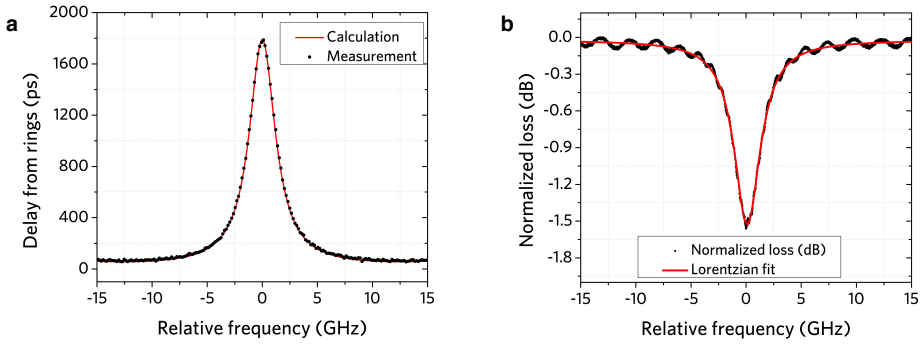

Figure 2.18: Measured group delay (a) and normalized loss (b) versus frequency detuning for TTD design with $\kappa = 0.715$ when all the ring resonances are aligned. ©IEEE publishing

While the peak delay is high when all the ring resonances are aligned, it rolls off rapidly, resulting in a narrow bandwidth. Frequency detuning is used to counteract this. The delay is flattened around the center frequency with 1 GHz detuning using Balanced SCISSOR action, as shown in Fig.2.19. At the same time, the loss at the resonance dip flattens out. An around 1 dB loss is reached, as well as a flattened top with a 1.2 ns group delay. The FWHM is estimated to be 5 GHz, which matches measurements closely. For RF signals with a wide bandwidth, this flattened spectrum will result in significantly less distortion.

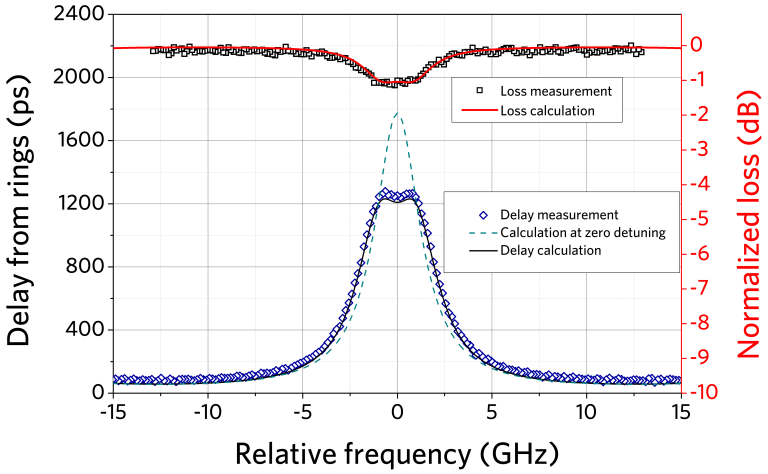

Figure 2.19: Measured group delay and normalized loss versus frequency detuning for SCISSOR design with $\kappa = 0.715$, at 1 GHz frequency detuning. ©IEEE publishing

The operation principle of tunable delay on center frequency is illustrated in Fig. 2.20a. With ring resonator groups tuned away in resonance, the center frequency group delay is thus descreased. Figure 2.20b shows the designed and measured group delay for Balanced SCISSOR activity at different frequency detunings for $\kappa = 0.715$. By varying the frequency detuning from 0 to over 6 GHz, a continuously tunable delay of 1800 ps is demonstrated, with good match with calculation.

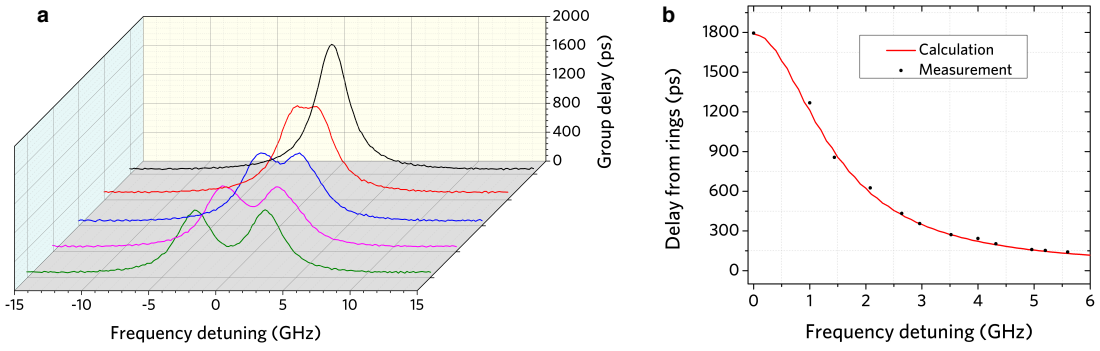

Figure 2.20: a. Tunable delay operation on SCISSOR $\kappa = 0.715$. b. Summarized group delay versus frequency detuning dependence. ©IEEE publishing

Not only the delay value, but also the FWHM shifts as the Balanced SCISSOR resonance is tuned "in" and "out," giving the system some versatility in operation. The

overall achievable delay and the FWHM can both be adjusted to suit various applications once a TTD design is fixed. The design can include a variety of possible delay / FWHM combinations for devices with different values. Only the delay range shift between peak delay and flat top response are listed in Fig. 2.21, which summarizes four designs.

When all the rings are aligned in resonance as shown in the inset, a maximum delay of 3.4 ns is achieved with a configuration with κ of 0.56. The FWHM was extended to 12 GHz for design with $\kappa = 0.91$, at a frequency detuning of 2.5 GHz, with a flat top response of 520 ps group delay over a broad band, with fluctuations within 15 ps. It's also worth noting that the delay bandwidth can be extended by raising the frequency detuning to the point that the two sets of peaks are further separated, allowing the tail of the frequency response to be used. The curve in Fig. 2.16, which has a 5 GHz frequency detuning and a very flat group delay around the middle frequency, demonstrates this trend.

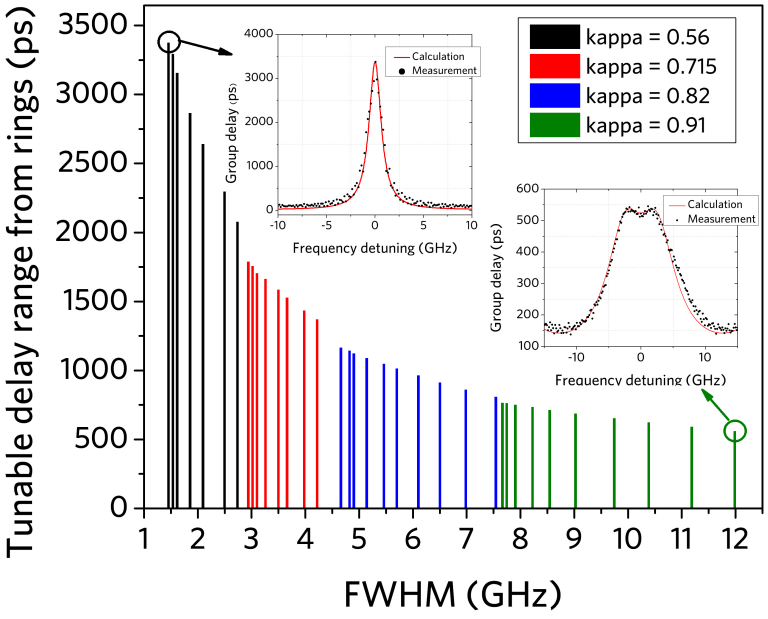

Figure 2.21: A summary of the tunable delay range and FWHM for different κ. ©IEEE publishing

The use of ultra-low loss Si_3N_4 waveguides instead of silicon waveguides for TTD

devices is driven by a desire to reduce the device's total insertion loss. The signal loss from multiple round trips of propagation inside the ring resonator is greatly reduced thanks to the low propagation loss of Si_3N_4 waveguides. Radiation loss due to curvature mismatch can be reduced by carefully designing the adiabatic transition between the straight and bending arc waveguides. However, in addition to the loss inherent in the ring resonator, the ring coupler to the bus waveguide introduces additional loss. This loss is extensively investigated [16], and for a ring resonator with a large value, this loss will contribute significantly to the total loss. As light enters the coupling region from the bus waveguide, the excess loss is caused by mode conversion at the coupling region, and it will rise as the mode mismatch increases. The gap width between the bus waveguide and the ring resonator determines the mode mismatch in most cases. More super eigenmode difference can be seen between the cross-sections A and B depicted in Fig. 2.22a for a smaller distance. Since the transformation can not be perfectly adiabatic over such a short distance, a significant mode conversion loss may occur. The mode mismatch will be reduced as the gap width is increased, and the mode transformation will be more likely to become an adiabatic operation, resulting in a much lower excess loss.

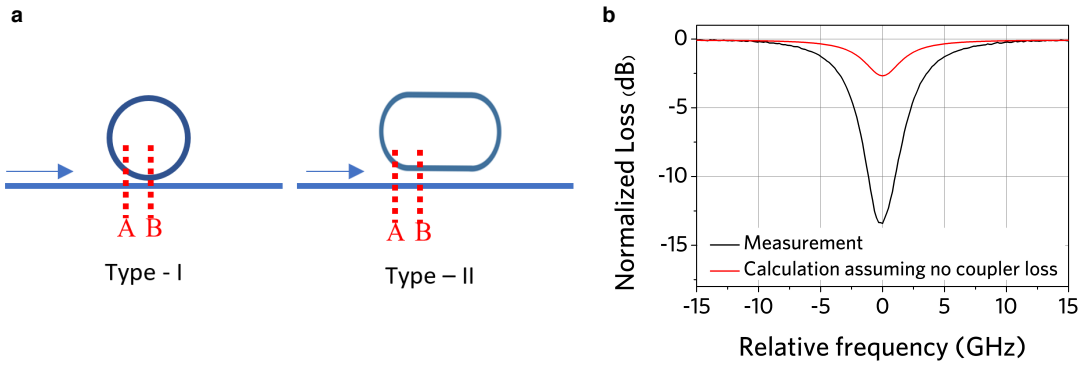

Figure 2.22: a. An illustration comparison of two types of ring couplers with different coupler loss. b. Measurement and calculation of a type-I coupler device. ©IEEE publishing

The type-II racetrack ring couplers used in this study have a much longer coupling

length than a standard curve-straight type-I ring coupler. To obtain the same coupling ratio, this allows for a larger coupling gap width. Figure 2.22b shows the results of a TTD system from a previous run using type-I ring couplers[17]. The total loss can reach 10 dB, despite an independent waveguide loss measurement of only 8 dB/m. In the case of a lossless coupler, an 8 dB/m propagation loss could result in a total loss of just 2.5 dB. This unexpectedly high loss is due to the device's limited gap width (560 nm), which causes excessive coupler loss. A similar value can be achieved in racetrack style designs with a gap width of about 2.1 µm, which significantly decreases the excess coupler loss as well as the device's total loss.

2.3.2 Laser reflectors and filters

Semiconductor lasers with ultra-narrow linewidth are used in high-capacity coherent optical communications, RF photonics, LIDAR, and other optical sensing devices[18]. External cavity lasers with a long external cavity that provides narrowband optical feedback and significantly improve photon lifetime, resulting in a significant reduction in laser linewidth. The reflector should provide adequate optical feedback, i.e. high reflectivity, narrow bandwidth, and high suppression of alternate lasing modes, for an ideal external cavity. Furthermore, tunability over a wide wavelength spectrum would be preferable. In RF photonics and other applications, a wideband tunable laser reflector may also be used as a tunable filter.

Here we use the developed thin-core Si_3N_4 waveguide to build triple-ring and quad-ring reflectors which are featured with low loss, wide tunability, narrow bandwidth and high side mode suppression ratio (SMSR)[19]. Figure 2.23 plots the calculated close-in and wide transmission response for four configurations: 1-Ring, 2-Ring, 3-Ring and 4-Ring. It can be seen that although a 1-Ring filter can provide a narrow bandwidth, it

can only provide a small FSR, so cannot favor single mode lasing conditions. 2-Ring can provide an increased FSR due to the Vernier effect, but for very large ring radius, the close-in side mode suppression ratio is very limited. With an additional high-Q ring, 3-Ring provides much improved close in passive side mode suppression, which would result in a laser with excellent single mode operation. 4-Ring took this one step further, due to it relaxed the requirement on the ring coupler κ value to provide the same optical path length and this could help reduce the in-cavity power density and increase the laser tuning stability.

For the discussed ring-resonators, additional interferometric and phase control structures are required to be used as a laser reflector. As shown in Fig. 2.24, a 2x2 / Mach-Zehnder Interferometer (MZI) tunable directional coupler (DC) cascades three or four ring resonators within a loop mirror. The reflected signal is collected from the same port through the inverse tapers on one of the DC's inputs. The other DC input port is used to control tuning and may be used as an extra laser output in the future. The phase relations of clockwise and counter-clockwise light inside the reflector are regulated by thermal phase tuners on one MZI arm and inside the circle. To prevent unwanted reflections, a platinum heater is used to tune the resonance frequency of each ring resonator, and unwanted ports are terminated by an Euler spiral waveguide terminator. For each configuration, both racetrack and pulley coupler designs are used. Racetrack and pulley couplers have lower coupler loss than straight to curve directional couplers, which helps to minimize the reflector's total loss. For each reflector style, κ is kept as a constant for all the ring couplers.

The ring resonances can be matched and then tuned together by tuning the heaters. The wide-band tuning operation for a 3-Ring-pulley and a 4-Ring-pulley is summarized in Fig. 2.25. A LUNA optical vector analyzer and an optical isolator are used to capture the reflection spectra. When coupling to a reference waveguide, the spectra are normalized

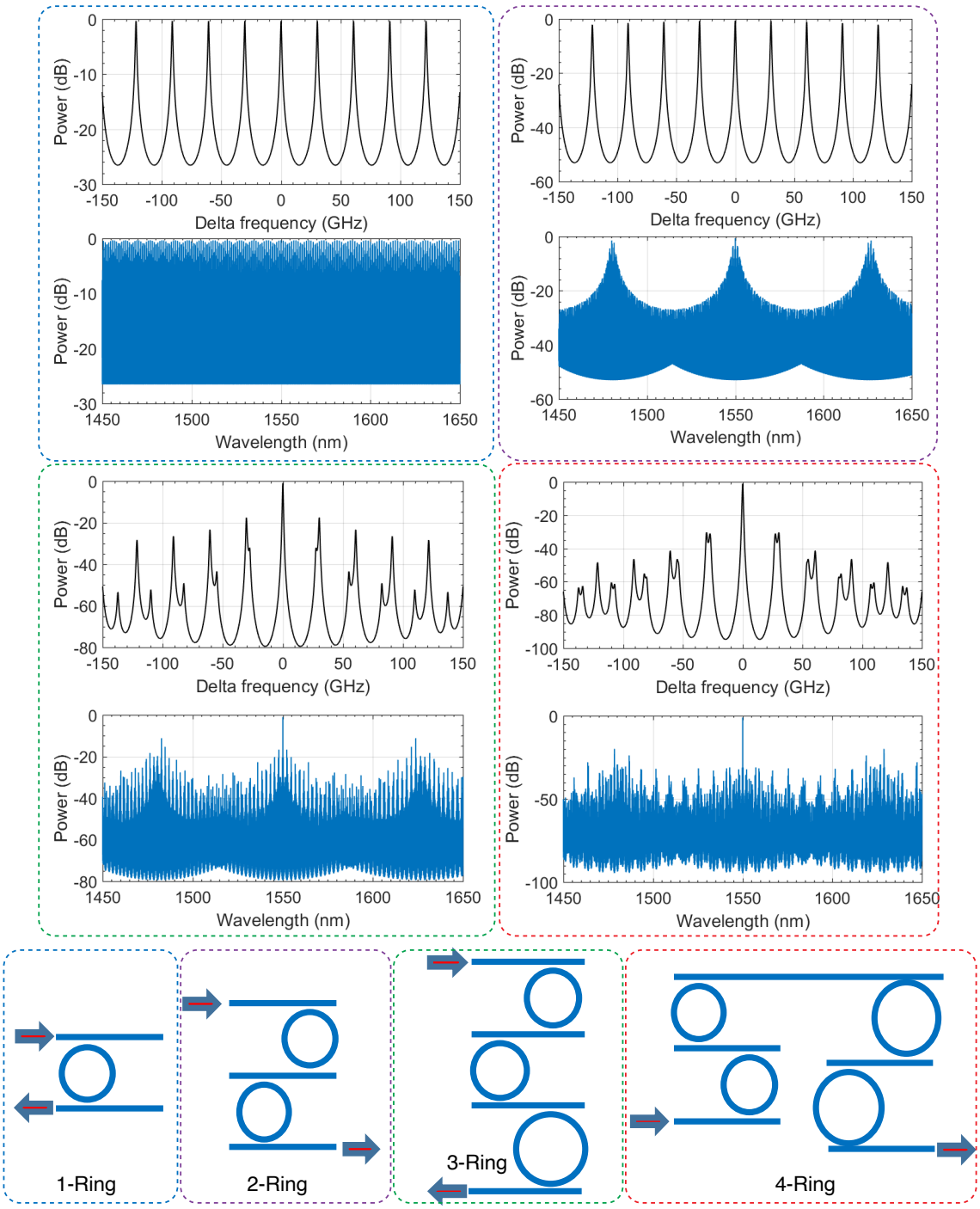

Figure 2.23: Calculated transmission response (top: close in, bottom: wide) of multiple-ring resonators. Blue: 1-Ring, purple: 2-Ring, green: 3-Ring, red: 4-Ring.

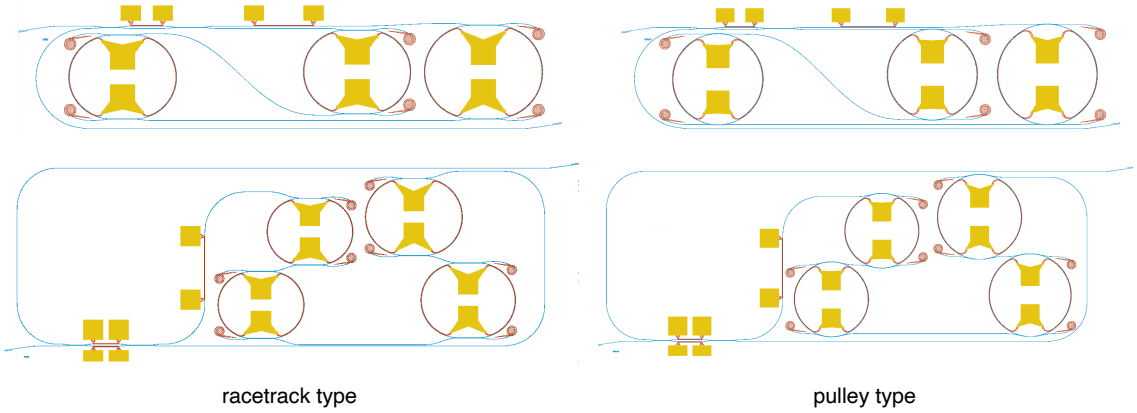

Figure 2.24: Schematic illustration of 3-Ring and 4-Ring based laser reflectors with loop mirror (directional coupler based) and phase tuner. Two types of couple designs are used including racetrack type and pulley type.

to the transmission measurement. All designs have full C-band tunability, indicating that they could be used in a widely tunable laser. Over a broad wavelength range (>80 nm), single peak reflection is also achieved, with varying SMSR calculated for designs with different values. The SMSR is over 7 dB and 12 dB for 3-Ring-racetrack and 3-Ring-pulley devices, respectively.

Due to the additional narrow band filtering provided by the fourth high-Q ring resonator, the SMSR for 4-Ring-racetrack and 4-Ring-pulley designs is increased to over 12 dB and 20 dB, respectively. Fine tuning of the reflector peak is achieved under precise control of ring heaters, as shown in Fig. 2.26a. The reflection is reduced at shorter wavelengths, which may be due to wavelength dependence of the pulley ring coupler and the 2x2 DC. A 4-Ring-pulley reflector, Fig. 2.26b, achieves a minimum 3 dB bandwidth of 2.6 pm (325 MHz), with the potential for lasing linewidth below 10 Hz.

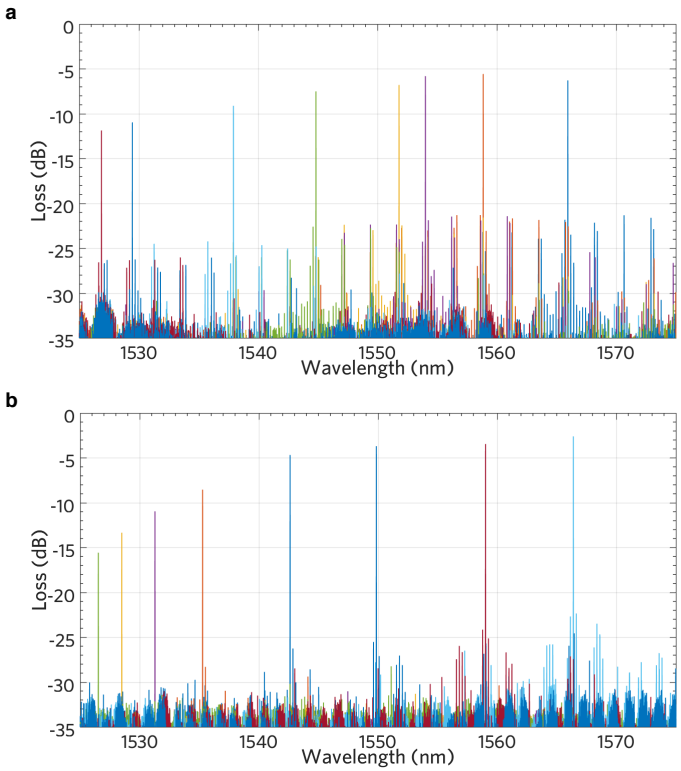

Figure 2.25: Wide tuning of reflection peak for a. 3-Ring with Pulley coupler. $L1 = 6283\mu m, L2 = 6304\mu m, L3 = 6956\mu m, \kappa = 0.3$; b. 4-Ring with Pulley coupler. $L1 = 6283\mu m, L2 = 6304\mu m, L3 = 6956\mu m, L4 = 7140\mu m, \kappa = 0.45$.

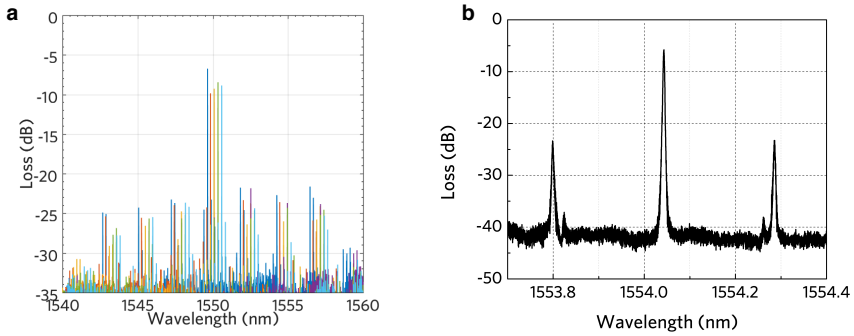

Figure 2.26: a. Fine tuning of reflection peak for 4-Ring with Pulley coupler. b. Close in look of reflection peak with > 15 dB passive SMSR. The ring parameters are $L1 = 6283\mu m, L2 = 6304\mu m, L3 = 6956\mu m, L4 = 7140\mu m, \kappa = 0.45$.

2.4 Summary

In summary, this chapter discussed the developments of various passive devices on low loss Si_3N_4 waveguide platform including wavemeter, low κ grating, spiral grating with large group delay, ring-resonator-based tunable time delay line and ring-resonator-based laser reflectors and filters. These devices, not only play important roles in stand-alone passive Si_3N_4 based devices, but also offer great potentials to be integrated by hybrid or heterogeneous methods with III-V materials for improved integrated laser performances. The laser integration of several key devices will be covered in the following chapters.

References

[1] M. A. Tran, D. Huang, and J. E. Bowers, *Tutorial on narrow linewidth tunable semiconductor lasers using si/iii-v heterogeneous integration*, *APL photonics* **4** (2019), no. 11 111101.

[2] D. J. Moss, R. Morandotti, A. L. Gaeta, and M. Lipson, *New cmos-compatible platforms based on silicon nitride and hydex for nonlinear optics*, *Nature Photonics* **7** (07, 2013) 597.

[3] D. Marpaung, C. Roeloffzen, R. Heideman, A. Leinse, S. Sales, and J. Capmany, *Integrated microwave photonics*, *Laser & Photonics Reviews* **7** (2019/01/16, 2013) 506–538.

[4] J. F. Bauters, M. J. R. Heck, D. D. John, J. S. Barton, C. M. Bruinink, A. Leinse, R. G. Heideman, D. J. Blumenthal, and J. E. Bowers, *Planar waveguides with less than 0.1 db/m propagation loss fabricated with wafer bonding*, *Opt. Express* **19** (Nov, 2011) 24090–24101.

[5] M. W. Puckett, K. Liu, N. Chauhan, Q. Zhao, N. Jin, H. Cheng, J. Wu, R. O. Behunin, P. T. Rakich, K. D. Nelson, *et. al.*, *422 million intrinsic quality factor planar integrated all-waveguide resonator with sub-mhz linewidth*, *Nature communications* **12** (2021), no. 1 1–8.

[6] J. F. Bauters, M. J. Heck, D. D. John, J. S. Barton, C. M. Bruinink, A. Leinse, R. G. Heideman, D. J. Blumenthal, and J. E. Bowers, *Planar waveguides with less than 0.1 db/m propagation loss fabricated with wafer bonding*, *Optics Express* **19** (2011), no. 24 24090–24101.

[7] C. Xiang, M. A. Tran, T. Komljenovic, J. Hulme, M. Davenport, D. Baney, B. Szafraniec, and J. E. Bowers, *Integrated chip-scale Si_3N_4 wavemeter with narrow free spectral range and high stability*, *Optics Letters* **41** (2016), no. 14 3309–3312.

[8] J. F. Bauters, M. Heck, D. Dai, J. Barton, D. Blumenthal, and J. Bowers, *Ultralow-loss planar Si_3N_4 waveguide polarizers*, *IEEE Photonics Journal* **5** (2012), no. 1 6600207–6600207.

[9] Z. Du, C. Xiang, T. Fu, M. Chen, S. Yang, J. E. Bowers, and H. Chen, *Silicon nitride chirped spiral Bragg grating with large group delay*, *APL Photonics* **5** (2020), no. 10 101302.

[10] C. Xiang, M. L. Davenport, J. B. Khurgin, P. A. Morton, and J. E. Bowers, *Low-loss continuously tunable optical true time delay based on Si_3N_4 ring resonators*, *IEEE Journal of Selected Topics in Quantum Electronics* **24** (2017), no. 4 1–9.

[11] I. Frigyes and A. Seeds, *Optically generated true-time delay in phased-array antennas*, *IEEE Transactions on Microwave Theory and Techniques* **43** (1995), no. 9 2378–2386.

[12] J. B. Khurgin, *Expanding the bandwidth of slow-light photonic devices based on coupled resonators*, *Optics Letters* **30** (2005), no. 5 513–515.

[13] J. Cardenas, M. A. Foster, N. Sherwood-Droz, C. B. Poitras, H. L. Lira, B. Zhang, A. L. Gaeta, J. B. Khurgin, P. Morton, and M. Lipson, *Wide-bandwidth continuously tunable optical delay line using silicon microring resonators*, *Optics Express* **18** (2010), no. 25 26525–26534.

[14] P. A. Morton and J. B. Khurgin, *Microwave photonic delay line with separate tuning of the optical carrier*, *IEEE Photonics Technology Letters* **21** (2009), no. 22 1686–1688.

[15] L. Zhuang, D. Marpaung, M. Burla, W. Beeker, A. Leinse, and C. Roeloffzen, *Low-loss, high-index-contrast Si_3N_4/sio 2 optical waveguides for optical delay lines in microwave photonics signal processing*, *Optics Express* **19** (2011), no. 23 23162–23170.

[16] F. Xia, L. Sekaric, and Y. A. Vlasov, *Mode conversion losses in silicon-on-insulator photonic wire based racetrack resonators*, *Optics Express* **14** (2006), no. 9 3872–3886.

[17] C. Xiang, M. L. Davenport, J. B. Khurgin, P. A. Morton, and J. E. Bowers, *Tunable optical delay line based on Si_3N_4 ring resonators*, in *2017 IEEE Photonics Conference (IPC)*, pp. 119–120, IEEE, 2017.

[18] P. A. Morton and M. J. Morton, *High-power, ultra-low noise hybrid lasers for microwave photonics and optical sensing*, *J. Lightwave Technol.* **36** (Nov, 2018) 5048–5057.

[19] C. Xiang, P. A. Morton, J. Khurgin, C. Morton, and J. E. Bowers, *Widely tunable Si_3N_4 triple-ring and quad-ring resonator laser reflectors and filters*, in *2018 IEEE 15th International Conference on Group IV Photonics (GFP)*, pp. 1–2, IEEE, 2018.

Chapter 3

Narrow linewidth hybrid integrated lasers

A narrow-linewidth lasers plays important roles in high-capacity coherent optical transmission system, high spurious free dynamic range (SFDR) analog optic links, remote sensing and so on. State-of-the-art narrow-linewidth lasers are based on bulky solid-state lasers and fiber lasers.

Semiconductor lasers have the benefits of much reduced size, weight, power consumption and cost (SWaPC). However, they are vulnerable to the high spontaneous emission (ASE) induced laser phase noise. Typical monolithic III-V based lasers are with linewidth on the orders of MHz. Recent progress of external cavity based semiconductor lasers reduced fundamental linewidth down to 10 Hz regime. Heterogeneous integration, which provides the direct on chip integration of low loss Si waveguides with III-V gain materials, are also pushing its linewidth down below 100 Hz too.

This chapter will first introduce the theory of semiconductor laser linewidth, and give a mini review of recent progress on narrow linewidth semiconductor lasers using hybrid and heterogeneous integration. Then nonlinear loss of Si waveguide which limits the

performance of narrow-linewidth lasers will be discussed and show that silicon nitride based lasers are advantageous in terms of high power and narrow linewidth operation. After that, the developments and results of a hybrid integrated narrow-linewidth E-DBR laser based on silicon nitride low κ Bragg grating will be covered.

3.1 Narrow-linewidth integrated lasers: a brief review

Since the early developments of semiconductor lasers, the linewidth reduction remains as a big concern because telecommunication - the most important application for semiconductor lasers - sets a high requirement on the laser linewidth. This requirement evolves with the adoption of more advanced modulation formats and higher transmission data rates. It has been experimentally demonstrated that, for square 64-QAM (quadrature amplitude modulation) at 40 Gb/s, the required laser linewidth is $\sim$ 1 KHz, which is 100x narrower than the requirement of square 16-QAM. As the linewidth requirement keeps increasing, conventional monolithic III-V semiconductor lasers with MHz-range linewidth are not suitable to keep up with the trend.

For monolithic III-V lasers, the Schawlow-Townes linewidth [1] and its Henry correction factor due to linewidth-enhancement factor α of semiconductors [2] have been studied decades ago. It has also been pointed out early that, the laser linewidth has narrowing effect due to passive external cavity and negative optical feedback [3; 4]. Based on these theories, decades developments improved the experimental linewidth results from 100 MHz to 0.5 MHz. These results, targeting at telecommunication applications, use quantum-well epi structures.

The typical linewidth enhancement factor α of quantum well is around 2 to 6. The

linewidth will see a broadening factor of $1 + \alpha^2$. This clearly implies that if α can be reduced to be lower than 1, it can result in another order of magnitude reduction in the laser linewidth, purely from the gain material. Quantum-dots (QDs) are with a small α factor and recent works on the development of monolithic QD-based DFB lasers and SG-DBR (sampled-grating distributed Bragg reflector) lasers achieved minimum linewidth of 30 kHz and 6 KHz respectively. However, this decrease is now at its bottleneck due to the external III-V waveguide cavity loss is still too high ($>$ 1 dB/cm).

Compared with III-V waveguides, Si waveguides has much 10-100 times lower loss, thus enabling 10x-100x increases in the feedback cavity without sacrificing on laser output power and lasing threshold. Si_3N_4 waveguides, as descried in previous chapter, enable ultra low propagation loss and typically can enable below 0.1 dB/cm waveguide loss and is down to below 1dB/m with a record of $\sim$ 0.045 dB/m. Thus the integration with Si_3N_4 waveguides represents the state-of-the art integrated narrow linewidth laser performance.

Hybrid integration, which refers to using butt-coupling of laser gain chip with external integrated passive cavity is an approach that allows the separate optimization of laser gain material and laser cavity design[5]. Also, compared with heterogeneous integration, it doesn't impose process compatibility issues so it's an easier approach to achieve a good laser performance with quicker turnaround time. However the coupling loss is usually high and limit the device performance. Also the packaging needs to be robust to improve the laser long-term stability.

Heterogeneous integration enables wafer-scale production of narrow-linewidth lasers and avoids the complicated and high-cost optical packaging of separate chips. However, to heterogeneously integrate the laser gain with low loss Si_3N_4 waveguides is challenging due to the large index mismatch in between. So III-V/Si heterogeneous lasers are the first generations of narrow-linewidth lasers using heterogeneous integration. Recent progress in multilayer heterogeneous integration (one focus of this thesis) developed integration

techniques for III-V gain materials with Si_3N_4 low-loss waveguides and the linewidth performance is approaching to the state-of-the art hybrid integrated lasers.

Figure 3.1 summarizes the progression of integrated semiconductor laser linewidth performances. Three categories are compared based on the integration platforms, i.e. monolithic III-V, hybrid integration and heterogeneous integration. The clear trend is monolithic integration is limited to above 10 kHz range, while hybrid integration currently holds the record linewidth performance. Heterogeneous integration, with improvement in the fabrication process is approaching the hybrid integration performance. State-of-the-art heterogeneously integrated lasers are having linewidth below 100 Hz based on the device operation approach.

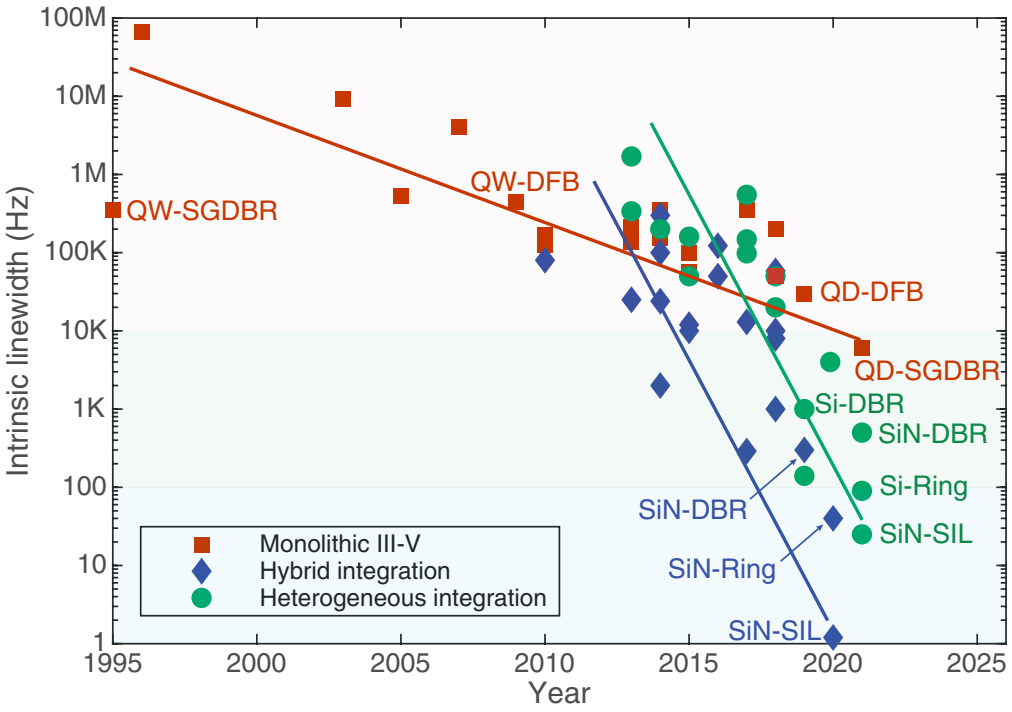

Figure 3.1: Integrated semiconductor laser linewidth progression. ©AIP publishing

More information can be concluded from Fig. 3.1. For monolithic lasers, SG-DBR laser is having narrower linewidth than DFB laser thanks to the passive waveguide. The

linewidth performance is improved by replacing QW with QD in recent years. For hybrid and heterogeneous integration, Si_3N_4 is performing better than Si due to the lower loss. The operation principle of narrow-linewidth laser is mostly based on three approaches:

1. Distributed Bragg grating (DBR)
2. Ring-resonator external cavity (Ring)
3. Self-injection locking (SIL)

Among these approaches, the key is the effective cavity length or optical delay time. Bragg grating can provides a narrow-bandwidth and long cavity length feedback but the effective length is limited by its physical length. Ring resonators are resonant structures and the effective length can thus be increased to be beyond the size limit. However, it requires additional filtering of the longitudinal mode and thus multiple ring resonators need to be employed thus complicating the laser tuning operation. However it increases the photon lifetime by high-Q structures and thus reduces the laser linewidth more than the grating-based cavity with similar physical size. Self-injection locking, on the other hand, is to utilize ultra-high-Q structure to do selective feedback of an existing laser line. This results in orders of magnitude laser phase noise reduction and doesn't require a high feedback signal level[6–9]. Hybrid integration with SIL is achieving Hertz-level laser intrinsic linewidth and heterogeneous integration of III-V/Si DFB lasers and high-Q Si_3N_4 ring resonators enables a 25 Hz intrinsic linewidth recently. The developments of heterogeneous integration with Si_3N_4 will be covered in Chapter 4 and 5, while this chapter focuses on the design and developments of Si_3N_4 cavity and a proof-of-concept demonstration using hybrid integration.

3.2 Nonlinear loss in high-Q Si rings

As extensively discussed, low loss is the key in the linewidth narrowing in heterogeneous and hybrid integrated lasers. This loss, not only includes the optical propagation loss depending on the waveguide material, structures, and fabrication control, but also includes any power-dependent nonlinear loss which is overlooked in many related researches. This section will study the nonlinear loss in high-Q Si ring resonators and its limitation in narrow-linewdith laser applications. And as a solution, extended Si ring resonators and ideally Si_3N_4 ring resonators can be adopted to surpass the nonlinear loss limitation[10].

The invention of a laser cavity with an integrated low-loss Si waveguide is at the heart of the advancement of heterogeneously integrated III-V/Si lasers. A low-loss Si waveguide can be used to build a laser cavity with a much higher quality factor (Q), extending the photon lifetime and thus increasing laser coherence. Latest reports of lasers with fundamental linewidth on the order of 100 Hz depend heavily on ultra-low loss Si waveguides with optical losses ranging from 0.1 dB/cm to 1 dB/cm[11; 12].

High-Q Si ring resonators are used as an external cavity in many of these systems to provide narrow-band optical feedback and wide-band wavelength tuning. The output power, tuning range, and linewidth of such a tunable laser are largely determined by the design of cascaded ring resonators. When designing low-loss Si waveguides and high-Q rings for a high-performance tunable laser, however, the focus was primarily on passive performance, with parasitic limitations in the laser system being overlooked. Since the modified Schawlow-Townes linewidth scales with 1/P, a narrow linewidth laser favors high output power. A Si ring resonator's output at remarkably high-power levels will vary from its own 'cold-cavity' performance at low-power levels, where its passive performance is normally described. Although a high Q-factor increases photon lifetime

and benefits laser coherence, it also increases the power level inside the ring resonator. For a ring resonator with a fixed dimension, this power build-up scales up with increased Q-factor[13; 14]. However, since Si has a strong two-photon absorption (TPA) coefficient (TPA= 5 x 10^{-12} m/W at 1.55 µm [15]), free carriers are produced at high power levels, resulting in free carrier absorption (FCA). As a result of the increased nonlinear loss at high power levels, the ring resonator Q-factor decreases. Although one of the main advantages of silicon photonic waveguides is their small size due to the high index contrast with the cladding material, their design must account for nonlinear loss in addition to its cold-cavity performances.

Si ring resonators are made on 100-mm-diameter silicon-on-insulator (SOI) wafers. Figure 3.2 shows the cross section of a fabricated ring resonator at the bus waveguide to ring waveguide coupling field. The buried SiO_2 layer is 1 µm thick, with a total thickness of 500 nm for the Si waveguide layer. The etch depth, as well as the Si width in the bus waveguide (W_{bus}), can be customized to allow single mode and multimode waveguides (Wring). Deep-UV lithography is used to create the device, which is then accompanied by photoresist reflow to minimize line roughness. C4F8/SF6 based reactive ion etch etching is used for waveguide etching, which is supported by a laser etch monitor for precise etch depth control. The waveguide top cladding is then made of 620 nm thick PECVD SiO_2.

This set of ring resonators has 231 nm etch depth with an all-pass configuration and the top-view schematic is shown in Fig. 3.2 b and c. With a ring radius of 100 µm, two types of bus-ring waveguide couplers are used: pulley-type (Fig.3.2 b) and parallel waveguide racetrack-type (Fig.3.2 c). Coupler loss is reduced in these two forms of couplers, and all straight to bend structures are rendered adiabatic to reduce transition loss. The bus waveguide width is 960 nm, and the ring waveguide width is 2.06 µm for the pulley-type ring, which is multimode and supports three transverse-electric modes (TE0, TE1 and TE2). The racetrack-style ring has a bus and ring waveguide that are

1.07 µm wide. At a bend radius of 100 µm, it is quasi-single mode, with only TE0 mode visible in the transmission spectrum. Figure 3.2d shows the simulated fundamental mode effective area as a function of W_{ring} for a bend radius of 100 µm. The effective mode area for a ring waveguide width of 2.06 µm and 1.07 µm wide waveguide is 0.65 µm^2 and 0.42 µm^2, respectively. Since the mode overlaps with the etched sidewall differently depending on the waveguide distance, the Q-factor varies. Figures 3.2e and f show one TE0 mode resonance for each ring design, for multimode pulley ring and quasi-single mode racetrack ring resonators, respectively, with fitted intrinsic Q-factors (Q_0) of 2.4 x 10^6 and 1.1 x 10^6 respectively.

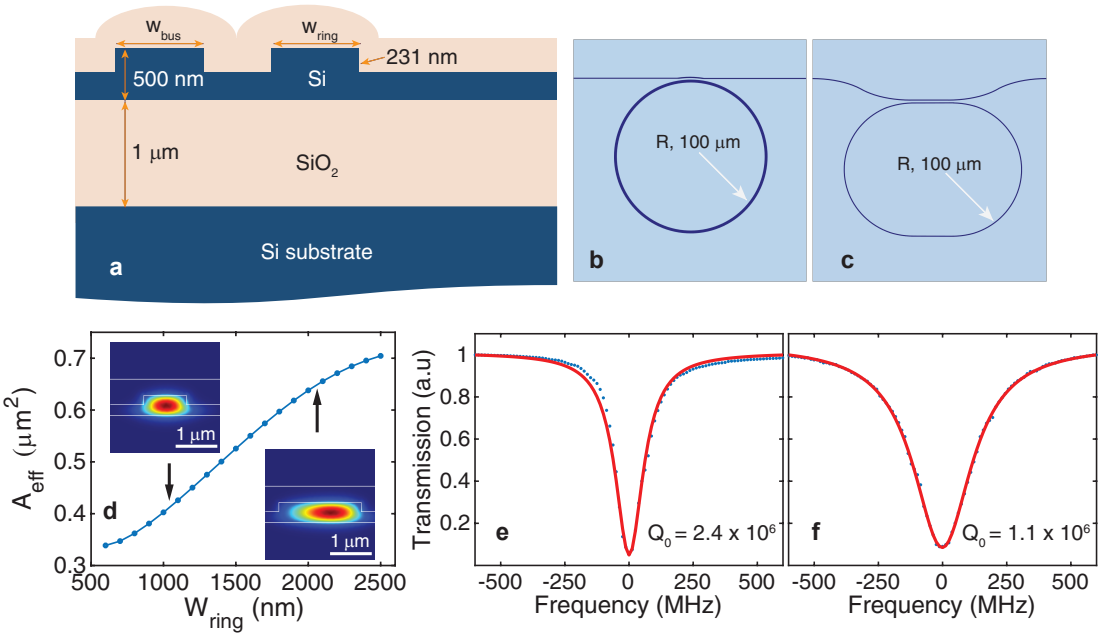

Figure 3.2: a. Schematics of the Si ring resonator's cross section at the bus-ring coupling area. Top-view schematics of the pulley-type (b) and racetrack-type ring resonators (c). d. Effective mode area of the Si waveguide simulated at a bend radius of 100 µm. The simulated Si mode profile with two different ring waveguide widths is shown in the insets. e,f. Fitted TE0 mode resonance of a pulley multimode ring resonator and a racetrack quasi-single mode ring resonator, respectively. The measurements are shown in blue, while the Lorentzian fit is shown in red. ©OSA publishing

In the Si bus waveguide, the Q-factor measurement is done with -17 dBm power. The low bus waveguide power ensures that the transmission spectrum is not skewed. Cold-cavity Q_{0c} refers to the intrinsic Q-factor at low input power. High Q-factor also leads to high intracavity power strength since the power build-up within the ring resonator scales up with the ring Q-factor. For the fabricated rings, we measured the power-dependent transmission spectrum. An Agilent 81960A/81680A tunable laser and an Agilent 81635A power sensor are used to make the measurement. For each sweep, the ring resonance is swept from a short wavelength to a long wavelength. During each sweep, the Agilent 8164B or Agilent 8163B Lightwave Multimeter's built-in wavemeter corrects the absolute wavelength results. The measurement results of a pulley form multimode ring with Q_{0c} = 1.7 x 10^6 are shown in Figure 2(a). Due to proportional index change from absorptive heating and Kerr nonlinearity as the intracavity power intensity increases, the measured ring resonance red shifts as a function of the power in the bus waveguide as the input power is increased during each sweep. When the power in the bus waveguide is above -10 dBm, the resonator's shape is Lorentzian at low power levels, but it becomes a non-Lorentzian, triangular shape at high power levels. As the laser scan wavelength is red detuned, the combined effect of thermal refractive index change and Kerr nonlinear index change causes this [25]. As the laser sweep wavelength crosses the effective resonance wavelength, the intracavity power drops rapidly, followed by a resonance blue change, resulting in a rapid increase in transmitted power to the off-resonance state.

Since the resonator transmission is no longer Lorentzian in shape, Lorentzian fitting for high-power levels is no longer valid. The minimum normalized transmission at resonance wavelength of a sweep, on the other hand, increases as the sweep input power increases, as shown in Fig. 3.3a. This means that at high input power levels, additional power is lost inside the cavity system under steady state where the coupler coupling strength is set[16]. The bus-ring waveguide cavity system can be represented using three

quality factors in all circumstances, similar to high-Q microdisk resonators: Q_l (loaded Q), Q_0 (intrinsic Q), and Q_c (coupler Q). These Q factors are related by

$$\frac{1}{Q_l} = \frac{1}{Q_0} + \frac{1}{Q_c} \tag{3.1}$$

At cold cavity condition, this can be written as

$$\frac{1}{Q_{lc}} = \frac{1}{Q_{0c}} + \frac{1}{Q_{cc}} \tag{3.2}$$

The Q_{lc}, Q_{0c} and Q_{cc} at cold cavity condition by Lorentzian fitting. The relation

$$Q_c = \frac{2Q_l}{1 - \sqrt{T_{min}}} \tag{3.3}$$

and

$$Q_0 = \frac{2Q_c(1 - \sqrt{T_{min}})}{1 + \sqrt{T_{min}}} \tag{3.4}$$

hold for all conditions with different power in the bus waveguide. At steady state $Q_c = Q_{cc}$ and Q_c is fixed. So it's straightforward to extract the different Q_0 at different powers using equation 3.4.

The cold-cavity finesse for this resonator is around 650, and the power strength in the ring resonator is calculated to be around 200 mW/µm^2 with 6.5 dBm bus waveguide power.

The thermal red shift and the free carrier dispersion (FCD) blue shift combine to produce the resonance shift. The free carrier density produced by the TPA process in Si ring waveguide determines the FCD blue change. It is shown that the 23 pm resonance shift with 6.5 dBm bus waveguide results from the thermal red shift of 46 pm and FCD blue shift of 23 pm with FCD induced index change of - 4.75 x 10^{-5} using equations

describing the strength dependent TPA and FCA processes. If we assume a 23 ns free carrier lifetime and a temperature increase of 0.5 K, the free carrier density is around 1.4 x 10^{16} /cm^3 [17]. The coupler Q_c can be considered as a constant in the study because of the slight temperature change. The calculated thermal impedance is approximately 277 K/W. The total loss is made up of three components: linear loss (α_l), TPA loss ($\alpha_{TPA} = \beta_{TPA} \cdot I$), and FCA loss ($\alpha_{FCA} = \sigma \cdot N_{FC}$), where I is the power strength, σ is the FCA cross section, and N_{FC} is the free carrier density.

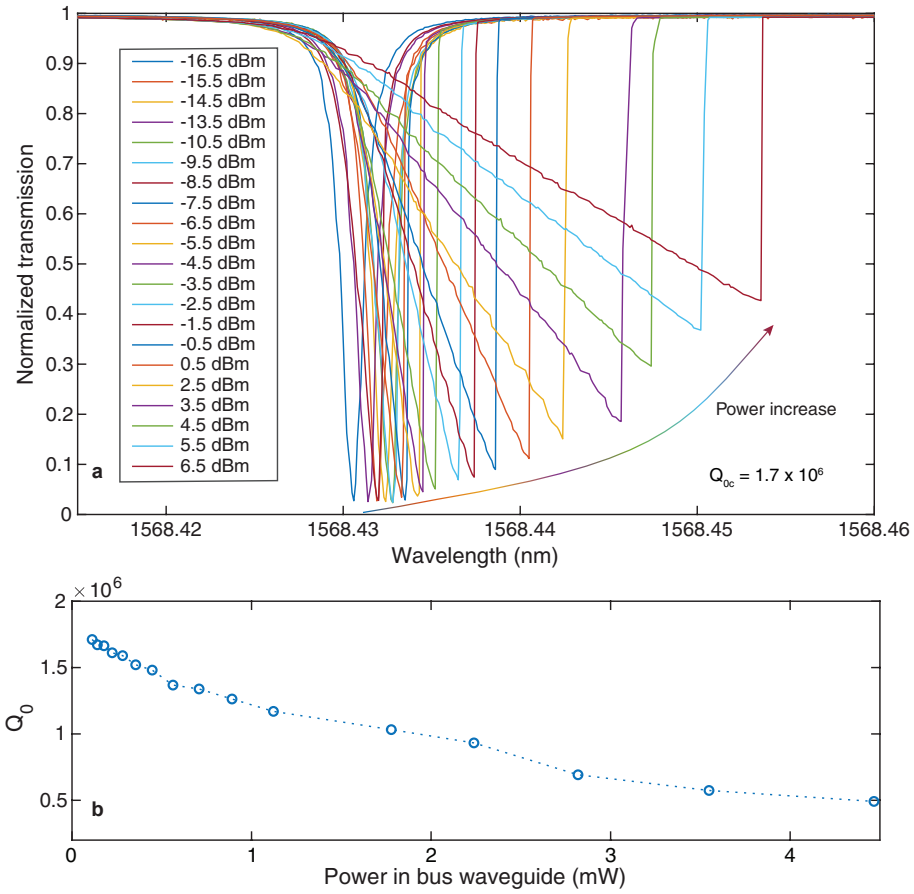

Figure 3.3: a. Normalized transmission for a multimode pulley-ring Si resonator with $Q_{0c} = 1.7 \times 10^6$ at various bus waveguide powers, as shown in the legend. b. Power-dependent intrinsic Q-factor extracted from a. ©OSA publishing

Figure 3.3b shows the extracted intrinsic Q-factor with respect to different power

levels. With increased power in the bus waveguide, the intrinsic Q-factor drops dramatically. In the bus waveguide, Q_0 decreases to around 0.5 x 10^6 at 4.5 mW capacity, a 3x reduction over Q_{0c} in the cold cavity. When Q_0 drops to half of Q_{0c} in a bus waveguide at 2.5 mW power, nonlinear loss begins to dominate. This is due to the high intracavity power build-up, which is a product of the high Q-factor and large free-spectral-range combined effect (FSR, 1.044 nm). Since the nonlinear loss is dependent on the same intracavity power intensity, our conclusion still holds for an add-drop ring resonator. For a ring resonator used in tunable lasers, this large Q-factor drop will greatly deteriorate the laser performance, in terms of both output power and laser linewidth.

A high-Q ring resonator for use in a narrow-linewidth external cavity laser must have a long group delay, i.e. a wide effective cavity length, to reduce the adjusted Schawlow-Townes linewidth[3]. In a heterogeneously integrated external cavity laser, the passive/active section length ratio is critical in determining the necessary ring resonator dimension. Both the power coupling strength (κ) and the physical radius R of the ring resonator determine the effective length: $L_{eff} = 2\pi R(1-\kappa)/\kappa$. So, in addition to changing the κ, increasing the physical size of the ring resonator is an alternative way to increase the effective length.

We made a new group of Si ring resonators with a different etch depth and ring radius. Both the bus and ring waveguides now have a 1.8 µm width. As shown in Figs. 3.4a and b, the etch depth is reduced to 56 nm, and the ring radius is increased to 849 µm, 711 µm, and 600 µm, respectively. The respective gap width between the waveguide and the ring for the three ring resonators sharing the same bus waveguide is tailored to maintain a similar coupling coefficient. After a fast photodetector, the transmission spectrum is captured by sweeping an Agilent 81608A tunable laser and recording the obtained voltage signal from an oscilloscope. Figure 3.4c depicts the measurement findings. The grouped resonance wavelengths are grouped by different FSRs corresponding to different

ring radius in Fig. 3.4d.

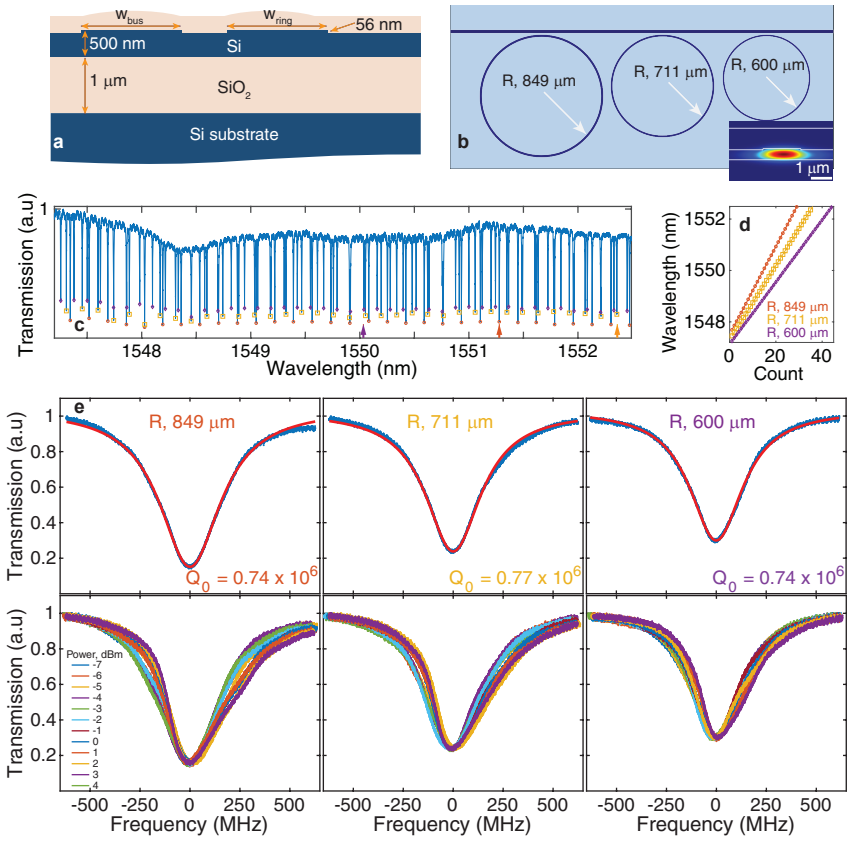

Figure 3.4: (a) Cross-sectional view schematics of cross-sectional view of the extended Si ring resonator at the bus-ring coupling region. (b) Top-view schematics of three extended ring resonators sharing a common bus waveguide. (c) Transmission spectra measured from the common bus waveguide showing three group of resonances of the rings in (b). (d) Resonance wavelengths separated from (c), grouped by ring radius. (e) Fitted TE0 mode resonance of extended ring resonators with difference ring radius. The measured resonance is marked with corresponding colors in (c). The top row is measurements at low power and the bottom row is measurements with different bus waveguide power as shown in the legend. ©OSA publishing

With -7 dBm power in the bus waveguide, Figure 3.4e shows the resonance transmission for each ring radius. With a radius of over 600 μm, both of these rings have an intrinsic Q-factor of about 0.75 x 10^6, meaning that no bending loss is limiting the total loss. Each figure's bottom row depicts normalized transmission in a bus waveguide at various power levels ranging from -7 dBm to 4 dBm. At each resonance, the frequencies

are also matched to compare the relative transmission. Unlike the high-Q ring resonator transmission shown in Fig. 3.3a, these ring transmissions have a very similar profile at various power levels. Furthermore, since the transmission minimum is unaffected by the bus waveguide strength, the power-dependent Q-factor shift is minimal. There are three major explanations for this difference. First, this group of resonators does not have a Q-factor of 4 x 10^6, as stated in our previous work [18] since the condition of the etching equipment is not optimized in this process run. Second, the increased ring radius reduces the resonator finesse ($Finesse = \lambda \cdot Q_l/(2\pi R \cdot n_g)$), as well as the power build-up factor in the ring resonator. Third, the broad effective mode area of 0.91 µm^2 is achieved by the 1.8 µm wide, 56 nm deep etch depth waveguide. As a result of the combined effects of reduced power build-up and wide mode field, the intracavity power density is reduced. Even with same loaded Q-factor as the high-Q ring resonators measured in Fig. 3.3, this will reduce the intracavity power density by an order of magnitude.

Other than expanding the high-Q Si ring resonator to accommodate the high-power application, another solution in heterogeneously integrated tunable lasers is to use a material device that is free of nonlinear loss in the telecommunication wavelength range, for example, silicon nitride. The power based transmission properties of a fabricated Si_3N_4 high-Q cavity with a 1.6 mm ring radius were calculated here. Figure 3.5a depicts a cross section of the Si_3N_4 waveguide. The Si_3N_4 ring resonator's intrinsic Q-factor is 8.3 x 10^6, corresponding to a propagation loss of 3.3 dB/m (Fig. 3.5b). The effective mode area is around 10 µm^2 . Power-dependent transmission sweeps are measured in the same way as for extended Si rings, and the results are summarized in Fig. 3.5c. For each resonance wavelength, the wavelength is shifted and normalized. The normalized transmission almost has the same minima at all power levels. Even with a very high Q-factor, this calculation shows that the power-dependent loss in Si_3N_4 is negligible.

We can now summarize the power-dependent output for all of the resonators discussed

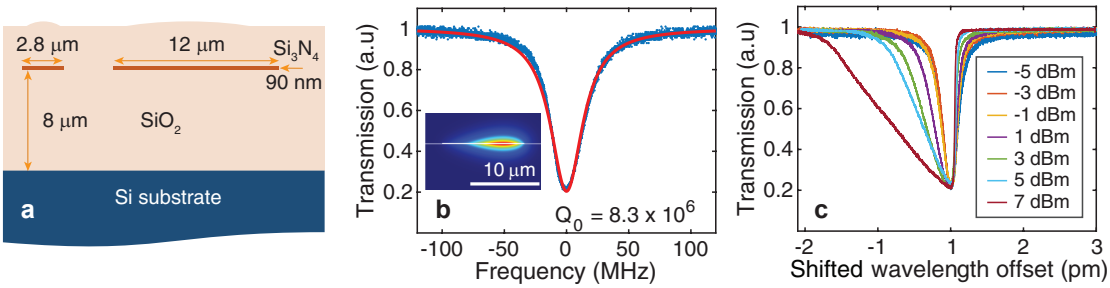

Figure 3.5: (a) Cross-sectional schematic view of Si_3N_4 ring resonator at the bus-ring coupling region. (b) Fitted TE0 mode resonance of Si_3N_4 ring resonator with 1.6 mm radius. (c) Normalized transmission at different bus waveguide power shown in the legend for Si_3N_4 ring resonator. ©OSA publishing

above using the Q-factor extraction method mentioned before. Because of nonlinear loss at high power intensity levels in the ring waveguide, the loss will be different from the loss in the bus waveguide. The derived loss in the ring can be determined from the ring resonator intrinsic Q-factor from $\alpha = 2\pi n_g/Q_0\lambda$, where n_g is the group index and λ is the resonance wavelength, without taking into account the spatial loss modulation along the ring circumference.

The power-dependent loss is summarized in Fig. 3.6. As the bus waveguide capacity reaches 0.5 mW (around 80 mW/m^2 power density in the ring resonator), a multimode Si ring with high Q-factor (2.4 x10^6 and 1.7 x 10^6) shows the lowest cold-cavity loss (0.3 and 0.4 dB/cm) among the Si resonators, but the extracted loss ramps up rapidly. When the bus waveguide power is about 2 and 3mW respectively, the loss becomes the highest (¿ 1 dB/cm). With $>$ 1 mW bus waveguide power, a similar radius but smaller cross-section quasi-single-mode ring resonator with $Q_{oc} = 1.1 \times 10^6$ shows strong dependency, and the slope is similar to the 1.7x10^6 multimode ring due to its smaller mode cross section, which results in similar power intensity despite the Q-factor difference. Because of the relaxed intracavity power density, the extended Si ring resonator is relatively power-independent, with a loss of about 0.9 dB/cm. And as predicted, the Si_3N_4 ring resonator has very

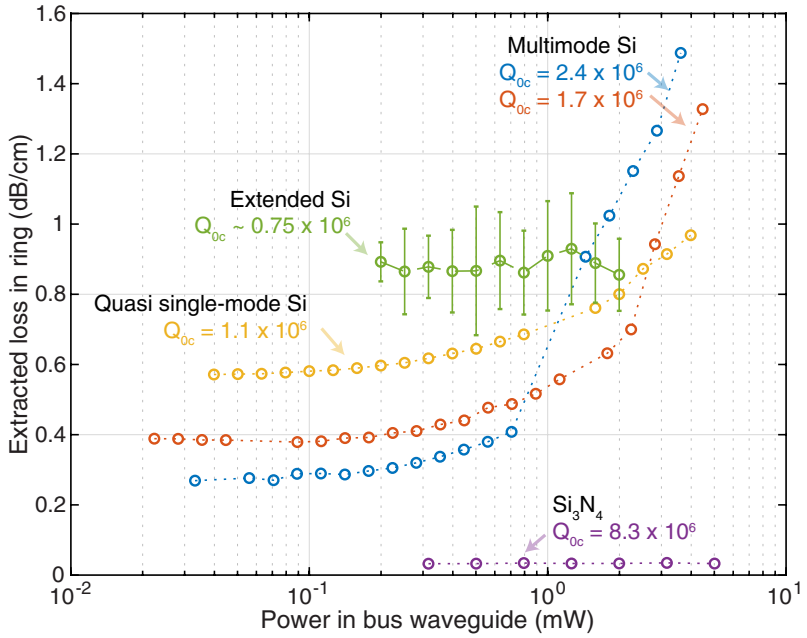

Figure 3.6: Dependence of extracted loss in ring for different type of ring resonators on the power in bus waveguide. The Si waveguides are all with 500-nm total thickness. The quasi-single mode Si waveguide is with a racetrack-type resonator and the waveguide is 1.07 µm. The multimode Si is 2.06 µm wide in a pulley type, while both have 100 µm radius and 231 nm etch depth. The extended Si waveguide is 1.8 µm wide with 56-nm deep etch depth. The ring radius is around 600 µm. The Si_3N_4 waveguide is 12 µm wide, 90 nm deep with 1.6 mm radius. ©OSA publishing

little nonlinear loss.

According to this analysis, the nonlinear loss becomes significant at sub-mW bus waveguide power (100 mW/m^2 power intensity in ring resonator) and dominates the total loss of the laser device with just a few mW in the bus waveguide for high-Q (¿ 1M) Si resonators with small ring radius (100 µm) and small cross section (0.4-0.7 µm^2). At higher power levels, it can rapidly scale up. As a result, they are incompatible with a high-performance narrow-linewidth laser, which is commonly used in this power range for a variety of applications. The output power will be limited due to the negative impact of nonlinear failure. In addition, since the linewidth scales with 1/P, the laser's linewidth output suffers at the same time. Furthermore, even with arbitrary high gain content,

the laser linewidth would not collapse in the end with this degree of power-dependent loss, and there would be a lower limit to the achievable linewidth due to nonlinear loss. Furthermore, nonlinear absorption can produce additional heat and increase the overall system's phase instability. Nonlinear self-pulsing and nonlinear hysteresis effects in a poorly engineered high-Q Si ring resonator will further degrade laser output at moderate power levels[19]. And, once again, increased Q-factor and smaller ring resonator physical size would exacerbate this negative impact (ring radius, ring waveguide cross section area, etc.). To avoid TPA-induced FCA, one potential solution is to use a reverse biased p-i-n diode in the Si waveguide[20]. This is commonly used in Si Raman lasers to enable the Si waveguide to handle over 10 times more power. Using the TM mode in Si resonators could help reduce the confinement factor and nonlinear absorption loss, but improving the TM mode Q-factor and lowering the linear loss requires fabrication optimization. Designing a high-Q ring resonator with reduced intracavity power density, such as extended Si ring resonator designs with large ring radius and large cross section, is a simpler process. This power based loss will be a more critical limiting factor in having a high power, narrow-linewidth butt-coupled Si laser due to the even smaller waveguide core size of 220 nm thick Si waveguides in a typical silicon photonics foundry. Beyond that, we expect ring-resonator based III-V/Si/Si_3N_4 widely tunable heterogeneously integrated lasers to achieve unparalleled laser efficiency due to the ultra-low loss of Si_3N_4 waveguides and their negligible nonlinear loss. One focus of this thesis is to integrate Si_3N_4 into the laser cavity to enable a narrow laser linewidth, and the next section is the first step towards this: a hybrid integrated ultra-narrow linewidth Si_3N_4 E-DBR laser.

3.3 Ultra-narrow linewidth E-DBR lasers

External cavity lasers are widely used as narrow linewidth laser sources in many applications. An extended Bragg grating with a narrow bandwidth and high side-lobe suppression is an excellent option among the various external cavity designs. The extended cavity's narrow mode spacing is offset by the extended Bragg grating's broader bandwidth, resulting in an Extended-Distributed Bragg Reflector (E-DBR) laser. With a Lorentzian linewidth down to 15 Hz and an output power of 100 mW, E-DBR lasers based on a fiber Bragg grating (FBG) external cavity have been demonstrated[21]. However, a high index and perturbation uniformity over a long FBG is difficult to achieve, and high-quality fabrication of custom grating designs is needed to produce these lasers. Due to the use of planar wafers, high-precision optical lithography, and standard waveguide etching methods, integrated on-chip waveguide Bragg gratings would be preferred for large-scale manufacturing if comparable Bragg grating performance could be achieved.

Here we use the developed low-κ Si_3N_4 Bragg grating as the external cavity to enable ultra-narrow linewidth hybrid integrated lasers[5]. Figure 3.7 shows the butt coupled semiconductor gain chip (reflective semiconductor amplifier (RSOA)) and Si_3N_4 grating chip. The laser output is taken from the other side of the Si_3N_4 grating through another angled facet Si_3N_4 inverse taper. The ultra-low κ Si_3N_4 Bragg grating design is similar to those discussed in Chapter 2. Identical Si_3N_4 grating posts are placed on one side of a Si_3N_4 waveguide with a period , separated from the Si_3N_4 waveguide by a designed gap width. The posts provide a weak perturbation of the loosely confined Si_3N_4 waveguide mode, and constructively build up the desired optical reflection at the Bragg wavelength (determined by $\lambda_{Bragg} = 2\Lambda \cdot n_{eff}$ where n_{eff} is the effective index). The waveguide is 90 nm thick and 2.8 µm wide. A Bragg wavelength of 1550 nm was selected, resulting in a period of 526 nm and a calculated effective index of 1.472. The grating fill factor is set

to 0.5, with a 263 nm grating post size. Both the waveguide and the grating posts are 90 nm thick.

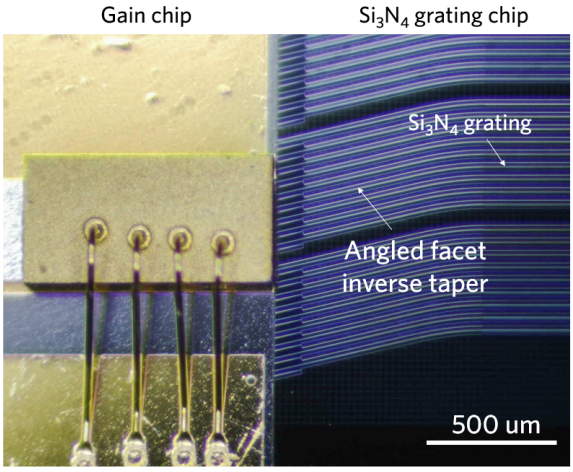

Figure 3.7: Optical image of the butt coupled semiconductor gain chip (RSOA) and Si_3N_4 grating chip. ©OSA publishing

By adjusting the gap width between the post and the Si_3N_4 waveguide core, the grating κ can be customized. It is desirable to provide an ultra-low κ extended grating with narrow grating reflection bandwidth for use as a narrow linewidth laser cavity, as the modified Schawlow-Townes theorem shows that the laser linewidth is proportional to the square of the passive cavity filter bandwidth as

$$\Delta\nu_{laser} \propto \frac{\Delta\nu_{cavity}}{P_{laser}} \tag{3.5}$$

where P_{laser} is the laser output power. κL_g, on the other hand, should be large enough for a fixed grating length L_g, since κL_g directly translates to the peak grating reflectivity since for weak reflection it holds:

$$|r_g| \approx \frac{tanh(\kappa L_g) \cdot sin(\delta L_g)}{\delta L_g} \tag{3.6}$$

where r_g is the grating reflectivity, $\delta \equiv \beta - \beta_0$ and β and β_0 are the average propaga-

tion constant and propagation constant at Bragg wavelength respectively. A sufficient reflectivity is needed because the mirror loss of a DBR laser is determined by it. When the overall gain equals the overall loss, lasing condition is fulfilled, and a low κL_g will prevent the lasing if the mirror loss were too high. We chose a grating length of 20 mm based on this study and fabrication choices, which suits in a single reticle mask of 248 nm deep ultraviolet (DUV) lithography stepper. The gap width ranges from 1589 to 945 nm, with κ ranging from 0.2 to 1 cm^{-1}.

The modified Schawlow-Townes linewidth ($\Delta\nu_0$) coupled to an external cavity (a Bragg grating with effective length defined by

$$L_{eff} = \frac{1}{2\kappa \cdot tanh(\kappa L_g)} \tag{3.7}$$

can be used to calculate the E-DBR laser linewidth. The external cavity will reduce the modified Schawlow-Townes linewidth of the active-cavity-only laser by a factor of

$$F^2 = (1 + A + B)^2 \tag{3.8}$$

where A and B include the effects of reduced reduced longitudinal mode confinement and detuned negative feedback on the laser linewidth [3]. As factor B is mainly depends on the phase, here we only consider the contributions from factor A that determines the cavity length and feedback design.

The factor A is defined by

$$A = \frac{n_{Si_3N_4} \cdot (L_{eff} + L_{taper})}{n_{gain} \cdot L_{gain}} \tag{3.9}$$

where L_{taper} is the inverse taper length (700 µm), L_{gain} is gain chip waveguide length (1 mm) and $n_{GC} = 3.8$ and $n_{Si_3N_4} = 1.57$ are the group indices of the gain chip and

Si_3N_4 waveguide (and also approximation for the short Si_3N_4 inverse taper) respectively. Additionally, the laser mirror loss α_m is also affected by the peak grating reflection

$$R_g = tanh^2(\kappa L_g) \tag{3.10}$$

and the coupling loss δ. We have

$$\langle \alpha_m \rangle = \frac{ln(\frac{1}{\sqrt{R_1 R_{eff}}})}{L_{gain}} \tag{3.11}$$

and due to the HR coating on the gain chip rear facet, $R_1 \sim 1$. The effective grating reflectivity is given by

$$R_{eff} = \delta^2 \cdot R_g e^{-2\alpha_{Si_3N_4} \cdot (L_{eff} + L_{taper})}. \tag{3.12}$$

By applying these into the modified Schawlow-Townes linewidth and related formulas

$$\Delta v_0 = \frac{(\Gamma v_g g_{th})^2 \eta_0}{4\pi P_0} n_{sp} h v \left(1 + \alpha_H^2\right) \tag{3.13}$$

$$P_0 = F_2 \frac{\eta_i \langle \alpha_m \rangle}{\langle \alpha_i \rangle + \langle \alpha_m \rangle} \frac{hv}{q} (I - I_{th}) \tag{3.14}$$

and

$$\eta_0 = \frac{\langle \alpha_m \rangle \cdot F_2}{\Gamma g_{th}} \tag{3.15}$$

we find

$$\Delta v = \frac{\Delta v_0}{(1+A)^2} \propto \frac{(\langle \alpha_i \rangle + \langle \alpha_m \rangle)^2}{(I - I_{th})(1+A)^2} \tag{3.16}$$

Since lasers are normally biased at many times the threshold current during operation,

we assume that all laser designs are pumped at the same $(I-I_{th})$ condition for comparison purposes. We thus define the figure of merit (FOM):

$$FOM \equiv \frac{\left(\langle\alpha_i\rangle + \langle\alpha_m\rangle\right)^2}{(1+A)^2} \tag{3.17}$$

For different κ designs of E-DBR lasers, the FOM enables optimization for the narrowest linewidth. The FOM for E-DBR lasers based on gratings ($L_g = 20$ mm) with different κ is plotted in Fig. 3.8. To achieve a narrow linewidth, it is necessary to have a low coupling loss. The narrowest linewidth is reached for κ values of 0.3 cm^{-1} to 0.4 cm^{-1}, which corresponds to an on-chip peak reflection range of 20% to 45 %, depending on the coupling loss. The reflectivity is still in the weak perturbation regime, and grating side lobe suppression is high, allowing for a high laser side-mode suppression ratio (SMSR). Another advantage of a lower grating reflectivity is that the laser slope efficiency and output power are increased.

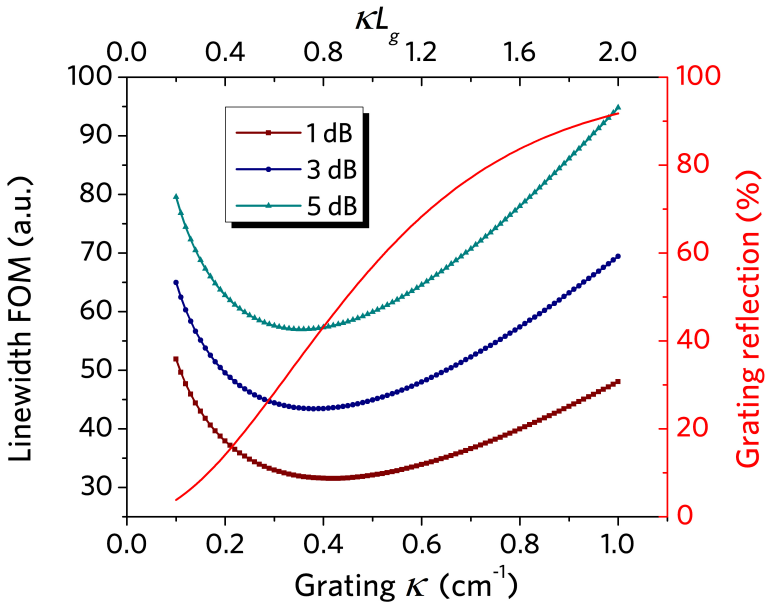

Figure 3.8: Calculated linewidth FOM and grating on-chip reflection dependence on grating κ values for $L_g = 20$ mm. ©OSA publishing

3.4 Hybrid integrated Si_3N_4 E-DBR lasers

Based on previous analysis, the device configuration of Figure 3.9a shows the passive grating measurement for a grating with a designed κ of 0.3 cm^{-1}. The on-chip grating power reflection is calculated to be around 20 % centered at 1544.17 nm by taking the grating's transmission response from the input to the output side. The reflection spectrum in Fig. 3.9b shows a single reflection peak with a 3-dB bandwidth of 4.5 GHz and around 12 dB close-in sidelobe suppression. Because of the high wavelength selectivity, stable single mode lasing with a narrow spectral linewidth is possible.

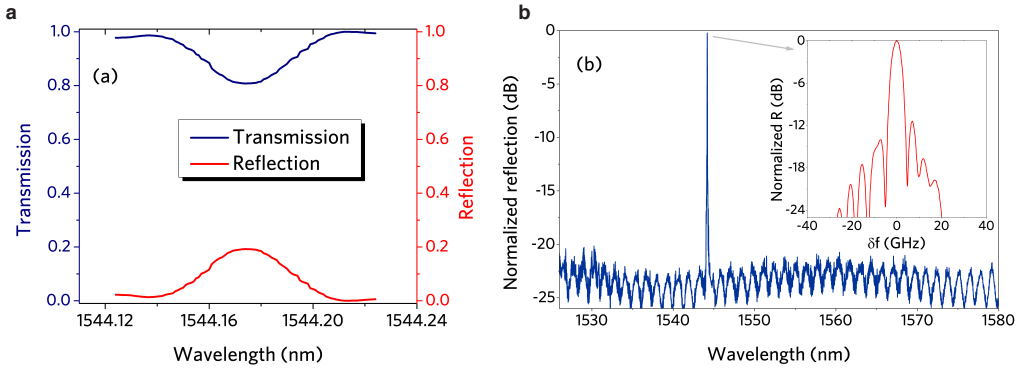

Figure 3.9: a. Normalized transmission and on chip reflection of a Si_3N_4 Bragg grating. b. Normalized reflection (inset shows close-in response). ©OSA publishing

Figure 3.10a depicts the measured Light-Current-Voltage (LIV) characteristic. With a combined on-chip power of 24 mW and a cleaved optical fiber coupled power of 12 mW, the threshold current is 92 mA. The relatively high threshold current is due to the high coupling loss between the gain and grating chips, which can be reduced or removed in a fully integrated structure, and this will also increase the maximum output power. External cavity mode hopping behavior between single mode and multimode lasing regions causes strong variations in output power versus pump current. When no grating-based mode for single-mode operation is available in multimode regions, lasing can even stop with zero output power. Tiny discontinuities in the IV curve result from

carrier density variations caused by these strong mode interactions, as seen in the map, suggesting strong laser feedback from the external Si_3N_4 grating cavity. Figure 3.10b shows the lasing spectrum; the lasing wavelength is 1544.17 nm, and the SMSR is over 55 dB.

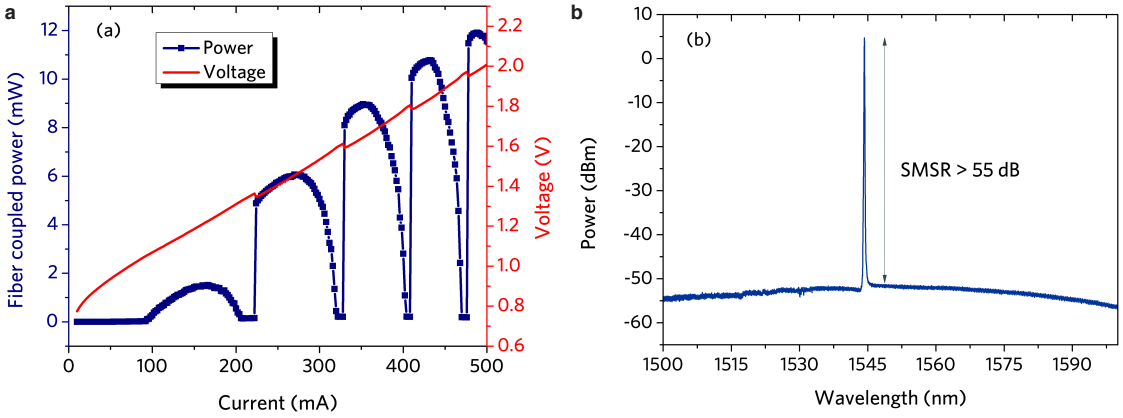

Figure 3.10: a. LIV measurements and b. lasing spectrum at 420 mA of an E-DBR laser with 0.3 cm^{-1} κ grating. ©OSA publishing

Despite the fact that the coupling loss between the semiconductor chip and the Si_3N_4 grating accounts for the majority of the cavity loss, the grating $_g$ also has an impact on the effective mirror loss and laser efficiency. Stronger κ increases grating reflection for the same length gratings, resulting in lower mirror loss and lasing threshold. The LIVs of lasers using the same gain chip but gratings with four different κ values can be seen in Fig.3.11a, which shows the LIVs of lasers using the same gain chip but gratings with four different κ values. Figure 3.11b depicts the relationship between threshold current and maximum fiber coupled power. The threshold current falls from 110 mA to 54 mA as κ increases from 0.2 cm^{-1} to 1 cm^{-1}, while the maximum power peaks for the grating with κ of 0.5 cm^{-1}. For applications requiring a high output power, the grating should be built to provide enough feedback (reflection) for a low threshold current, as well as minimal mirror loss to achieve a high lasing slope efficiency.

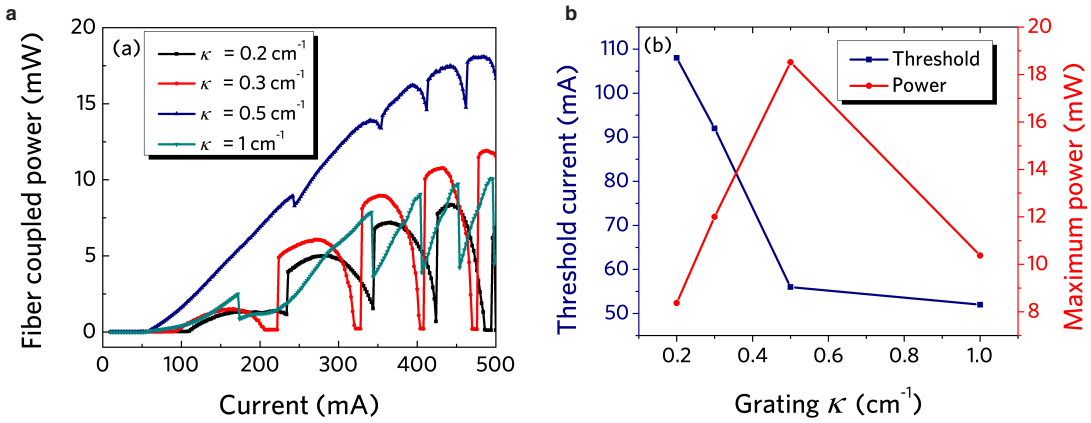

Figure 3.11: a. LIV measurements and b. dependence of threshold current and maximum fiber coupled power for gratings with various κ values. ©OSA publishing

We used an OEWaves phase noise measurement equipment to describe the laser frequency noise (OE4000). To avoid any feedback effect on the laser linewidth efficiency, optical isolators with isolation ¿ 60 dB were used after the laser output. Figure 3.12 shows frequency noise measurements for the Si_3N_4 E-DBR laser with a grating κ of 0.3 cm^{-1} from 1 kHz to 10 MHz. The bias current is 350 mA, which is near the top of a single-mode operation regime. The final flat section shows 100 Hz2/Hz frequency noise, corresponding a 320 Hz Lorentzian linewidth, making this sub-kHz laser ideal for LIDAR and advanced communication systems.

3.5 Summary

In summary, this chapter starts with introduction of narrow-linewidth developments, showing the trend and solution for a high-performance narrow-linewidth laser. Then the nonlinear loss in Si high-Q ring resonators which is one important limiting factor for narrow-linewidth III-V/Si tunable lasers is discussed. The conclusion is that Si_3N_4 which is low loss and free of nonlinear loss is advantageous for a narrow-linewidth laser. Then a hybrid-integrated Si_3N_4 E-DBR narrow-linewidth laser based on butt coupled

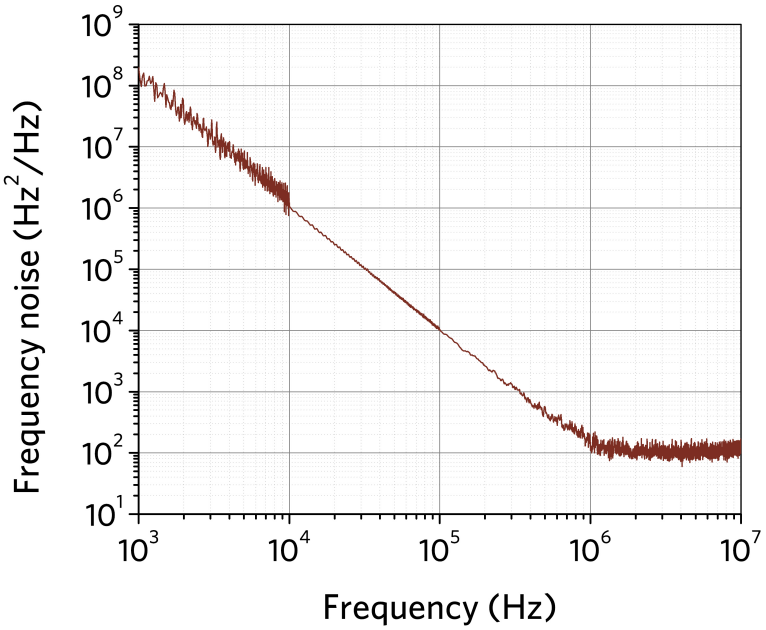

Figure 3.12: Frequency noise spectrum of an E-DBR laser with 20-mm long, $\kappa = 0.3cm^{-1}$ grating. ©OSA publishing

semiconductor gain chip and Si_3N_4 low κ grating is demonstrated, showing excellent linewidth performance and verifies the laser cavity design. This chapter also lays the theoretical design foundation for heterogeneously integrated lasers on Si_3N_4, which will be the focus for the following chapters.

References

[1] A. L. Schawlow and C. H. Townes, *Infrared and optical masers*, *Physical Review* **112** (1958), no. 6 1940.

[2] C. Henry, *Theory of the linewidth of semiconductor lasers*, *IEEE Journal of Quantum Electronics* **18** (1982), no. 2 259–264.

[3] R. Kazarinov and C. Henry, *The relation of line narrowing and chirp reduction resulting from the coupling of a semiconductor laser to passive resonator*, *IEEE Journal of quantum electronics* **23** (1987), no. 9 1401–1409.

[4] K. Vahala and A. Yariv, *Detuned loading in coupled cavity semiconductor lasers—effect on quantum noise and dynamics*, *Applied Physics Letters* **45** (1984), no. 5 501–503.

[5] C. Xiang, P. A. Morton, and J. E. Bowers, *Ultra-narrow linewidth laser based on a semiconductor gain chip and extended Si_3N_4 Bragg grating*, *Optics Letters* **44** (2019), no. 15 3825–3828.

[6] N. M. Kondratiev, V. E. Lobanov, A. V. Cherenkov, A. S. Voloshin, N. G. Pavlov, S. Koptyaev, and M. L. Gorodetsky, *Self-injection locking of a laser diode to a high-Q WGM microresonator*, *Optics Express* **25** (Nov., 2017) 28167–28178.

[7] G. Hadley, *Injection locking of diode lasers*, *IEEE journal of quantum electronics* **22** (1986), no. 3 419–426.

[8] N. G. Pavlov, S. Koptyaev, G. V. Lihachev, A. S. Voloshin, A. S. Gorodnitskiy, M. V. Ryabko, S. V. Polonsky, and M. L. Gorodetsky, *Narrow-linewidth lasing and soliton kerr microcombs with ordinary laser diodes*, *Nature Photonics* **12** (2018), no. 11 694–698.

[9] W. Liang, D. Eliyahu, V. S. Ilchenko, A. A. Savchenkov, A. B. Matsko, D. Seidel, and L. Maleki, *High spectral purity kerr frequency comb radio frequency photonic oscillator*, *Nature Communications* **6** (08, 2015) 7957.

[10] C. Xiang, W. Jin, J. Guo, C. Williams, A. M. Netherton, L. Chang, P. A. Morton, and J. E. Bowers, *Effects of nonlinear loss in high-Q Si ring resonators for*

narrow-linewidth III-V/Si heterogeneously integrated tunable lasers, *Optics Express* **28** (2020), no. 14 19926–19936.

[11] C. T. Santis, S. T. Steger, Y. Vilenchik, A. Vasilyev, and A. Yariv, *High-coherence semiconductor lasers based on integral high-q resonators in hybrid si/iii-v platforms*, *Proceedings of the National Academy of Sciences* **111** (2014), no. 8 2879–2884.

[12] M. A. Tran, D. Huang, and J. E. Bowers, *Tutorial on narrow linewidth tunable semiconductor lasers using si/iii-v heterogeneous integration*, *APL photonics* **4** (2019), no. 11 111101.

[13] J. Heebner, R. Grover, and T. Ibrahim, *Optical microresonator theory*. Springer, 2008.

[14] W. Bogaerts, P. De Heyn, T. Van Vaerenbergh, K. De Vos, S. Kumar Selvaraja, T. Claes, P. Dumon, P. Bienstman, D. Van Thourhout, and R. Baets, *Silicon microring resonators*, *Laser & Photonics Reviews* **6** (2012), no. 1 47–73.

[15] Q. Lin, O. J. Painter, and G. P. Agrawal, *Nonlinear optical phenomena in silicon waveguides: modeling and applications*, *Optics Express* **15** (2007), no. 25 16604–16644.

[16] M. Borselli, T. J. Johnson, and O. Painter, *Beyond the rayleigh scattering limit in high-q silicon microdisks: theory and experiment*, *Optics Express* **13** (2005), no. 5 1515–1530.

[17] H. Rong, A. Liu, R. Nicolaescu, M. Paniccia, O. Cohen, and D. Hak, *Raman gain and nonlinear optical absorption measurements in a low-loss silicon waveguide*, *Applied physics letters* **85** (2004), no. 12 2196–2198.

[18] M. A. Tran, D. Huang, T. Komljenovic, J. Peters, A. Malik, and J. E. Bowers, *Ultra-low-loss silicon waveguides for heterogeneously integrated silicon/iii-v photonics*, *Applied Sciences* **8** (2018), no. 7 1139.

[19] T. J. Johnson, M. Borselli, and O. Painter, *Self-induced optical modulation of the transmission through a high-q silicon microdisk resonator*, *Optics Express* **14** (2006), no. 2 817–831.

[20] H. Rong, R. Jones, A. Liu, O. Cohen, D. Hak, A. Fang, and M. Paniccia, *A continuous-wave raman silicon laser*, *Nature* **433** (2005), no. 7027 725–728.

[21] P. A. Morton and M. J. Morton, *High-power, ultra-low noise hybrid lasers for microwave photonics and optical sensing*, *J. Lightwave Technol.* **36** (Nov, 2018) 5048–5057.

Chapter 4

Heterogeneously integrated laser on silicon nitride

As a complementary metal–oxide–semiconductor (CMOS) material, silicon nitride (Si_3N_4) is widely used in modern integrated circuit (IC) technology[1]. Silicon nitride (Si_3N_4) has made rapid progress in photonics over the last decade, with breakthroughs in nonlinear photonics, optical sensing, and other fields. The lack of a high-performance integrated laser, however, prevents large-scale incorporation of Si_3N_4 waveguides into complex photonic integrated circuits (PICs). One important aspect of this thesis is to show how a novel III-V/Si/Si_3N_4 structure allows for efficient electrically pumped lasing in a Si_3N_4-based laser external cavity. As opposed to lasers that are solely based on semiconductors, the laser has much better temperature stability and lower phase noise. Furthermore, the demonstrated multilayer heterogeneous integration paves the way for incorporating efficient optical gain with a variety of low-refractive-index materials.

This chapter will cover the developments of heterogeneously integrated lasers on silicon nitride. First part will include the developments of multilayer heterogeneous integration that is a key enabler for the integration of silicon nitride waveguide with III-V

gain materials. Second part discussed the first demonstration of heterogeneous integrated Si_3N_4 laser with a Si_3N_4 Spiral grating. Third part of this chapter discussed the developments of high-performance Si_3N_4 E-DBR lasers with high output power and narrow linewidth. These lasers, together with ultra-high-Q Si_3N_4 ring resonators, also enable Hertz-level narrow linewidth semiconductor lasers.

4.1 Multilayer heterogeneous integration

Heterogeneous integration combines the advantages of various material classes that aren't naturally "compatible" in order to provide photonic devices with greater functionality. Since the advent of heterogeneous III-V integration with silicon to make effective lasers, the silicon photonics industry has seen rapid advancements[2]. For optical interconnects, high-capacity III-V/Si based silicon photonic transceiver chips with seamless integration of lasers and silicon photonic circuits have been commercialized, with millions of devices shipped annually[3]. Existing Si_3N_4 technology has resulted in the development of a full range of passive devices and the next breakthrough will necessitate the inclusion of an on-chip laser, while active applications up to now still rely on off-chip laser sources. Hybrid butt coupling of a III-V gain chip to a Si_3N_4 external cavity has been used to include Si_3N_4 into the laser cavity, as discussed in Chapter 3 [4]. In comparison to a butt-coupled laser, heterogeneous integration of Si_3N_4 into the laser cavity eliminates the time-consuming and costly optical alignment and packaging of separate chips. Additionally, butt coupling also causes much higher coupling loss and parasitic reflection, both of which will degrade the laser efficiency.

Compound waveguide coupling is used in a heterogeneously integrated laser through the hybrid evanescent mode within the heterogeneous layers or via efficient mode transitions between the compound waveguiding layers. The III-V epitaxial layer in current

mature heterogeneous integrated lasers operating at 1550 nm has a thickness around 2 µm and a slab mode refractive index of 3.2, while Si_3N_4 has a refractive index of 2. Within a III-V/Si_3N_4 structure, even extreme tapering of the thick III-V epitaxial layer is unable to enable efficient mode coupling between them. To address this, we propose a III-V/Si/Si_3N_4 laser structure with multilayer heterogeneous integration and multiple mode transitions, starting with a gain section III-V/Si hybrid waveguide, transitioning to a Si waveguide, and then to the Si_3N_4 waveguide through a Si/Si_3N_4 transition. The Si_3N_4 passive layer is deposited and processed first, as shown in Fig. 4.1a, while the Si layer and subsequent III-V epitaxial layer are transferred on top of the Si_3N_4 waveguides through wafer bonding and processed later. A lower thermal oxide cladding and an upper cladding of deposited spacer oxide, as well as a Through oxide layer for laser passivation, make up the necessary silicon dioxide (SiO_2) cladding for a low loss Si_3N_4 waveguide. It should be noted that the mature 'SMART CUT' method for fabricating silicon-on-insulator (SOI) wafers could be used to fabricate Si-on-Si_3N_4 wafers in the future[5].

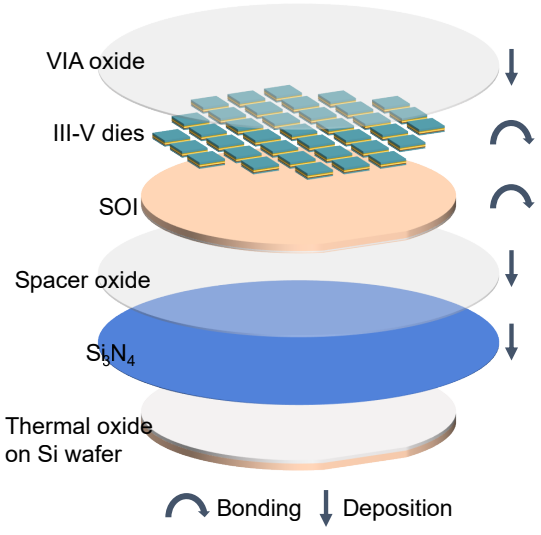

Figure 4.1: Schematic illustration of the multilayer heterogeneous integration process for laser integration with silicon nitride. ©OSA publishing

The use of III-V/Si/Si_3N_4 multilayer structure as shown in Fig. 4.2a will enable a good index match between the 2-µm-thick InP stack and 500-nm-thick Si layer (Fig. 4.2b) as the Si slab mode index at 500 nm thickness exceeds that of a InP slab. So a Si waveguide can match the InP mode index and result in a hybrid InP/Si mode for efficient mode transition between InP and Si. However, the index match between the 500-nm-thick Si layer and 90-nm thick Si_3N_4 layer is still challenging. Figure 4.2c shows that this matching requires a Si waveguide width below 150 nm. For 500-nm thickness, this will impose significant difficulties as the narrow waveguide taper tip aspect ratio (height to width) is too high for precise dimension control in the waveguide etch.

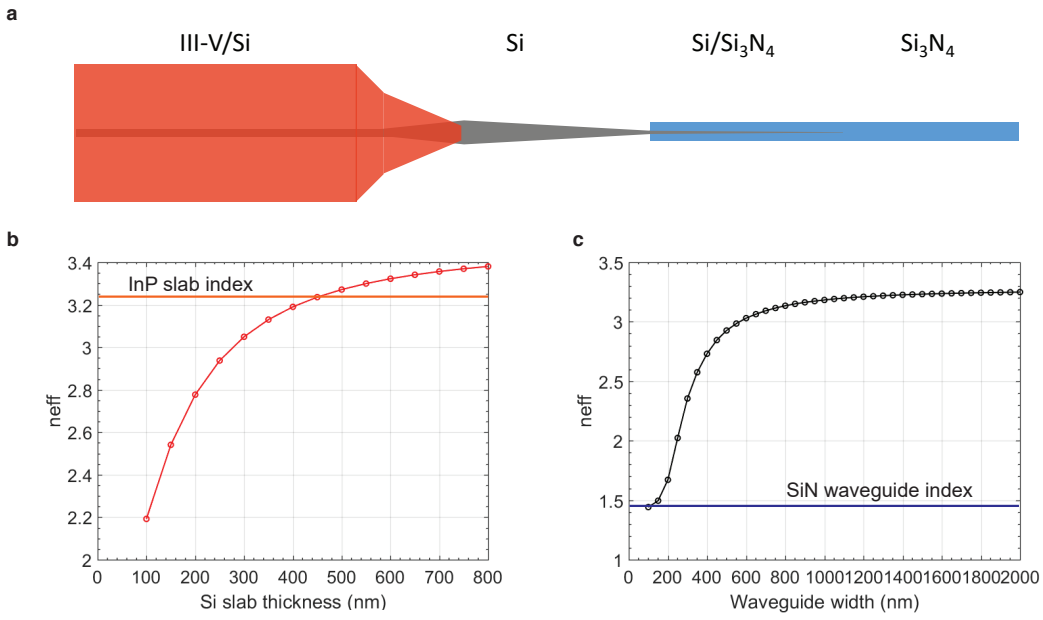

Figure 4.2: Schematic illustration of a III-V/Si/Si_3N_4 structure with fully etched Si layer and the calculated modal index versus waveguide dimensions.

To overcome this issue, we choose to use shallow-etched Si waveguides for the InP/Si hybrid section and use a dual-level Si taper to transit optical mode from shallow-etched Si rib waveguide to thin-core Si waveguide before transitioning to underneath Si_3N_4 waveguide. This structure is shown in Fig. 4.3a. The calculated modal index and

overlap in Fig. 4.3b illustrate that a narrow Si width (below 200 nm) is required to provide > 80% mode overlap between the Si/Si_3N_4 hybrid mode and Si_3N_4 waveguide mode. Figure 4.3c plots the simulated cross-sectional fundamental TE mode electrical field distribution at different taper section labeled by color contour: red, Si-Si_3N_4 taper Si_3N_4 end; green, Si-Si_3N_4 taper Si start; orange, thick Si to thin Si taper end; blue, thick Si to thin Si taper start.

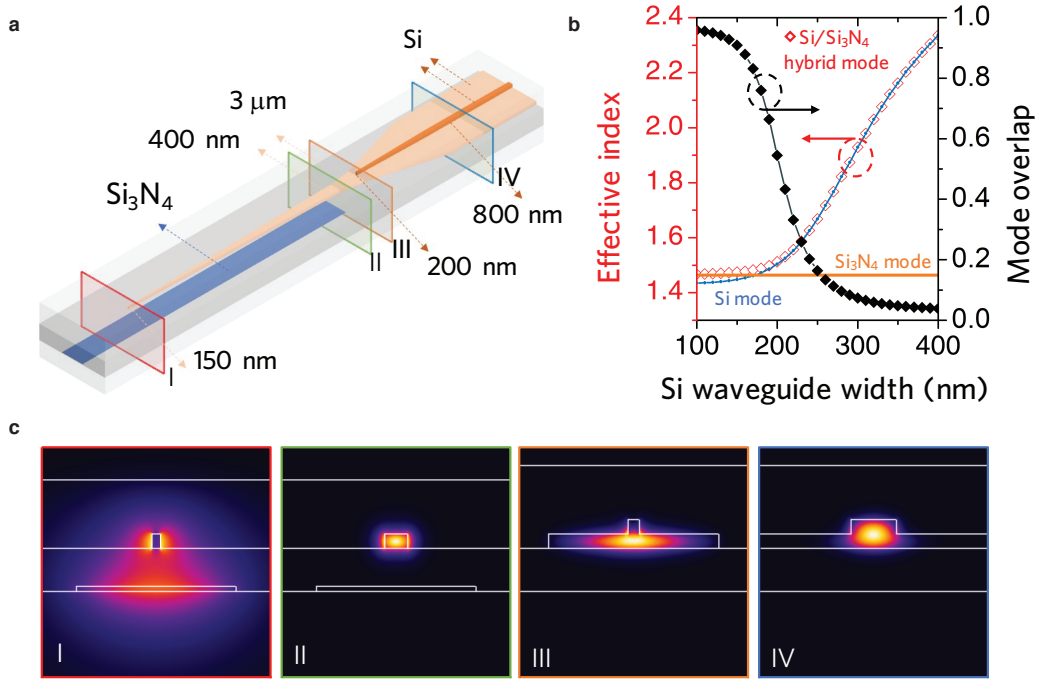

Figure 4.3: a. Schematic illustration of a dual-level Si-Si_3N_4 taper. b. Calculated modal index and mode overlap between the thin-core 269-nm-thick Si waveguide mode and thin-core 269-nm-thick, 2.8-μm-wide Si_3N_4 waveguide mode. c. Simulated mode distribution plot for different locations at the Si-Si_3N_4 taper as shown in a. ©OSA publishing

The taper transmission efficiency is simulated by 3D-FDTD (finite-difference time-domain) method and the result is in Fig. 4.4. As used in our laser, a 269 nm thick Si layer is tapered from 400 nm to 150 nm while the Si_3N_4 waveguide is 2.8 μm wide along the taper. The spacer oxide in between the Si and Si_3N_4 layer is 660 nm thick. The

power transmission of fundamental TE mode in the Si waveguide to the fundamental mode TE mode in the Si_3N_4 waveguide is over 90%, validating the adiabatic design to achieve a high mode overlap between the fundamental TE hybrid Si/Si_3N_4 mode and the fundamental TE Si_3N_4 mode. In general, a narrower taper tip is preferred. As can be seen from Fig. 4.41, 100 nm taper tip provides near unity mode transmission while a 200 nm tip will result in about 3 dB single trip loss in the taper.

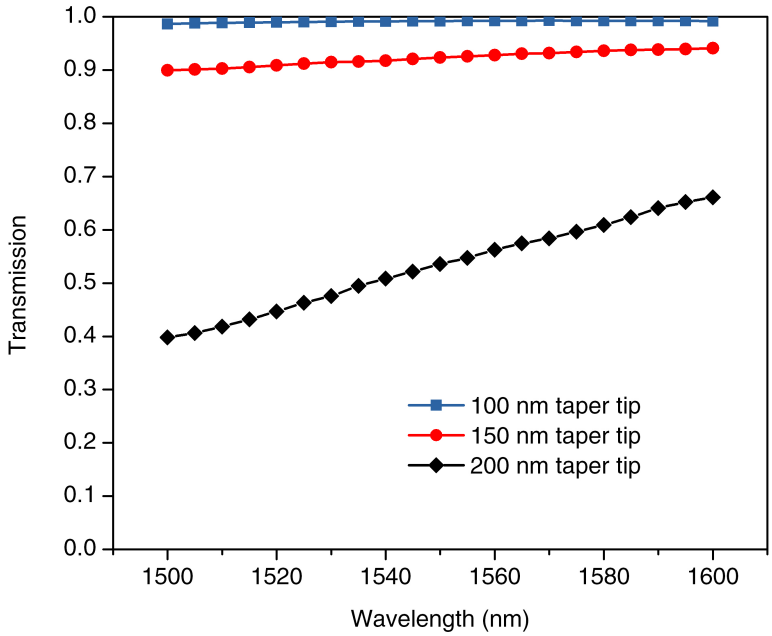

Figure 4.4: 3D-FDTD simulation of the fundamental TE mode transmission efficiency of Si-Si_3N_4 taper with different Si taper tip width.

The multilayer structure is thus based on the III-V/Si and Si/Si_3N_4 bonding and transition. This is illustrated in Fig. 4.5. The process starts with Si_3N_4 processing to create Si_3N_4 waveguides including Si_3N_4 laser cavities. After SiO_2 upper cladding deposition and polarization, the SOI is bonded on top of the Si_3N_4 wafer. Si substrate and BOX is removed to create a Si-on-Si_3N_4 wafer. Si process follows and InP epi is then bonded with its substrate removed. InP processing including InP mesa etch and laser passivisation, metallization complete the device fabrication. More details on the device

fabrication can be found in the appendix.

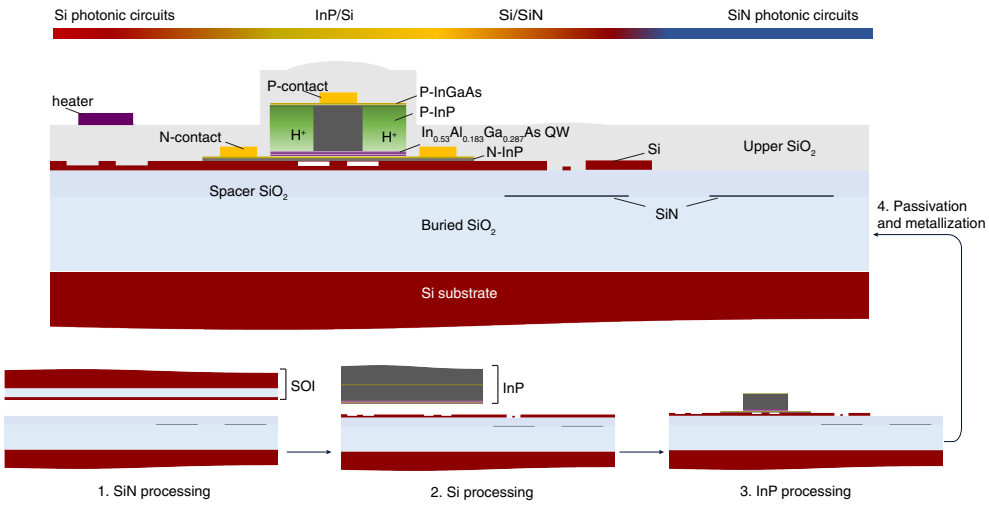

Figure 4.5: General process sequence and the cross section illustration of III-V/Si/Si_3N_4 multilayer structure before vias opening and probe deposition.

It has to be noted, this multilayer structure not only provides optical gain to Si_3N_4 photonic circuits, but also combines Si photonic circuits with Si_3N_4 photonic circuits in a way that both merits can be optimized and combined for advanced photonic devices. For example, the mature toolbox from Si photonics including modulation and photodetection can be used to enrich the functionalities of Si_3N_4 photonic circuits, which are also missing on a stand-alone Si_3N_4 platform.

Equipped with a highly-efficient Si-Si_3N_4 taper, the optimization of the III-V/Si/Si_3N_4 laser can be done on the optimization of Si_3N_4 cavity and III-V/Si gain respectively. There has been a lot of work done in Bowers group for the optimization of higher laser gain and also lower active loss. The current commonly used InP laser epi is a 3-QW $In_{0.53}Al_{0.183}Ga_{0.287}As$ epi. Its has total thickness of around 2.1 µm. P-InGaAs and N-InP layers serve as the metal contact layer with high doping levels. The P-InGaAs layer is also the etching stop layer for InP substrate removal. This epi has abrupt SCH structure

and more work can be done in optimizing the SCH structure for efficient carrier injection and improving the laser output power. More details on the iterations of InP epi stack can be found in Dr. Michael L. Davenport thesis[6].

4.2 III-V/Si/Si_3N_4 laser based on Si_3N_4 spiral grating

The first demonstrated III-V/Si/Si_3N_4 laser is based on a Si_3N_4 Bragg spiral grating[**?**]. Figure 4.6a plots laser schematics. On the two ends, a narrow-band Si_3N_4 spiral shaped distributed Bragg grating reflector (DBR) and a broadband tunable Si loop mirror form the laser mirrors, while a 1.5-mm long hybrid segment with indium phosphide dependent multiple quantum well (InP MQW) on Si provides the optical gain. The spiral DBR length is 20 mm and is formed by circular Si_3N_4 posts mounted along the curved waveguide (Fig. 4.6b) in a footprint of just 3.5 mm x 3.6 mm using a low loss Si_3N_4 waveguide (2.8 m wide and 90 nm thick). The grating period is 526 nm, indicating a reflection peak near 1550 nm. To keep the grating unchirped as the spiral waveguide radius decreases, the distance between the grating post and waveguide is increased from 920 nm to 944 nm along the spiral. As a low-reflection waveguide radiation terminator, another waveguide spiral with a radius of 100 µm to 40 µm is used. This terminator could be replaced by a spiral waveguide with opposite curvature in a larger spiral configuration to form a laser output for light passing through the grating. The Si_3N_4 spiral grating radiation during lasing is seen in the inset image taken with an infrared (IR) camera. SEM images in Fig. 4.7 show the cross section of InP/Si and Si/Si_3N_4 hybrid region and top view of InP/Si taper.

The continuous-wave (CW) light–current–voltage (LIV) characteristics of the III-

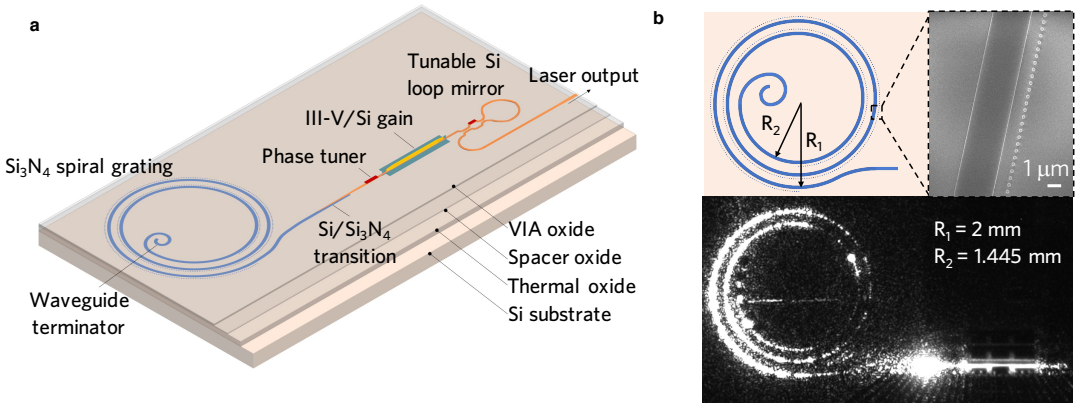

Figure 4.6: a. Schematics design of the III-V/Si/Si_3N_4 laser based on a Si_3N_4 Spiral Bragg grating. b. Infrared camera showing the laser operation and lasing in the Si_3N_4 spiral grating. ©OSA publishing

V/Si/Si_3N_4 laser at a 20 °C temperature are shown in Fig. 4.8. For 320 mA gain current, the lasing threshold is 75 mA with a peak on-chip output power of over 0.5 mW. Around 2.5 Ω of differential resistance. A wavemeter is used to record the lasing peak wavelength during the LIV sweep. As the gain current rises, multiple discontinuities appear in the output power and peak wavelength, indicating a 'cycled' mode hop. As the gain section temperature rises, the thermal response time of longitudinal modes and the grating reflection peak vary, resulting in shifted longitudinal mode number [7]. In our laser, this abrupt wavelength shift reflects the longitudinal mode spacing, which is around 0.025 nm.

The multiple mode hop area shown in Fig. 4.8 is an indication of the large temperature increase of the laser gain area due to the injected current heating. Although the laser resistance is low due to the excellent P- and N- contact (on the order of 5×10^{-6} Ω·cm^2), the thick SiO_2 undercladding limits the thermal dissipation and results in multiple mode hop cycles in the ∼ 300 mA injection current ramp. Currently, the undercladding thickness is 8 µm, which can be potentially reduced to around 5 µm in the future. Another potential solution is to implement thermal shunts designs[8]. Before the probe metal

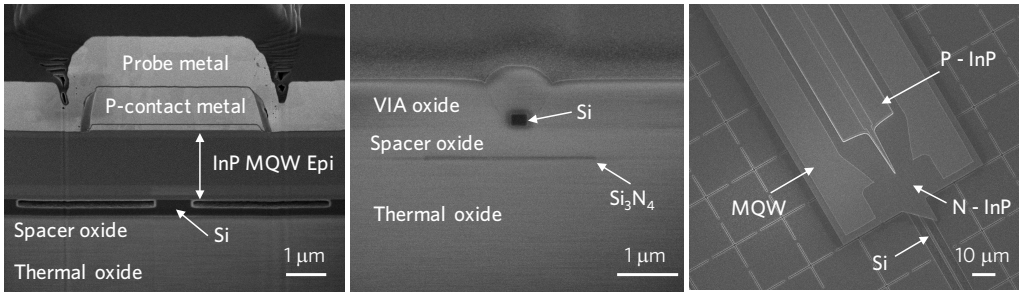

Figure 4.7: SEM image of fabricated laser; cross-sectional view at InP/Si (left), Si/Si_3N_4 (middle) section and tilted top view of InP-Si taper after N-InP mesa formation (right). ©OSA publishing

deposition, the passivated laser structures need to be go though another etch steps such it can creates void trenches down to the Si substrates. Si has a much higher thermal conductance ($\sim 130\ W/m \cdot K$ at 20^oC) than SiO_2 ($\sim 1.38 W/m \cdot K$ at 20^oC). With better thermal dissipation the mode hop phenomenon can be much relaxed.

When the gain current is increased from 232 mA to 249 mA, Figure 4.9b plots four mode states within a continuous wavelength change cycle corresponding to Fig. 4.9a. Since the multimode has less modal gain than the single mode, the wavelength red changes and the power decreases. The in-cavity optical process is largely responsible for mode hop activity and power fluctuation. With phase tuning, the power and peak wavelength display high hysteresis at 190 mA gain current (Fig. 4.9c). The laser appears to continue in single-mode operation and maintain relatively high power for longer as the temperature drops. The Si_3N_4 spiral grating produces a narrow band filter with a sidelobe extinction ratio of over 20 dB. The high lasing side mode suppression ratio (SMSR) of over 58 dB is due to the excellent sidelobe extinction ratio (Fig. 4.10).

Since both InP and InP/Si lasers have high thermo-optic coefficients, they are usually temperature sensitive. The thermo-optic coefficients (dn/dT) of Si_3N_4 and SiO_2 at 1550 nm are around $2.45 \times 10^{-5} K^{-1}$ and $9.5 \times 10^{-5} K^{-1}$, respectively. This is an order of

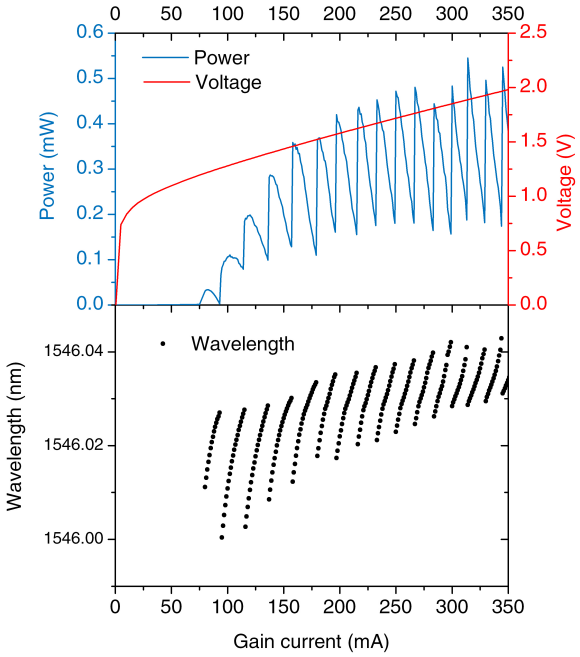

Figure 4.8: LIV characteristics and corresponding peak lasing wavelength. ©OSA publishing

magnitude less than Si ($dn/dT = 1.8 \times 10^{-4}K^{-1}$) or InP ($dn/dT = 2 \times 10^{-4}K^{-1}$). As a result, a Si_3N_4 waveguide DBR laser cavity would be much less vulnerable to temperature fluctuations than a Si or InP laser cavity. The results are shown in Fig. 4.11, which compare our laser to an extended-DBR InP/Si laser with a 15 mm long Si Bragg grating. The wavelength shift of the InP/Si/Si_3N_4 laser is just 0.47 nm (10.46 pm/^{o}C) when the temperature is changed from 10 to 55 ^{o}C, while the wavelength shift of the InP/Si laser is 3.3 nm (73.18 pm/^{o}C), a 7x difference.

Our laser's frequency noise was measured here (Fig. 4.12). It provides 0.3 power reflectivity with no tuning of the Si loop mirror. The lowest white-noise-limited frequency noise level obtained is about 2000 Hz^2/Hz, corresponding to a Lorentzian linewidth of 6 kHz. This is further reduced to 1300 Hz^2/Hz and 4 kHz, respectively, by increasing the photon density in the laser cavity by tuning the Si loop mirror reflectivity to optimum.

We also found a detuned loading effect in our laser, where the minimum linewidth is

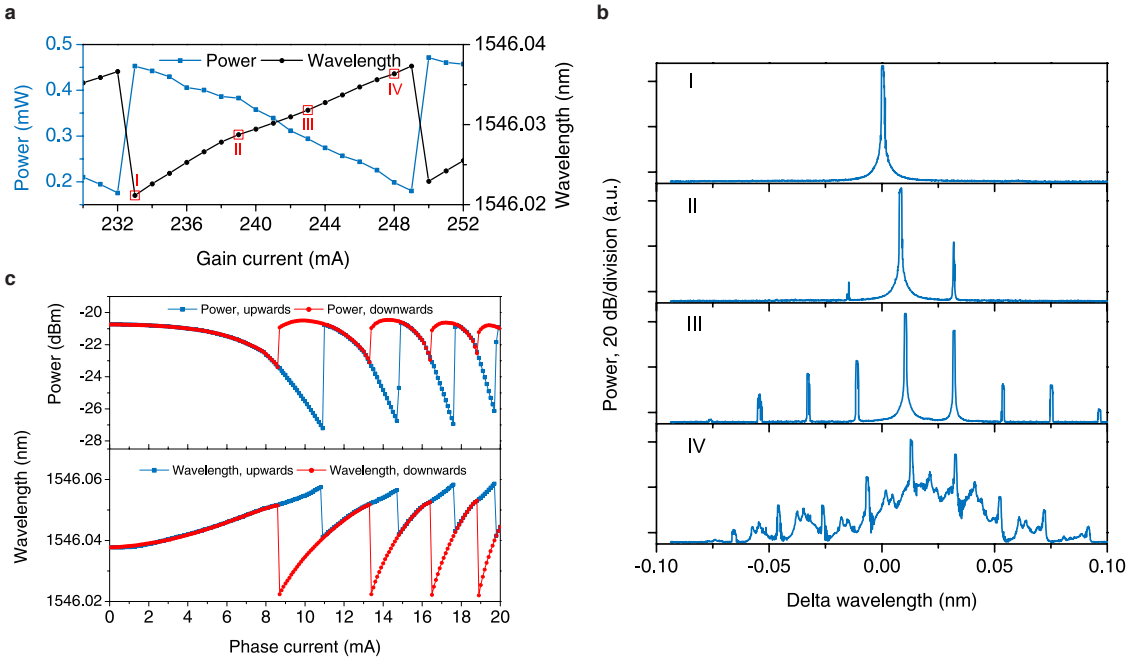

Figure 4.9: Close-in lasing spectrum at different bias currents as labeled in the top plot, showing (I) stable single-longitudinal mode, (II, III) stable multi-longitudinal mode and (IV) chaotic multi-longitudinal mode state. ©OSA publishing

reached when the longitudinal mode is slightly red shifted to the spiral grating reflection peak. Other than output power and peak wavelength variation due to mode hop, the laser exhibits 'cycled' frequency noise (FN) behavior while it is working across different mode states[9]. We investigated this phenomenon by taking the frequency noise spectral density (S_f) at different in-cavity phase conditions. We bias the laser at 190 mA and apply varying phase current on the thermo-optic phase tuner. When the phase current increases from 10.4 mA to 14.3 mA, we observed a complete cycle in terms of power variation and center frequency shift. The center frequency shift and white noise limited frequency noise level are shown in Fig. 4.13a. We plot S_f and corresponding optical spectra at four different phase currents in Fig. 4.13b,c. 10.4 mA marks the start of the first observed cycle, with Sf of $11.7 \times 10^3 Hz^2/Hz$. As the phase current increases to 12.3 mA, Sf reaches its local minimum of $2.7 \times 10^3 Hz^2/Hz$. The further increase

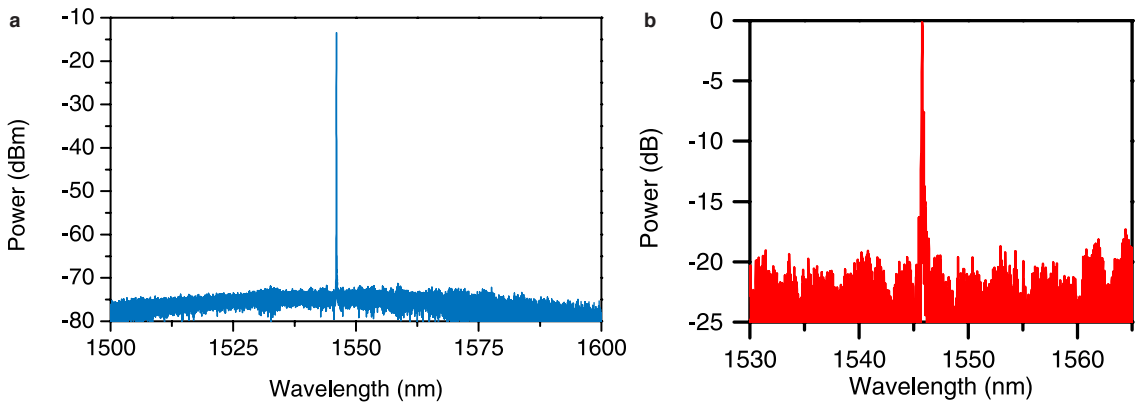

Figure 4.10: a. Optical spectrum at single mode operation. b. Passive grating reflection of the spiral Bragg grating.

of phase current leads the laser into multi-longitudinal mode state. After an abrupt increase in frequency noise, Sf decreases to the minimum multi-mode FN state with $S_f = 6.7 \times 10^3 Hz^2/Hz$ at 14.2 mA phase current. The second cycle starts at 14.3 mA phase current, evidenced by the blue shifted frequency and single-longitudinal mode spectrum. S_f is $9.1 \times 10^3 Hz^2/Hz$, close to Sf at the first cycle start. From Fig. 4.13c we

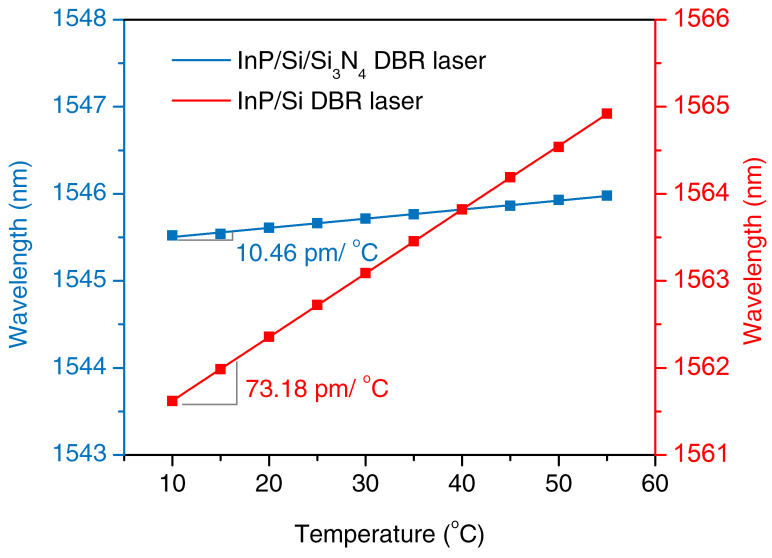

Figure 4.11: Lasing wavelength dependence on stage temperature. Blue, InP/Si/Si_3N_4 laser at around 250 mA gain current at single mode state; Red, InP/Si DBR laser at around 230 mA gain current at single mode state. ©OSA publishing

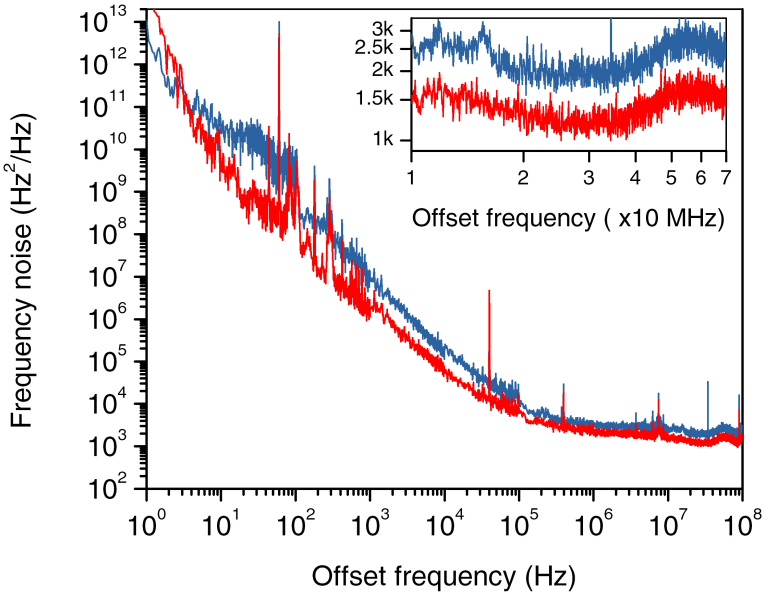

Figure 4.12: Laser frequency noise. Blue, 300.4 mA gain current and zero tuning on Si loop mirror; Red, 320 mA gain current and 10 mA Si loop mirror bias current. Inset shows zoom-in look of white-noise-limited frequency noise level. ©OSA publishing

can see the low FN single-mode state comes with a slightly increased sidemode, which is evidence of the detuned loading effect[10]. This proves that a slightly red shifted longitudinal mode benefiting from negative optical feedback will have the lowest phase noise.

As the first demonstration of heterogeneously integrated laser with Si_3N_4 cavity, this laser proves the feasibility of integrate Si_3N_4 with III-V through multilayer heterogeneous integration. The spiral grating can be replaced by other Si_3N_4 feedback cavity as discussed in Chapter 2. With further reduced loss this approach will enable lasers with a longer Si_3N_4 spiral grating and weaker coupling constant κ, or cascaded ring resonators, to significantly reduce the laser linewidth and increase the output power.

Low phase noise combined with excellent temperature stability will result in lasers that are perfect for applications requiring highly stable lasers for optical references or sensing. This laser's high temperature stability should allow it to be used in high-

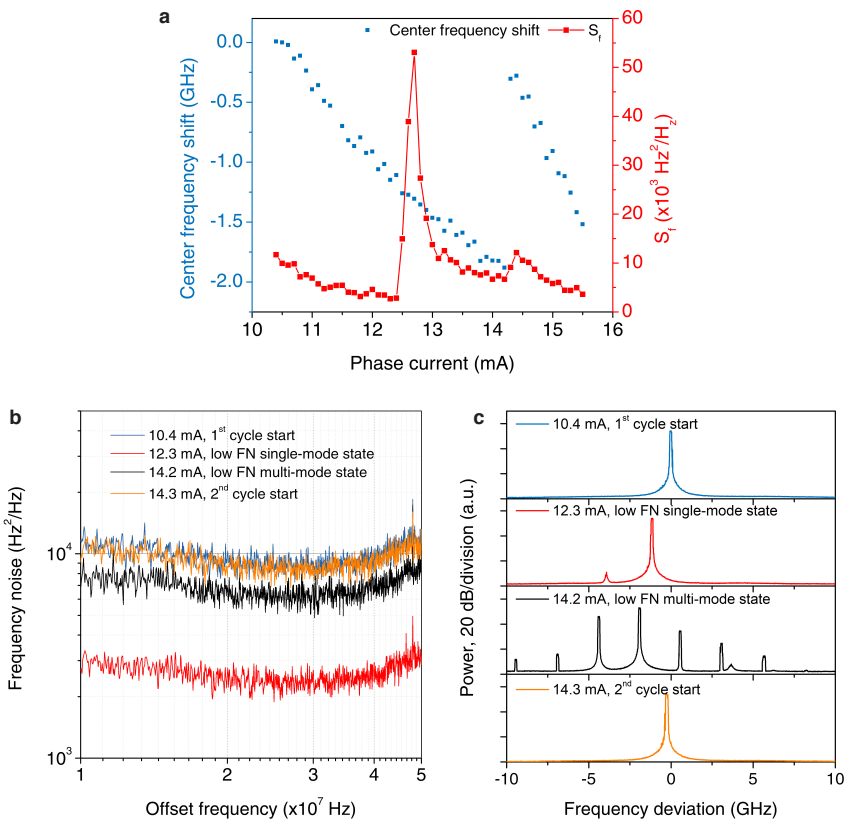

Figure 4.13: a. Laser center frequency shift and white noise limited frequency noise level dependence on phase tuning. b. frequency noise spectral density plot. c. optical spectrum at four different phase current conditions across a full cycle. ©OSA publishing

temperature environments. Our approach will also allow a whole new class of devices that need low loss waveguides but are currently not integrated, such as optical gyroscopes [11], ultra-narrow-linewidth Brillouin lasers, and frequency comb generators, which require off-chip pump lasers currently. The successful demonstration of multilayer heterogeneous integration is an important move toward fully utilizing the capabilities of wafer bonding technology, which can combine various material features for potential multi-functional PICs.

4.3 High-performance lasers for fully integrated Si_3N_4 photonics

The development of first heterogeneous III-V/Si/Si_3N_4 laser is a key step towards fully integrating Si_3N_4 with lasers and other functional photonic devices. However, the power is quite low due to the large taper loss, non-optimized Si_3N_4 grating cavity. High-power, low-noise semiconductor lasers are of critical importance in many applications including coherent communications, LIDAR and remote sensing[9]. In addition, in non-linear photonics where Si_3N_4 is playing a central role in recent progress of chip-scale optical frequency comb generation, a high optical output power is essential for frequency comb and soliton generation. In this section using multilayer heterogeneous integration, we demonstrate high-power (¿10 mW), low-noise (1 kHz fundamental linewidth), and -150 dBc/Hz RIN (relative intensity noise) lasers. These lasers produce Hertz-level fundamental linewidth on-chip lasers and can also directly generate optical frequency combs when used in a proven integration scheme with ultra-high-Q Si_3N_4 microresonators[12].

Our laser has the following main parts, as shown in Fig. 4.14: Si_3N_4 Bragg grating, InP/Si gain, Si reflector, and phase tuner. The Si_3N_4 grating is a low-κ side post grating that is generated by putting Si_3N_4 posts on both sides of the Si_3N_4 waveguide center. The distance between the center and the posts is always the same width and can be customized to achieve the desired κ value. The gratings use the maximum available 20 mm in length to fit the laser inside a deep ultra-violet (DUV) stepper mask reticle. It has an extended-distributed Bragg reflector, in order to achieve a long cavity length with high singlemode selectivity (E-DBR). A hybrid InP/Si active waveguide with mode transition tapers to the underneath Si waveguide is used in the InP/Si gain portion. Previous work [13] describes this form of hybrid segment in detail. In various laser designs, the gain section lengths are 2.5 mm or 1.5 mm. In this hybrid InP/Si waveguide

portion, the Si waveguide is shallow etched with a 231 nm etch depth to accommodate a single transverse-electric (TE) mode. Proton implantation is used to define the electrical current channels for efficient carrier injection after the creation of the large InP mesa and laser passivation.

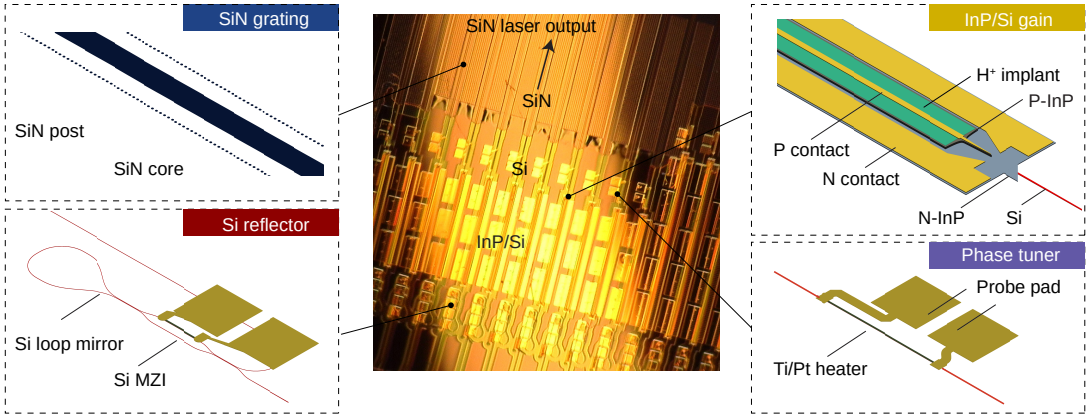

Figure 4.14: A device optical photograph showing InP/Si/Si_3N_4 DBR laser arrays. The lasers consist of four sections including the Si_3N_4 grating, InP/Si gain section, Si reflector and phase tuner, with each schematic shown respectively.

Although one mirror uses a Si_3N_4 grating for narrow-band feedback, the other uses a broadband Si reflector mounted on a tunable Si loop mirror. The interferometer power splitting ratio and, as a result, the total reflectivity are tuned using a thermally regulated Si MZI (Mach–Zehnder interferometer). With zero bias as the initial state, the Si reflector is designed to provide 100% power reflectivity. Between the InP/Si gain and the Si_3N_4 grating, a phase tuner with a thermally tuned heater is used to tune the intra-cavity phase state. For efficient chip-to-fiber coupling and off-chip laser characterization, the E-DBR laser output is passed through a Si_3N_4 grating in a Si_3N_4 waveguide, followed by a Si_3N_4 inverse taper. On demand, the laser output could be sent to other Si_3N_4 photonic integrated circuits and computers.

The Si_3N_4 waveguide in our E-DBR laser is 90 nm thick and 2.8 μm wide, with an

effective mode refractive index of 1.46 and a 5.3 μm^2 effective mode area. The shallow-etched Si waveguide mode is converted to a 269-nm thick Si fully-etch waveguide mode and then tapered to a 150-nm wide taper tip over a 50-µm length to facilitate highly efficient mode conversion between the Si waveguide and Si_3N_4 waveguide. This taper structure was discussed earlier in this Chapter. The laser fabrication is a wafer-scale process that uses a DUV stepper to conduct all of the optical lithography on a 100-mm diameter wafer.

The laser characterization findings are summarized in Fig. 4.15. The output-coupled optical lensed fiber is used to test the laser output power. The chip facet's coupling loss is 3.5 dB from the Si_3N_4 inverse taper. The LI curves for three lasers with different gain section lengths (1.5 mm or 2.5 mm) and different Si_3N_4 grating κ designs (0.25 cm^{-1}, 0.75 cm^{-1}, and 0.875 cm^{-1}), are shown in Fig. 4.15a. For each of these lasers, the Si_3N_4 output waveguide power is higher than 10 mW. The LI measurements show that for higher laser output power, a longer gain section length combined with a smaller grating κ value (weaker grating feedback) is beneficial, as a smaller κ corresponds to a greater mirror loss at the output facet. The laser gain, intrinsic loss, Si/Si_3N_4 taper loss, and Si_3N_4 waveguide loss [4] are used to calculate the minimum κ value, which reflects the minimum grating feedback intensity sustaining lasing conditions.

The laser threshold is also affected by the length of the laser gain portion and the grating feedback. The long external cavity laser has a low laser threshold of 42 mA due to a short gain section length of 1.5 mm and a large grating κ value of 0.875 cm^{-1} (20 mm-long external cavity). In Fig. 4.15b, the Si_3N_4 grating reflection responses for the three lasers in Fig. 4.15a are shown. The smaller grating κ architecture results in a broader reflection bandwidth, but with reduced side lobe suppression (3.5 dB), as shown by the normalized reflection. The grating reflection bandwidth will increase as κ increases. As shown by the red and green curves in Fig. 4.15b, side lobe suppression has a maximum

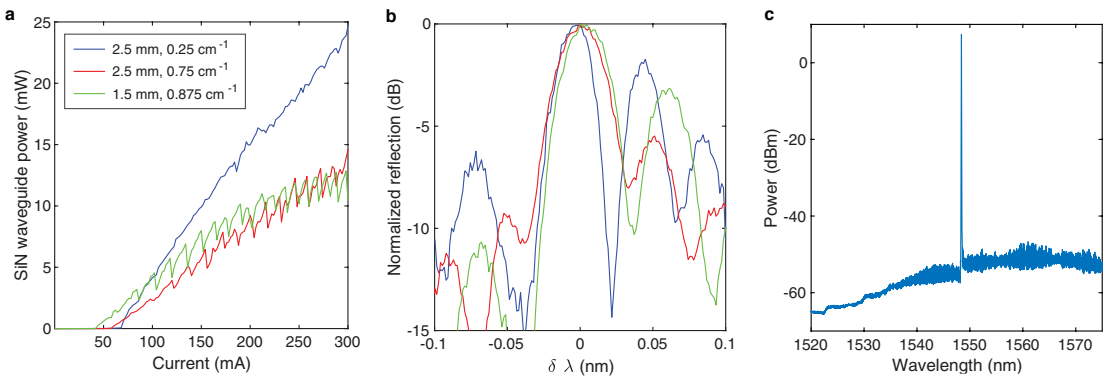

Figure 4.15: a. LI measurements of three lasers with different gain section length (1.5 mm or 2.5 mm) and grating κ values (0.25 cm^{-1}, 0.75 cm^{-1} and 0.875 cm^{-1}). b. Corresponding grating reflection response of lasers measured in a. c. Optical spectrum of high-power laser (shown in blue in a and b) at a gain current of 300 mA.

ratio at a certain κ value and decreases with further increasing κ value.

The Si_3N_4 grating determines the laser wavelength since it provides narrow-band reflection and the Si reflector feedback is broadband. The lasing wavelength is about 1548 nm, and the grating time is 526 nm. With proper phase conditions, single mode operation is accomplished, and the single-mode laser outputs high power inside the mode hop areas, as shown in Fig. At a gain current of 300 mA, the high-power laser with 2.5-mm long gain section and 0.25 cm^{-1} grating κ achieves a side mode suppression ratio (SMSR) of 54 dB (Fig. 4.15c).

The long external cavity created by the extended Si_3N_4 grating allows for a narrow laser linewidth. The laser linewidth for an external cavity laser is $\Delta\upsilon = \Delta\upsilon_0/(1+A+B)$, where $\Delta\upsilon_0$ is the laser Schawlow-Townes linewidth without external feedback, which is determined by the III-V/Si gain section, factor A is the ratio of external passive cavity length (Si waveguide within the laser cavity and Si_3N_4 grating) to the active III-V/Si gain section length, and factor B includes the detuned loading effect which requires a slight red-detuning of the operation wavelength relative to the grating reflection peak[10; 14; 15]. Figure 4.16a shows the frequency noise range of a laser with a relatively

strong grating κ value and a 2.5-mm long gain section. Because of the high grating slope on the long wavelength side of the reflection response, which provides strong negative feedback to reduce the laser linewidth, the Lorentzian linewidth is about 780 Hz. The 1.5 mm-long gain section laser (0.875 cm^{-1} grating κ) also had its relative-intensity-noise (RIN) measured as depicted in 4.16b. The RIN is estimated below -150 dBc/Hz up to 20 GHz for gain currents between 230 and 300 mA. The low RIN is due to the Si_3N_4 grating's narrow bandwidth feedback.

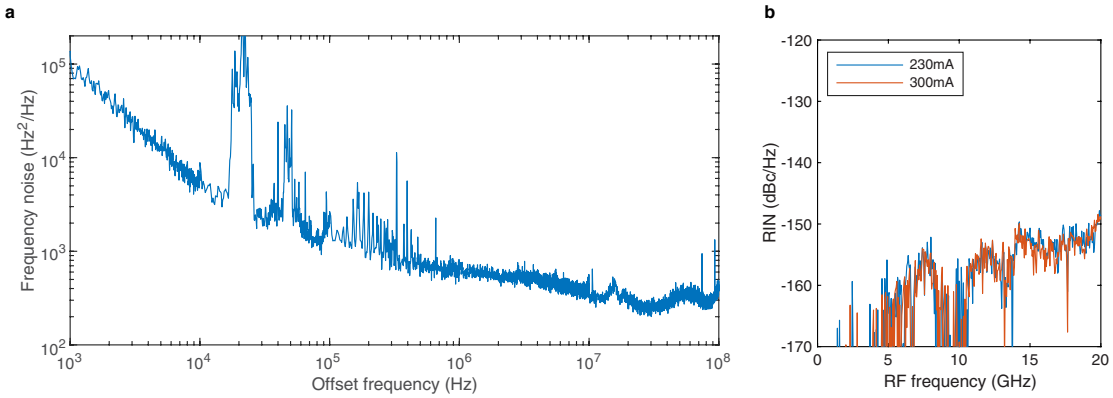

Figure 4.16: a. Laser frequency noise spectrum of a laser with sub-kHz fundamental linewidth and low frequency noise. b. Laser RIN measurements of a low-threshold laser (shown in green in a and b).

The performance of the laser, when is completely integrated with Si_3N_4 photonic integrated circuits, can be further improved by adding ultra-low-loss and ultra-high-Q Si_3N_4 photonics modules. Our laser can be combined with an ultra-high-Q Si_3N_4 ring resonator to create an ultra-low phase noise device. We butt coupled our Si_3N_4 laser with a stand-alone Si_3N_4 high-Q ring resonator with a nominal intrinsic Q factor of about 40 million as a proof-of-concept.

The effect of external cavity input from the resonator on laser coherence is summarized in Fig. 4.17a. Because of the large mode mismatch between the Si and Si_3N_4 waveguides in the E-DBR laser, effective mode transition with low reflection can only be achieved

when the taper tip is narrow. In devices where the taper tip is wider and builds up sufficient feedback, the laser will lase in a Fabry-Pérot (FP) mode (in mode competition with Si_3N_4 grating based lasing) from the wide taper tip and high-reflection reflector, with the output coupled to the Si_3N_4 waveguide. This results in a low-coherence lasing state, with the Si reflector and a series of tapers (III-V/Si to Si taper and Si to Si_3N_4 taper) forming a coupled FP cavity. The laser would have a very low coherence, i.e. a broad laser linewidth, due to the lack of a long external cavity.

The laser feedback is provided by the Si_3N_4 grating for a properly built and highly efficient Si/Si_3N_4 transition taper with low back-reflection, allowing high-coherence lasing and the laser fundamental linewidth is sub-kHz or kHz. The Si_3N_4 grating is part of the external cavity in this situation, and it must be low-loss in order to provide adequate feedback for the Si_3N_4 grating based lasing to work. This method, however, cannot be extended beyond the physical cavity length limit since the grating length is constrained by its physical length (the grating effective cavity length is always shorter than the physical length). Resonant structures such as ring resonators, on the other hand, provide optical delay enhancement based on the Q-factor and the bus waveguide to ring resonator coupling ratio.

One approach is to self-inject lock the laser to an ultra-high-Q ring resonator on the same Si_3N_4 platform to further reduce the laser linewidth. In self-injection locked operation, both the E-DBR and FP lasers performed well with external resonator feedback, with the E-DBR producing the better frequency noise results (Fig. 4.17c), while the FP-based operation can be used to produce frequency combs until it reaches the parametric oscillation threshold (Fig. 4.17d). Facet inverse taper and Si_3N_4 waveguide geometry are similar in our E-DBR laser and Si_3N_4 resonator. The free spectral range of the Si_3N_4 ring resonator is 5 GHz (FSR). Figure 4.17b shows the measured Q factor around the laser wavelength (1548 nm). The intrinsic Q factor for the resonance used for

laser self-injection locking is about 42 million. When the laser wavelength coincides with the Si_3N_4 ring resonance, the feedback signal is produced by Rayleigh scattering at the high-Q resonance inside the ring resonator, resulting in laser self-injection locking. Figure 4.17c shows the E-DBR laser frequency noise before and after self-injection locking. The laser frequency noise is decreased by about 30 dB across the entire frequency spectrum, resulting in a white noise floor of less than 1 Hz^2/Hz, which corresponds to about 3 Hz Lorentzian linewidth. By using an add-drop ring configuration and taking the laser output from the ring resonator's drop port, the phase noise can be further reduced[16].

Optical frequency comb generation is another capability of this integration device, as the laser output power exceeds the high-Q Si_3N_4 ring parametric oscillation threshold. Figure 4.17d shows frequency comb generation from a high-Q Si_3N_4 ring resonator with 30 GHz line spacing, pumped directly from a Si_3N_4 waveguide output by a low-coherence FP laser. Dark pulses can be achieved with this integration platform and normal-dispersion Si_3N_4 waveguides with improved output power. It should be noted that our platform with dispersion-engineered thick Si_3N_4 waveguides for bright soliton generation can also be used to expand the direct pumping scheme using laser self-injection locking for bright soliton generation. The laser and fully integrated III-V/Si/Si_3N_4 structure can thus be used to construct an ultra-low-noise laser and nonlinear photonics platform for a variety of applications, such as coherent optical communications[17], optical clocks[18], and optical/RF frequency synthesizers[19].

4.4 Summary and outlook

This chapter details the design, development and results of heterogeneously integrated lasers on Si_3N_4 [12; 20]. The benefit of integrating Si_3N_4 mainly results from the low propagation loss and low nonlinear loss. This laser, with superior passive cav-

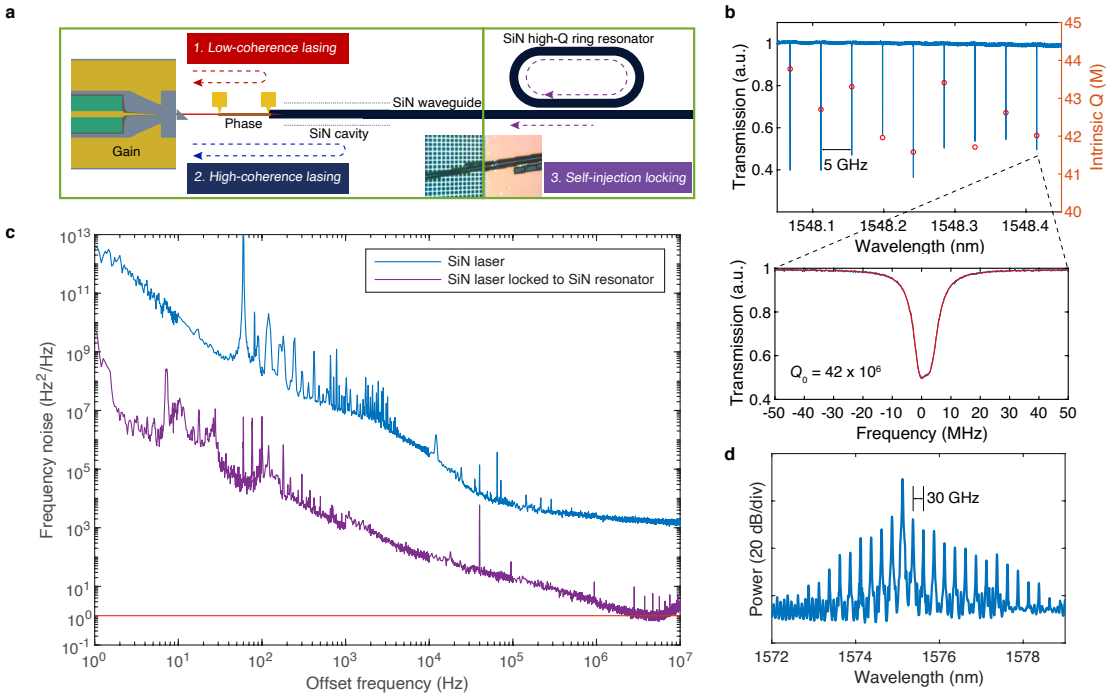

Figure 4.17: a. Three lasing conditions with a III-V/Si/Si_3N_4 platform shown schematically. Each condition employs a unique feedback system, resulting in a unique laser coherence. b. Transmission of a 5 GHz FSR high-Q Si_3N_4 ring resonator and the associated intrinsic Q factor around the Si_3N_4 laser resonance. The fitted curve at the bottom shows the zoomed-in resonance transmission used for self-injection locking (shown in red). c. Laser frequency noise of a high-coherence Si_3N_4 laser locked to a high-Q Si_3N_4 ring resonator with (purple) and without (blue) self-injection. The red reference line represents frequency noise of 1 Hz^2/Hz. d. Frequency comb generation of a high-power laser on a III-V/Si/Si_3N_4 platform self-injection locked to a 30 GHz FSR high-Q ring resonator using an optical spectrum.

ity, would have a lot of room to improve its performance. The laser linewidth, which is extensively discussed in this chapter, is of paramount importance in many applications. Heterogeneous integration offers the possibilities that can not be achieved with a monolithic III-V platform.

One important requirement to achieve a high-performance laser with integrated Si_3N_4 cavity is to have a highly efficiency Si-Si_3N_4 mode transition taper. Due to the index of thin-core Si_3N_4 waveguide is approaching the SiO_2 index, the Si taper tip needs to be

reduced to around 150 nm wide. For a thicker the Si_3N_4 layer, the Si taper can be made wider. The conformal shape of the taper is also important to maintain a high adiabatic transition efficiency. Also, a better matched modal index with Si_3N_4 also results in less reflection, which is detrimental to the lasing stability and lasing mode selectivity.

As stated in Chapter 3, the approach of integrate passive waveguides also includes Si waveguide. While Si_3N_4 waveguide is projected to be with preferable properties for the narrow laser linewidth than Si, III-V/Si has been developed for more than a decade. Its performance is still being improved through techniques including the use of extended Si waveguide for lower propagation loss and also lower nonlinear loss[21; 22]. Based on multiple ring resonators, the optical cavity can be extended without losing single mode selectivity. One benefit of Si-based laser cavity over Si_3N_4-based laser cavity is the group index of Si waveguide is more than 2x higher than thin-core Si_3N_4 waveguide, thus at same physical length and ring coupler coefficient, Si-based cavity offers more than 2x larger optical delay, which corresponds to 2x factor A in linewidth reduction theory as introduced before.

Ring resonators provide the required wide tunability for many applications. Vernier rings, which are very effective in extending the effective FSR of ring resonators, enabled $>$ 120 nm tuning range in a III-V/Si tunable laser using four ring resonators based on extended Si waveguides[21–23]. This progress, are predicted to be continued with Si_3N_4 ring resonators using the cavity described in Chapter 3.

The state-of-the-art performance of a 3-ring III-V/Si laser with sub-100 Hz Lorentzian linewidth, the demonstrated III-V/Si/Si_3N_4 DBR laser and a benchmark table-top Agilent 81680A tunable laser are compared in Fig. 4.18. It can be seen that the heterogeneous lasers are already having better linewidth performance than the bulky table-top laser. Green curve is a reference frequency noise plot from DFB injection locked to high-Q Si_3N_4 ring resonator which has 1.2 Hz fundamental linewidth[16]. Future directions of

III-V/Si/Si_3N_4 narrow linewidth integration thus can be categorized into widely tunable lasers using multiple Si_3N_4 ring resonators[24] and directly on-chip self-injection locking with ultra-high-Q ring resonator. The frequency noise of high-Q ring resonators are ultimately limited by the thermorefractive noise, which can be reduced with larger mode volume, i.e. a larger ring radius and smaller ring FSR[25].

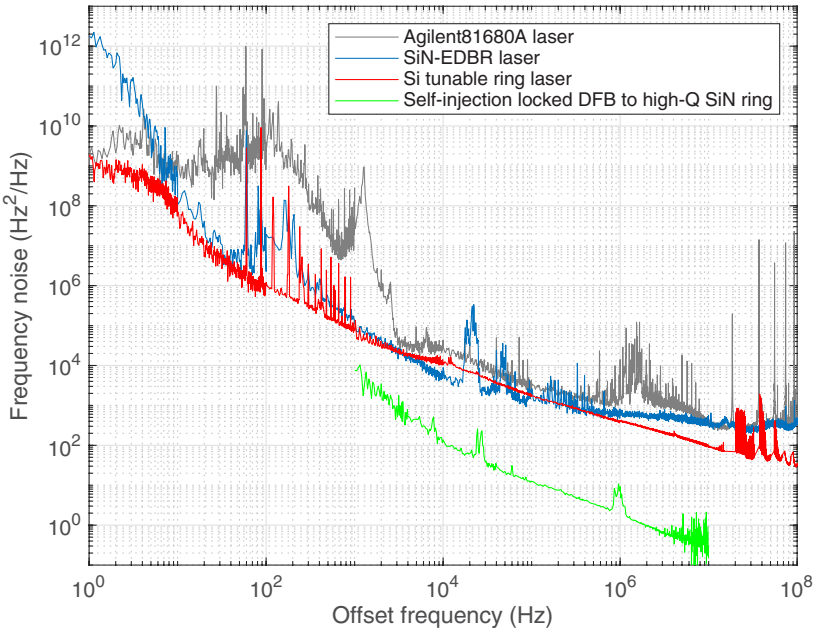

Figure 4.18: Frequency noise comparison of 3-ring III-V/Si widely tunable laser, III-V/Si/Si_3N_4 DBR laser, Agilent 81680A tunable laser and DFB lase self-injection locked ultra-high-Q Si_3N_4 ring resonator.

References

[1] F. L. Riley, *Silicon nitride and related materials*, *Journal of the American Ceramic Society* **83** (2000), no. 2 245–265.

[2] T. Komljenovic, D. Huang, P. Pintus, M. A. Tran, M. L. Davenport, and J. E. Bowers, *Photonic Integrated Circuits Using Heterogeneous Integration on Silicon*, *Proceedings of the IEEE* **106** (Dec., 2018) 2246–2257.

[3] R. Jones, P. Doussiere, J. B. Driscoll, W. Lin, H. Yu, Y. Akulova, T. Komljenovic, and J. E. Bowers, *Heterogeneously Integrated InP/Silicon Photonics: Fabricating Fully Functional Transceivers*, *IEEE Nanotechnology Magazine* **13** (Apr., 2019) 17–26.

[4] C. Xiang, P. A. Morton, and J. E. Bowers, *Ultra-narrow linewidth laser based on a semiconductor gain chip and extended Si_3N_4 Bragg grating*, *Optics Letters* **44** (2019), no. 15 3825–3828.

[5] M. Bruel, B. Aspar, and A.-J. Auberton-Hervé, *Smart-cut: a new silicon on insulator material technology based on hydrogen implantation and wafer bonding*, *Japanese journal of applied physics* **36** (1997), no. 3S 1636.

[6] M. L. Davenport, *Heterogeneous silicon III-V mode-locked lasers*. PhD thesis, UC Santa Barbara, 2017.

[7] L. A. Coldren, S. W. Corzine, and M. Mashanovitch, *Diode lasers and photonic integrated circuits*. Wiley, 2012.

[8] C. Zhang, D. Liang, G. Kurczveil, J. E. Bowers, and R. G. Beausoleil, *Thermal management of hybrid silicon ring lasers for high temperature operation*, *IEEE Journal of Selected Topics in Quantum Electronics* **21** (2015), no. 6 385–391.

[9] P. A. Morton and M. J. Morton, *High-power, ultra-low noise hybrid lasers for microwave photonics and optical sensing*, *J. Lightwave Technol.* **36** (Nov, 2018) 5048–5057.

[10] K. Vahala and A. Yariv, *Detuned loading in coupled cavity semiconductor lasers—effect on quantum noise and dynamics*, *Applied Physics Letters* **45** (1984), no. 5 501–503.

[11] R. Bergh, H. Lefevre, and H. Shaw, *An overview of fiber-optic gyroscopes*, *Journal of Lightwave Technology* **2** (1984), no. 2 91–107.

[12] C. Xiang, J. Guo, W. Jin, J. Peters, W. Xie, L. Chang, B. Shen, H. Wang, Q.-F. Yang, L. Wu, *et. al.*, *High-performance lasers for fully integrated silicon nitride photonics*, *arXiv preprint arXiv:2104.08414* (2021).

[13] M. L. Davenport, S. Skendžić, N. Volet, J. C. Hulme, M. J. Heck, and J. E. Bowers, *Heterogeneous silicon/iii–v semiconductor optical amplifiers*, *IEEE Journal of Selected Topics in Quantum Electronics* **22** (2016), no. 6 78–88.

[14] C. Henry, *Theory of the linewidth of semiconductor lasers*, *IEEE Journal of Quantum Electronics* **18** (1982), no. 2 259–264.

[15] T. Komljenovic and J. E. Bowers, *Monolithically integrated high-q rings for narrow linewidth widely tunable lasers*, *IEEE Journal of Quantum Electronics* **51** (2015), no. 11 1–10.

[16] W. Jin, Q.-F. Yang, L. Chang, B. Shen, H. Wang, M. A. Leal, L. Wu, M. Gao, A. Feshali, M. Paniccia, *et. al.*, *Hertz-linewidth semiconductor lasers using cmos-ready ultra-high-q microresonators*, *Nature Photonics* (2021) 1–8.

[17] G. M. Brodnik, M. W. Harrington, J. H. Dallyn, D. Bose, W. Zhang, L. Stern, P. A. Morton, R. O. Behunin, S. B. Papp, and D. J. Blumenthal, *Optically synchronized fiber links with spectrally pure integrated lasers*, *arXiv preprint arXiv:2102.05849* (2021).

[18] Z. L. Newman, V. Maurice, T. Drake, J. R. Stone, T. C. Briles, D. T. Spencer, C. Fredrick, Q. Li, D. Westly, B. R. Ilic, B. Shen, M.-G. Suh, K. Y. Yang, C. Johnson, D. M. S. Johnson, L. Hollberg, K. J. Vahala, K. Srinivasan, S. A. Diddams, J. Kitching, S. B. Papp, and M. T. Hummon, *Architecture for the photonic integration of an optical atomic clock*, *Optica* **6** (May, 2019) 680–685.

[19] D. T. Spencer, T. Drake, T. C. Briles, J. Stone, L. C. Sinclair, C. Fredrick, Q. Li, D. Westly, B. R. Ilic, A. Bluestone, N. Volet, T. Komljenovic, L. Chang, S. H. Lee, D. Y. Oh, M.-G. Suh, K. Y. Yang, M. H. P. Pfeiffer, T. J. Kippenberg, E. Norberg, L. Theogarajan, K. Vahala, N. R. Newbury, K. Srinivasan, J. E. Bowers, S. A. Diddams, and S. B. Papp, *An optical-frequency synthesizer using integrated photonics*, *Nature* **557** (2018), no. 7703 81–85.

[20] C. Xiang, W. Jin, J. Guo, J. D. Peters, M. J. Kennedy, J. Selvidge, P. A. Morton, and J. E. Bowers, *Narrow-linewidth III-V/Si/Si$_3$N$_4$ laser using multilayer heterogeneous integration*, *Optica* **7** (Jan, 2020) 20–21.

[21] M. A. Tran, D. Huang, T. Komljenovic, J. Peters, A. Malik, and J. E. Bowers, *Ultra-low-loss silicon waveguides for heterogeneously integrated silicon/iii-v photonics*, *Applied Sciences* **8** (2018), no. 7 1139.

[22] M. A. Tran, D. Huang, J. Guo, T. Komljenovic, P. A. Morton, and J. E. Bowers, *Ring-resonator based widely-tunable narrow-linewidth si/inp integrated lasers*, *IEEE Journal of Selected Topics in Quantum Electronics* **26** (2019), no. 2 1–14.

[23] M. A. Tran, D. Huang, and J. E. Bowers, *Tutorial on narrow linewidth tunable semiconductor lasers using si/iii-v heterogeneous integration*, *APL photonics* **4** (2019), no. 11 111101.

[24] C. Xiang, P. A. Morton, J. Khurgin, C. Morton, and J. E. Bowers, *Widely tunable Si_3N_4 triple-ring and quad-ring resonator laser reflectors and filters*, in *2018 IEEE 15th International Conference on Group IV Photonics (GFP)*, pp. 1–2, IEEE, 2018.

[25] G. Huang, E. Lucas, J. Liu, A. S. Raja, G. Lihachev, M. L. Gorodetsky, N. J. Engelsen, and T. J. Kippenberg, *Thermorefractive noise in silicon-nitride microresonators*, *Phys. Rev. A* **99** (Jun, 2019) 061801.

Chapter 5

Integrated laser soliton microcombs

This chapter covers the demonstration of the fist heterogeneouly intergated soliton microcomb device. This work in done in collaboration with Dr. Junqiu Liu, Dr. RuiNing Wang, Dr. Wenle Weng, Dr. Johann Riemensberger and Prof. Tobias J. Kippenberg from Laboratory of Photonics and Quantum Measurements (LPQM) at the Swiss Federal Institute of Technology (EPFL).

5.1 Introduction of microcombs

Optical frequency combs (OFC) [1; 2] have revolutionized timing, spectroscopy and metrology[3; 4]. Historically, frequency comb generation requires table-top exceptionally high-power discrete lasers, amplifiers, and complicated controls. Recent-decade developments of photonic integration play a key role in pushing the optical frequency combs technology into a new regime, where microresonator-based frequency combs (soliton microcombs), leveraging CMOS-compatible and wafer-scale production of high-Q silicon nitride (Si_3N_4) microresonators, lower the power threshold to tens of milliwatts which is compatible with state-of-the-art diode lasers. Hybrid packaging of a diode laser with

a high-Q microresonator enabled direct-pumping soliton microcombs generation and inspired a series of frequency combs research[5–7]. Rich dynamics are being explored in a coupled laser-resonator system that offers new operation points with unprecedented control on the soliton microcomb generation.

One long-lasting goal of frequency comb research is to fully integrate appropriate laser sources to directly generate high-quality frequency combs. To date, compared with mode-locked lasers, which generate narrow-band, mode-locked frequency combs, the laser integration for broadband Kerr frequency comb is still limited to using separated chips due to scientific and technical challenges. High-power, high-coherence pump lasers are difficult to integrate with high-Q microresonators as multiple material systems need to be deployed. The lack of such devices hinders how soliton microcombs application can scale up into complex systems. Future perspective of soliton microcombs applications requires reliable and mass-manufacturable microcombs with laser integration at the same scale, and ideally on a cost-effective platform with low power consumption. Heterogeneously integrated silicon photonics offers a compelling solution using low-cost silicon substrates. High-performance, large-scale heterogeneously integrated silicon photonic circuits with complete photonic elements, including lasers, modulators, photodetectors, etc., disrupt the optical interconnect technology and beyond. Here, we report the merge of soliton microcombs and heterogeneous silicon photonics to form novel integrated laser soliton microcombs on silicon. Our device is the first demonstration of full integration of lasers and microresonator frequency combs and opens a new era of soliton microcomb research.

There are various integrated platform that developed the capability of optical frequency comb generation and soliton generation. These include Si_3N_4[8–12], AlN[13; 14], $LiNbO_3$[15–17], AlGaAs[18–20], GaP[21], and SiC[22]. The leading platform is Si3N4, which has already been commonly used as diffusion barriers and etch masks in CMOS microelectronics. In addition to its inherent properties, such as the lack of two-photon

absorption, high Kerr nonlinearity, and weak Raman and Brillouin gains [23], recent advances in fabrication of nonlinear Si_3N_4 photonic integrated circuits (PIC) have allowed optical propagation losses of less than 1 dB/m [10; 24]. These ultralow losses have significantly reduced the soliton formation threshold power to levels that integrated lasers can provide , and have resulted in microwave X-band soliton repetition rates [25]. Dispersion engineered thick Si_3N_4 waveguides with anomalous dispersion are required to generate bright solitons[26; 27]. Photonic Damascence process overpasses cracking issues from the intrinsic high stress of thick Si_3N_4 films and enabled wafer-scale process of low-loss, high-yield dispersion engineered Si_3N_4 photonic circuits [24; 28–31]. In this work, the Si_3N_4 ring resonators and required top cladding polarization are provided by EPFL-LPQM [32].

5.2 Integrated laser soliton microcombs

The developed multilayer heterogeneous integration techniques in this thesis fit naturally in such applications as lasers and high-Q Si_3N_4 ring resonators can be effectively integrated on a common monolithic Si substrate. The demonstrated devices individually consist of three main parts, i.e., a distributed feedback (DFB) laser, a thermo-optic phase tuner, and a high-Q microresonator. As illustrated in Fig. 5.1a, DFB lasers, phase tuners, and high-Q microresonators are built on indium phosphide/silicon (InP/Si), silicon (Si), and Si_3N_4 layers, respectively. This stacked structure (Fig. 5.1b) is enabled by wafer bonding silicon-on-insulator (SOI) wafer and InP multiple-quantum-well (InP MQW) epi wafer to a pre-fabricated Si_3N_4 wafer in sequence. The processing has lithographically-defined alignment accuracy around 100 nm using a deep ultra-violet (DUV) stepper. Noteworthily, heterogeneous integration enables device fabrication at wafer-scale (100 mm diameter Si substrate wafers are currently employed and can be scaled up to larger substrates). Device images in Fig. 5.2 show the complete wafer, die-level devices, and a

high-Q Si_3N_4 ring resonator with a silicon interface.

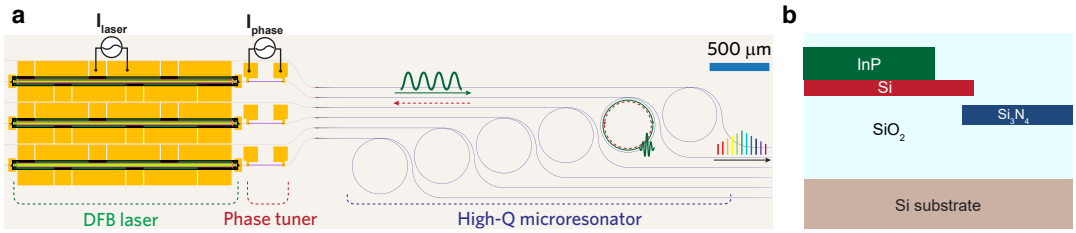

Figure 5.1: Schematic illustration of the integrated laser soliton microcomb device compromising DFB laser, phase tuner and high-Q Si_3N_4 ring resonator. Right picture shows a simplified side-view schematic of the integrated device.

Figure 5.3a shows schematic the wafer-scale integration of such devices. The DFB laser provides a high-power, single longitudinal-mode pump source with an excellent side mode suppression ratio (SMSR). It has a 1.8 mm-long InP/Si gain section, and the grating is etched at both sides of the shallow-etched silicon waveguide rib with 170 nm gap separation to the silicon waveguide core. The fully etched grating provides the optical resonant feedback for the pump laser and determines the lasing wavelength by its pitch size ($\lambda_{pump} = 2n_{eff}\Lambda$). Here the grating pitch size is 238 nm, which provides a center wavelength around 1550 nm. A quarter wavelength shift section is included at the grating length center to supply non-degenerate phase conditions favoring single longitudinal mode lasing. Single-wavelength laser output passes through the thermo-optic resistive heater with its phase controlled and couples to the high-Q ring resonator where degenerate nonlinear four-wave mixing process generates Kerr frequency combs. The high-Q ring resonator is dispersion-engineered to yield an anomalous dispersion across telecommunication C band and has a free-spectral range (FSR) of 100 GHz.

Laser direct pumping the resonator without intermediate optical isolator highlights such devices' operation principle (Fig. 5.3b). Optical self-injection locking leverages the narrow-band optical feedback at desired phase relations from a high-Q ring resonator to

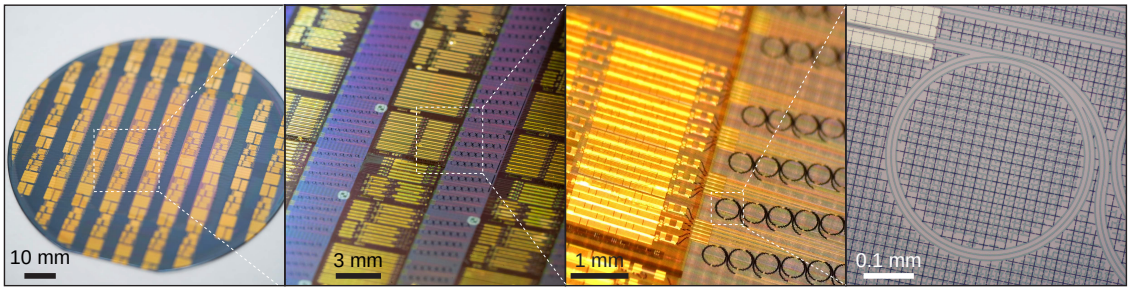

Figure 5.2: Photographs showing the completed 100-mm-diameter wafer, zoom-in of multiple laser soliton microcomb dies, and a microscopic image showing a Si_3N_4 microring resonator with Si/ Si_3N_4 interface.

stabilize the pump laser and pulls the laser frequency towards the ring resonance where optimum laser-resonator detuning is satisfied to generate optical frequency combs. In such an operation, the laser current and phase tuner current is controlled, where no sophisticated electronics feedback controls are required. The DFB lasing wavelength follows the laser current as the grating index increases due to injected electrical power heating. As a result, certain gain currents are permitted to give rise to comb generation if the corresponding lasing wavelength coincides with the ring resonator resonance (Fig. 5.3c). Additionally, the backscattered signal needs to satisfy certain phase relations (see Supplementary Information for details). The frequency comb generation region resides in where required laser-resonance detuning and phase conditions are both fulfilled. The back-reflected signal originates from Rayleigh scattering inside the microresonator due to surface roughness and bulk inhomogeneity.

The device fabrication process is summarized in Fig. 5.4, with key steps shown in the cross-sectional schematic view. It starts with photonic Damascene making high-Q Si_3N_4 ring resonators with thick Si_3N_4 layer thickness (750 nm). Chemical mechanical polishing (CMP) is used to remove excess deposited Si_3N_4 material, followed by spacer oxide deposition and second CMP for flat and smooth surface to be bonded with SOI wafer. After substrate removal of the bonded SOI wafer, the Si device layer is processed

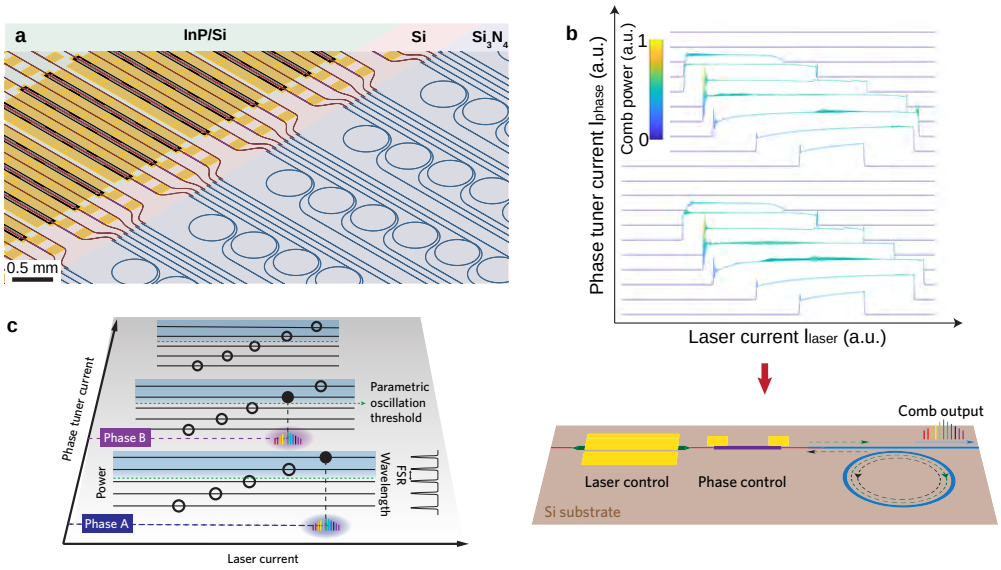

Figure 5.3: a. Schematic illustration of the wafer scale integration of laser soliton microcombs. b. Operation principle of electrically controlled soliton generation. c. Simple illustration of how the soliton microcomb can be generated at certain laser and phase tuner current.

to realize silicon waveguides with different etching depths, which includes shallow-etched Si waveguide for the laser and phase tuner, fully etched hole structure for grating, and thin-thickness Si taper for mode transition to underneath Si_3N_4 waveguides. InP MQW epi is then bonded to the patterned Si device surface at active regions. The InP process includes InP substrate removal, P-type, QW, and N-type mesa etch, P- and N-type contact metal deposition, passivation, VIA open, heater formation, and probe metal formation.

The roughness after second CMP of the Si_3N_4 upper cladding is below 0.3 nm and help enable a high SOI bonding yield (Fig. 5.5a). SEM image shows the Si grating which provides the required laser feedback. The FIB-SEM image of the device cross at sectional view shows the device's multiplayer nature (Fig. 5.5c).

The device characterization starts with laser performance measurements (Fig. 5.6a). Standard light-current curves with stepped laser current (0.5 mA), fixed phase tuner

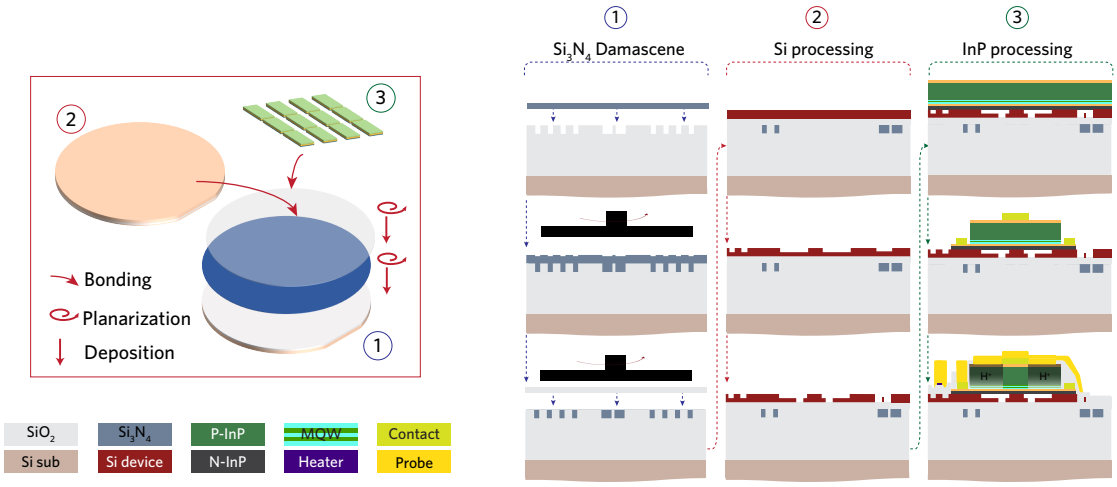

Figure 5.4: Simplified device fabrication process. Left panel shows that a pre-patterned Si_3N_4 Damascene substrate is planarized and subsequently bonded with an SOI wafer and an InP MQW epi wafer. The wafer undergoes 1.) Si_3N_4 photonic Damascene process, 2.) Si processing and 3.) InP processing. Right panel shows selected key steps in the wafer fabrication with 1.) Si_3N_4 photonic Damascene process including LPCVD Si_3N_4 deposition on the patterned SiO_2 substrate (top), excess Si_3N_4 removal and planarization (middle), and SiO_2 spacer deposition, densification and polishing (bottom); 2.) Si processing including Si substrate removal (top), Si waveguide etch for laser and thermal tuner (middle), and for Si grating and Si-Si_3N_4 mode conversion taper (bottom); 3.) InP processing including InP substrate removal (top), InP mesa etch (middle), and excess Si removal, laser passivation, contact formation, vias open, heaters, and probe metal formation (bottom).

current of 7 mA, and 20 degree Celsius stage temperature is shown in Fig. 5.6b. The laser threshold is 64 mA, and the maximum fiber-coupled output power is 8 mW, which corresponds to 20 mW in the Si_3N_4 waveguide. The laser center wavelength is also recorded with a wavemeter (shown in grey color). Several dips on the laser output power are seen at laser current of 133mA, 231mA, 329.5mA, and 418 mA where the laser wavelength coincides with the ring resonances. The recorded laser wavelength at corresponding laser currents confirmed the ring resonance spacing to be close to 100 GHz. The slight deviation is attributed to the ring resonance redshift due to injected current heating at elevated laser currents. It needs to be noted that HR coating with

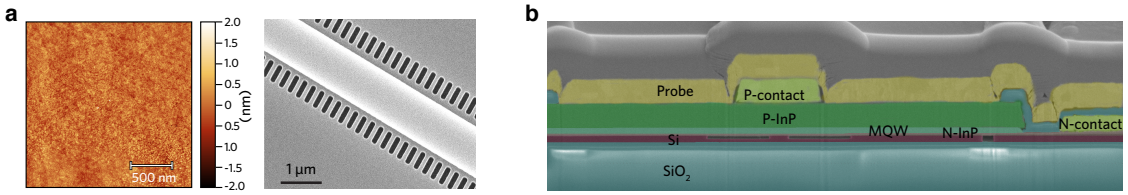

Figure 5.5: a. Left: Atomic-force microscopy (AFM) shows 0.27 nm RMS roughness of the Si_3N_4 wafer surface, after the second CMP on the SiO_2 spacer, before bonding with the SOI wafer. Right: SEM image of Si grating for laser before bonded with InP MQW wafer. b. False-colored SEM image showing the cross-section of the complete device at laser area with multilayer device structure.

70% reflectivity is applied on the other side of the DFB laser to boost the laser output power. Future devices can eliminate this coating to yield mode-hop-free DFB lasers and linearized laser wavelength dependence on the laser current. The DFB laser has high SMSR at resonance 1 and 2, where high output powers are also present and suitable for frequency comb generation. Fig. 3C shows the single-mode laser spectra at the two resonance wavelengths, with 60 dB and 57 dB SMSR, respectively.

The integrated laser soliton microcomb is generated by simply biasing laser current to match the laser wavelength with the ring resonance, together with proper phase tuner current to adjust the relative forward/backward phase relations. The generated states are mainl determined by the intra-cavity power and laser-resonance detuning. The 133 mA and 231 mA gain current does not provide enough laser power to generate frequency combs. At around 329 mA gain current, the 16 mW laser output power exceeds the parametric oscillation threshold and can supply enough frequency comb generation power. Indeed, we found this power level can also generate perfect soliton crystal states by finely tuning the laser wavelength into deep resonance (Fig. 5.7). We observed soliton crystal states with decreasing crystallization orders when increasing the laser current. With further increased laser power at around 418 mA, soliton crystal states with 200 GHz repetition rate and single soliton state with 100 GHz repetition rate are generated. The

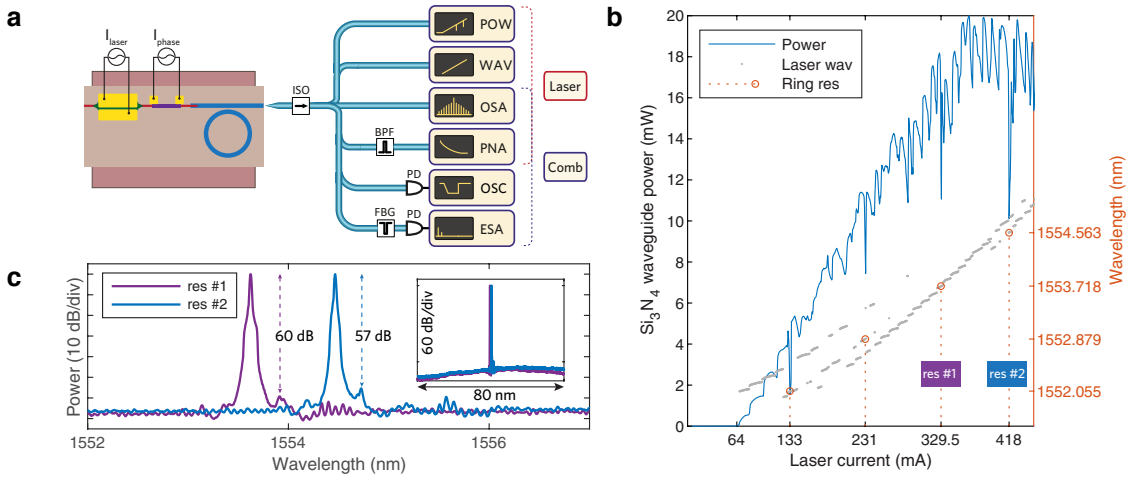

Figure 5.6: a. Schematics of the experimental setup for laser and soliton characterization. I_{laser} and I_{phase} are the current sources to drive the laser and the phase tuner. POW: power meter. WAV: wavelength meter. OSA: optical spectrum analyzer. PNA: phase noise analyzer. OSC: oscilloscope. ESA: electrical spectrum analyzer. ISO: isolator. BPF: band-pass filter. PD: photodetector. b. Light-current sweep measurement with stepped laser current and fixed phase tuner current. Grey color shows the corresponding laser center wavelength as a function of the laser current. Red circles indicate the laser wavelength coinciding with microresonator resonances. Soliton microcombs are generated with laser currents and wavelengths at resonance #1 and resonance #2. c. Single-mode DFB laser spectra at the wavelengths of resonance #1 and resonance #2.

low-noise soliton state is confirmed by the photodetection of the comb lines beat signal. The soliton states shown here, once generated, can be stable for at least hours in standard lab environments without any external control. The high stability is benefited from the single-chip nature of the device, which creates thermal equilibrium, and the fact that no moving parts or any free space coupling are required to maintain the frequency combs state.

To further study the self-injection locking phenomenon, we first measured the frequency noise of the pump line and comb line at soliton state and compared them to the laser free-running state (Fig. 5.8). One prominent effect of self-injection locking is to leverage the high-Q cavity to reduce the laser phase noise, i.e., the laser linewidth. The

free running DFB laser's fundamental linewidth is around 60 kHz, while it is reduced to about 25 Hz for the self-injection locked pump line in the single soliton state. The frequency noise reduction effect is effective across the full frequency range. Over 30 dB noise reduction is observed above 300 kHz, and this reduction is reduced to about 10 dB down to 1 kHz. Further frequency noise reduction is expected by utilizing a larger ring resonator (smaller FSR and lower thermal-refractive noise) with more substantial back reflection. Due to the linewidth narrowing effect, a relative frequency-noisy semiconductor laser can be used for direct pumping narrow-bandwidth resonators, surpassing

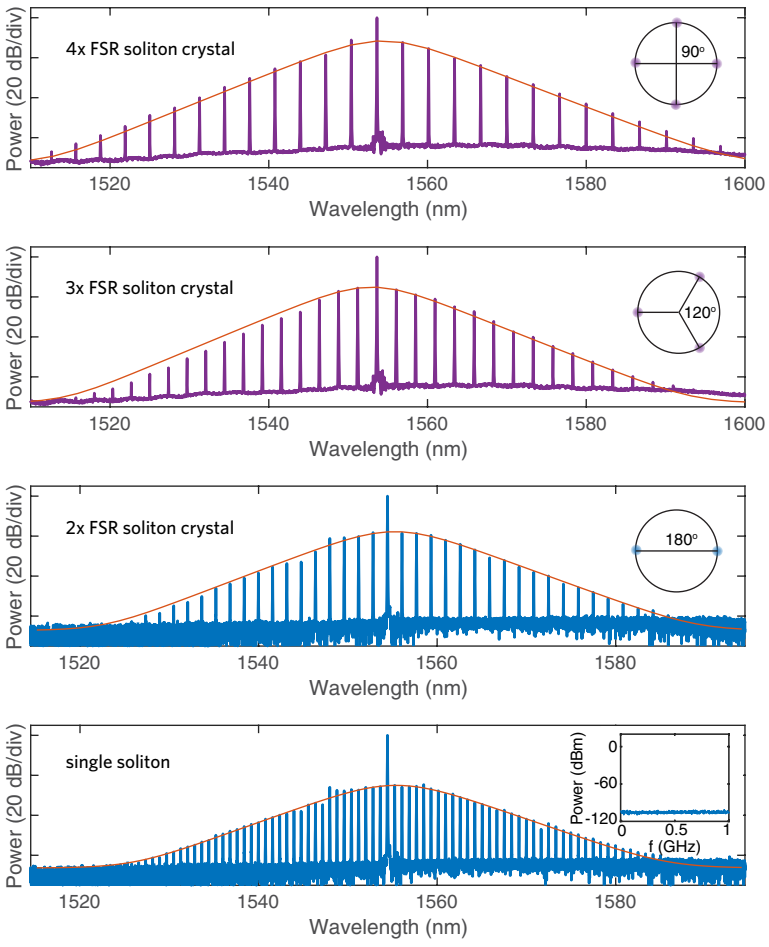

Figure 5.7: Optical spectra of the generated soliton frequency comb states.

the limitation from its spectral impurity. In the meantime, the low-frequency noise for the locked pump line is also transferred to the comb lines coherently. For example, the first neighboring comb lines have fundamental linewidth around 200 to 300 Hz, and their frequency noise below 10 MHz directly duplicate the self-injection locked pump line. This self-injection locking scheme thus enables multi-wavelength narrow-linewidth laser sources.

Another phenomenon that distinguishes the self-injection locking direct pumping scheme with conventional pumping with an optical isolator is the importance of phase relations between the forward and backward signal. In direct pumping with self-injection locking, the feedback phase needs to be in a certain range to facilitate the comb generation. In our device, this can be directly controlled by the phase tuner current. We studied the frequency comb generation with laser current sweep at different phase tuner current conditions. In order to exclude the interference from the mode hop phenomenon

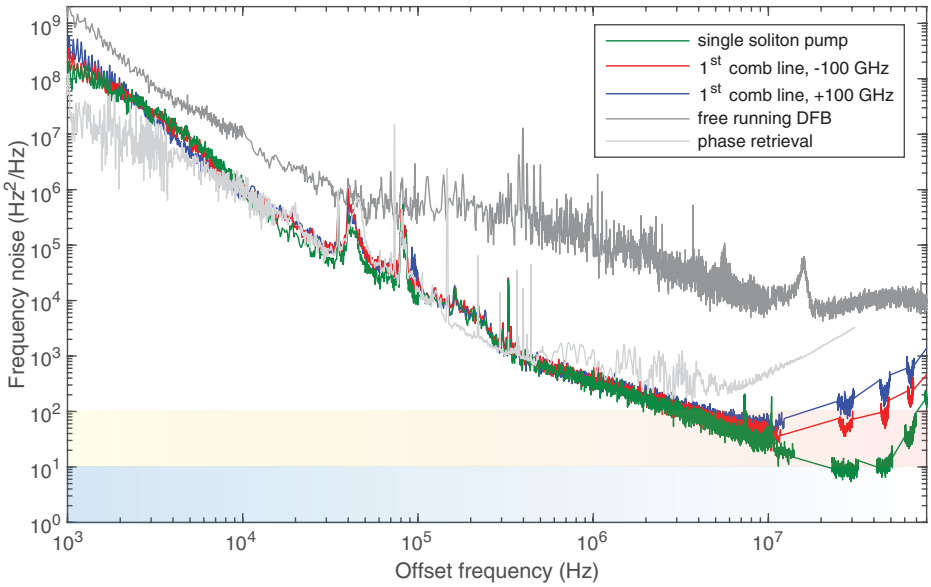

Figure 5.8: Measured frequency noise of pump line and comb lines of the self-injection locked single soliton states, and their comparison with the free-running DFB laser.

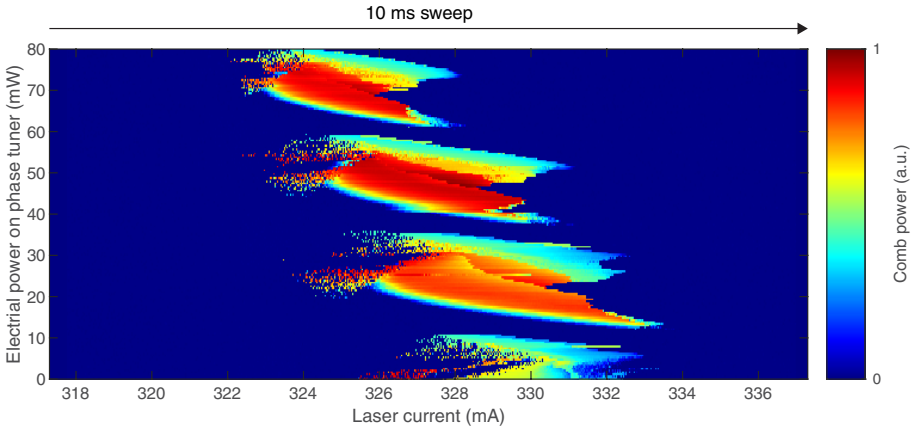

Figure 5.9: Comb power evolution with sweeping laser current (10 milliseconds sweep) under varying electrical power on the phase tuner.

when monitoring new frequency components power, we sweep the laser current across resonance #1 shown in Fig. 5.6b. Results shown in Fig. 5.9 unveil that the frequency comb generation is only permitted at certain phase conditions when the feedback signal can be in phase with the forward signal. Additionally, the phase altering effect is periodic and deterministic with the applied electrical power on the phase tuner. The allowed comb generation area is mainly dependent on the pump laser power and the backscatter intensity. Precise phase tuning thus offers a new route to control the integrated soliton microcomb generation.

5.3 Yield analysis

Our fabrication is done on a wafer with a diameter of 100 mm. The SOI to Si_3N_4/SiO_2 bonding as well as the InP to Si bonding are both necessary to create a multilayer structure. Because there has been substantial research on wafer-scale, high-yield fabrication of high-Q Si_3N_4 microresonators and heterogeneously integrated InP/Si lasers [11], the combined bonding yield of the two bonding stages determines our ultimate device yield.

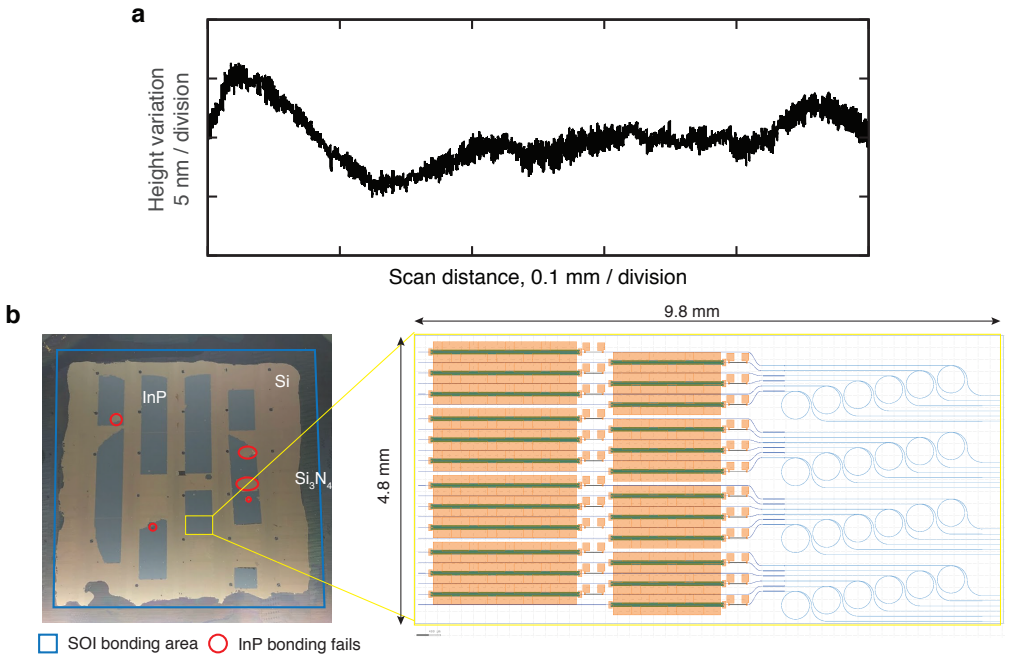

Figure 5.10: a. Measured long-range surface topography of the polished Damascene Si_3N_4 substrate, before SOI bonding. b. Photograph showing the under-processing wafer with bonded SOI and bonded InP. The substrates of SOI and InP are removed completely. The Si_3N_4, Si and InP layers are labeled and discerned by the colors. Blue rectangle marks the SOI bonding area, red circles mark the failed InP bonding area. Yellow rectangle corresponds to an area of around 9.8×4.8 mm^2 containing 24 complete laser soliton microcomb devices.

For high fabrication yield, the first SOI to Si_3N_4/SiO_2 bonding on the patterned Damascene substrate is the most important step. To get a high bonding yield with SOI, surface topological variation and roughness must be minimized. Figure 5.10a displays the measured long-range topography utilizing a surface stylus profiler, whereas Fig. 5.5a displays the 0.27 nm RMS roughness of the polished wafer surface.

A linear height change of roughly 120 nm is seen throughout a 0.5 mm scan distance of the stylus due to stylus drift and wafer total thickness variation (TTV, in our case TTV is < 5 µm). Because this linear fluctuation has no effect on surface flatness, eliminating it reveals our wafer surface with a 10 nm height fluctuation across a 0.5 mm stylus scan distance. The surface flatness of our polished, patterned Si_3N_4 Damascene substrate,

ready for SOI bonding, is represented by this 10 nm / 0.5 mm ratio. Surface flatness lower than this standard frequently leads to serious bonding failures.

A photo of the wafer after InP bonding and substrate removal is shown in Fig. 5.10b. The bonding of a large SOI piece (about 60×60 mm^2 size) fails only at the periphery border area, with the majority of the area demonstrating a strong bonding yield ($> 80\%$). The InP epi dies are attached to the laser gain area selectively. To preserve InP epi, not all of the useful Si area on the current wafer is bonded with InP. On the area where Si bonding yield is high, InP dies that are cleaved from half of a 2-inch InP MQW epi wafer are bonded. The bonding result in Fig. 5.10b depicts five bonding failure areas (red circles) caused by accidental particles. Better surface cleaning and epi handling can help prevent these failures in the future. The failing area is merely a fraction of the entire bonded area (less than 10%) and the bonding yield of InP is greater than 90%.

The finished substrate comprises many devices due to its huge area and good bonding yield after two bonding stages. In Fig. 5.10b, the marked yellow box corresponds to around 9.8×4.8 mm^2 area and comprises 24 full laser soliton microcomb devices. It demonstrates the feasibility of producing a thousand identical devices using the same device designs as previously discussed.

5.4 Summary and outlook

In summary, this chapter details the design, development and measurements of the first heterogeneously integrated soliton microcombs. The key of the device success originates the wafer-scale production of high-Q Si_3N_4 ring resonators and efficient laser integration through multilayer heterogeneous integration. The demonstrated device can be a key step towards many applications including:

1. Direct on-chip low-noise photonic microwave signal synthesis using soliton microcombs[33]

2. Integrated ultra-high-density optical transceiver[34]

3. Integrated nonlinear photonic integrated circuits incorporating χ^2 and χ^2 materials ($LiNbO_3$, AlGaAs, etc) [16; 19]

4. Device prototype for optical-frequency synthesizer [35], Brillouin gyroscope [36], photonic atomic clocks [37] etc.

The integration of lasers and high-Q devices opens up a complete new route for integrated photonics research with unprecedented control on the device performance. The miniaturization of table-table bulky devices on a size smaller than a coin and large reduction of power consumption is another prime example of the advantages of photonic integration. Heterogeneous integration techniques, that is further developed in this thesis, could greatly enrich the photonic functionalities[32].

References

[1] T. Udem, R. Holzwarth, and T. W. Hänsch, *Optical frequency metrology*, *Nature* **416** (03, 2002) 233.

[2] S. T. Cundiff and J. Ye, *Colloquium: Femtosecond optical frequency combs*, *Rev. Mod. Phys.* **75** (Mar, 2003) 325–342.

[3] T. Fortier and E. Baumann, *20 years of developments in optical frequency comb technology and applications*, *Communications Physics* **2** (2019), no. 1 153.

[4] S. A. Diddams, K. Vahala, and T. Udem, *Optical frequency combs: Coherently uniting the electromagnetic spectrum*, *Science* **369** (July, 2020).

[5] B. Stern, X. Ji, Y. Okawachi, A. L. Gaeta, and M. Lipson, *Battery-operated integrated frequency comb generator*, *Nature* **562** (2018), no. 7727 401–405.

[6] A. S. Raja, A. S. Voloshin, H. Guo, S. E. Agafonova, J. Liu, A. S. Gorodnitskiy, M. Karpov, N. G. Pavlov, E. Lucas, R. R. Galiev, A. E. Shitikov, J. D. Jost, M. L. Gorodetsky, and T. J. Kippenberg, *Electrically pumped photonic integrated soliton microcomb*, *Nature Communications* **10** (2019), no. 1 680.

[7] B. Shen, L. Chang, J. Liu, H. Wang, Q.-F. Yang, C. Xiang, R. N. Wang, J. He, T. Liu, W. Xie, J. Guo, D. Kinghorn, L. Wu, Q.-X. Ji, T. J. Kippenberg, K. Vahala, and J. E. Bowers, *Integrated turnkey soliton microcombs*, *Nature* **582** (2020), no. 7812 365–369.

[8] D. J. Moss, R. Morandotti, A. L. Gaeta, and M. Lipson, *New cmos-compatible platforms based on silicon nitride and hydex for nonlinear optics*, *Nature Photonics* **7** (07, 2013) 597.

[9] Y. Xuan, Y. Liu, L. T. Varghese, A. J. Metcalf, X. Xue, P.-H. Wang, K. Han, J. A. Jaramillo-Villegas, A. A. Noman, C. Wang, S. Kim, M. Teng, Y. J. Lee, B. Niu, L. Fan, J. Wang, D. E. Leaird, A. M. Weiner, and M. Qi, *High-q silicon nitride microresonators exhibiting low-power frequency comb initiation*, *Optica* **3** (Nov, 2016) 1171–1180.

[10] X. Ji, F. A. S. Barbosa, S. P. Roberts, A. Dutt, J. Cardenas, Y. Okawachi, A. Bryant, A. L. Gaeta, and M. Lipson, *Ultra-low-loss on-chip resonators with sub-milliwatt parametric oscillation threshold*, *Optica* **4** (Jun, 2017) 619–624.

[11] J. Liu, G. Huang, R. N. Wang, J. He, A. S. Raja, T. Liu, N. J. Engelsen, and T. J. Kippenberg, *High-yield wafer-scale fabrication of ultralow-loss, dispersion-engineered silicon nitride photonic circuits*, *arXiv* **2005.13949** (2020).

[12] Z. Ye, K. Twayana, P. A. Andrekson, and V. Torres-Company, *High-Q Si_3N_4 microresonators based on a subtractive processing for kerr nonlinear optics*, *Opt. Express* **27** (Nov, 2019) 35719–35727.

[13] H. Jung, K. Y. Fong, C. Xiong, and H. X. Tang, *Electrical tuning and switching of an optical frequency comb generated in aluminum nitride microring resonators*, *Opt. Lett.* **39** (Jan, 2014) 84–87.

[14] X. Liu, Z. Gong, A. W. Bruch, J. B. Surya, J. Lu, and H. X. Tang, *Iii-nitride nanophotonics for beyond-octave soliton generation and self-referencing*, *arXiv* **2012.13496** (2020).

[15] Y. He, Q.-F. Yang, J. Ling, R. Luo, H. Liang, M. Li, B. Shen, H. Wang, K. Vahala, and Q. Lin, *Self-starting bi-chromatic linbo3 soliton microcomb*, *Optica* **6** (Sep, 2019) 1138–1144.

[16] C. Wang, M. Zhang, M. Yu, R. Zhu, H. Hu, and M. Loncar, *Monolithic lithium niobate photonic circuits for kerr frequency comb generation and modulation*, *Nature Communications* **10** (2019), no. 1 978.

[17] Z. Gong, X. Liu, Y. Xu, and H. X. Tang, *Near-octave lithium niobate soliton microcomb*, *Optica* **7** (Oct, 2020) 1275–1278.

[18] M. Pu, L. Ottaviano, E. Semenova, and K. Yvind, *Efficient frequency comb generation in algaas-on-insulator*, *Optica* **3** (2016), no. 8 823–826.

[19] L. Chang, W. Xie, H. Shu, Q.-F. Yang, B. Shen, A. Boes, J. D. Peters, W. Jin, C. Xiang, S. Liu, G. Moille, S.-P. Yu, X. Wang, K. Srinivasan, S. B. Papp, K. Vahala, and J. E. Bowers, *Ultra-efficient frequency comb generation in algaas-on-insulator microresonators*, *Nature Communications* **11** (2020), no. 1 1331.

[20] G. Moille, L. Chang, W. Xie, A. Rao, X. Lu, M. Davanço, J. E. Bowers, and K. Srinivasan, *Dissipative kerr solitons in a iii-v microresonator*, *Laser & Photonics Reviews* **14** (2020), no. 8 2000022.

[21] D. J. Wilson, K. Schneider, S. Hönl, M. Anderson, Y. Baumgartner, L. Czornomaz, T. J. Kippenberg, and P. Seidler, *Integrated gallium phosphide nonlinear photonics*, *Nature Photonics* **14** (2020), no. 1 57–62.

[22] D. M. Lukin, C. Dory, M. A. Guidry, K. Y. Yang, S. D. Mishra, R. Trivedi, M. Radulaski, S. Sun, D. Vercruysse, G. H. Ahn, *et. al.*, *4h-silicon-carbide-on-insulator for integrated quantum and nonlinear photonics*, *Nature Photonics* **14** (2020), no. 5 330–334.

[23] F. Gyger, J. Liu, F. Yang, J. He, A. S. Raja, R. N. Wang, S. A. Bhave, T. J. Kippenberg, and L. Thévenaz, *Observation of stimulated brillouin scattering in silicon nitride integrated waveguides*, *Phys. Rev. Lett.* **124** (Jan, 2020) 013902.

[24] J. Liu, G. Huang, R. N. Wang, J. He, A. S. Raja, T. Liu, N. J. Engelsen, and T. J. Kippenberg, *High-yield, wafer-scale fabrication of ultralow-loss, dispersion-engineered silicon nitride photonic circuits*, *Nature Communications* **12** (2021), no. 1 1–9.

[25] J. Liu, E. Lucas, A. S. Raja, J. He, J. Riemensberger, R. N. Wang, M. Karpov, H. Guo, R. Bouchand, and T. J. Kippenberg, *Photonic microwave generation in the x- and k-band using integrated soliton microcombs*, *Nature Photonics* (2020).

[26] Z. Ye, K. Twayana, P. A. Andrekson, *et. al.*, *High-Q Si_3N_4 microresonators based on a subtractive processing for kerr nonlinear optics*, *Optics Express* **27** (2019), no. 24 35719–35727.

[27] K. Wu and A. W. Poon, *Stress-released Si_3N_4 fabrication process for dispersion-engineered integrated silicon photonics*, *Optics Express* **28** (2020), no. 12 17708–17722.

[28] M. H. P. Pfeiffer, A. Kordts, V. Brasch, M. Zervas, M. Geiselmann, J. D. Jost, and T. J. Kippenberg, *Photonic damascene process for integrated high-q microresonator based nonlinear photonics*, *Optica* **3** (2016), no. 1 20–25.

[29] M. H. P. Pfeiffer, C. Herkommer, J. Liu, H. Guo, M. Karpov, E. Lucas, M. Zervas, and T. J. Kippenberg, *Octave-spanning dissipative kerr soliton frequency combs in Si_3N_4 microresonators*, *Optica* **4** (Jul, 2017) 684–691.

[30] M. H. P. Pfeiffer, J. Liu, A. S. Raja, T. Morais, B. Ghadiani, and T. J. Kippenberg, *Ultra-smooth silicon nitride waveguides based on the damascene reflow process: fabrication and loss origins*, *Optica* **5** (Jul, 2018) 884–892.

[31] J. Liu, A. S. Raja, M. H. P. Pfeiffer, C. Herkommer, H. Guo, M. Zervas, M. Geiselmann, and T. J. Kippenberg, *Double inverse nanotapers for efficient light coupling to integrated photonic devices*, *Opt. Lett.* **43** (Jul, 2018) 3200–3203.

[32] C. Xiang, J. Liu, J. Guo, L. Chang, R. N. Wang, W. Weng, J. Peters, W. Xie, Z. Zhang, J. Riemensberger, *et. al.*, *Laser soliton microcombs on silicon*, *arXiv preprint arXiv:2103.02725* (2021).

[33] W. Liang, D. Eliyahu, V. S. Ilchenko, A. A. Savchenkov, A. B. Matsko, D. Seidel, and L. Maleki, *High spectral purity kerr frequency comb radio frequency photonic oscillator*, *Nature Communications* **6** (08, 2015) 7957.

[34] P. Marin-Palomo, J. N. Kemal, M. Karpov, A. Kordts, J. Pfeifle, M. H. P. Pfeiffer, P. Trocha, S. Wolf, V. Brasch, M. H. Anderson, R. Rosenberger, K. Vijayan, W. Freude, T. J. Kippenberg, and C. Koos, *Microresonator-based solitons for massively parallel coherent optical communications*, *Nature* **546** (06, 2017) 274.

[35] D. T. Spencer, T. Drake, T. C. Briles, J. Stone, L. C. Sinclair, C. Fredrick, Q. Li, D. Westly, B. R. Ilic, A. Bluestone, *et. al.*, *An optical-frequency synthesizer using integrated photonics*, *Nature* **557** (2018), no. 7703 81–85.

[36] Y.-H. Lai, M.-G. Suh, Y.-K. Lu, B. Shen, Q.-F. Yang, H. Wang, J. Li, S. H. Lee, K. Y. Yang, and K. Vahala, *Earth rotation measured by a chip-scale ring laser gyroscope*, *Nature Photonics* **14** (2020), no. 6 345–349.

[37] Z. L. Newman, V. Maurice, T. Drake, J. R. Stone, T. C. Briles, D. T. Spencer, C. Fredrick, Q. Li, D. Westly, B. R. Ilic, *et. al.*, *Architecture for the photonic integration of an optical atomic clock*, *Optica* **6** (2019), no. 5 680–685.

Chapter 6

Future directions

6.1 Lasers heterogeneously integrated with ultra-low-loss waveguides

The progress discussed in this thesis with regard to active-passive integration provides a new degree of freedom to engineer the integrated photonic devices performance. Si_3N_4 with superior passive properties offers ultra low loss and high temperature stability which are critical in a series of laser properties. Higher-power, lower-noise, higher-stability lasers can be constructed.

This thesis already demonstrated semiconductor lasers heterogeneously integrated with Si_3N_4 -DBR cavity and self-injection locked with high-Q Si_3N_4 ring resonator. Obviously, they are not tunable lasers yet and it's straightforward to achieve tunable lasers using the Si_3N_4 cascaded ring resonators discussed in the Chapter 2. With modified ring diameters, the three-ring designs could enable over 100 nm tuning range. Together with the low loss of Si_3N_4 waveguide, absence of nonlinear loss and lower thermal noise than Si, this could result in widely-tunable ultra-narrow linewidth semiconductor lasers with

high output power.

Regarding the self-injection locking scheme which results in the lowest linewidth to date, there is still a lot of room for heterogeneously integrated laser to improve. The Si_3N_4 ring resonator Q-factor can be further increased and the mode volume can be increased by using larger ring radius to have lower thermorefractive noise. With all these improvements, heterogeneously integrated laser could achieve have better performance than hybrid integrated counterparts. There are two factors that are important. First, for heterogeneously integrated laser, the free-running laser without self-injection locking could be a narrow-linewidth laser thus it will be less noisy than the monolithic III-V DFB laser used in hybrid integration. Second, the coupling loss from the laser to the resonator is much lower in heterogeneously integrated laser due to efficient Si-Si_3N_4 taper, which results in much higher backscatter intensity than the butt-coupling used in hybrid integration. These factors are beneficial to have even narrower linewidth. But significant work has to be done to improve the Q-factor of ultra-high-Q ring resonators used in heterogeneously integrated lasers. And the III-V laser process needs to be modified or investigated to maintain the ultra-high-Q factor of ring resonators that are fabricated at the front-end of fabrication process.

6.2 Heterogeneously integrated microcomb

The demonstrated heterogeneously integrated soliton microcomb device is the first demonstration of such devices on a monolithic substrate. This could form as the prototype basis of such devices in the future. For such devices, the high laser power and high Q-factors are always most important deciding factors.

For the laser power, a low contact resistance is important. The current demonstrated device is still limited by the contact resistance and one order improvement is expected

to yield higher laser power less heating. The gain section 1.8 mm can also be modified for high gain. The epi currently used is 3-QW InAlGaAs which was developed for lower noise than 5-QW or 8-QW epis. Thus, if higher gain is the target, the epi design can be changed accordingly. More opportunities include switching to QD-based laser gain epis which are well known for high gain, high power output. However, this has to be based on applications since QD epi are mostly based on InAs/GaAs operating in the telecom O-band.

Higher Q-factors are expected by further engineering the material quality as recent investigations show that the thick-Si_3N_4 ring resonator absorption-limited Q-factor is as high as 200 million. As the comb generation threshold is inversely proportional to Q^2, a higher Q-factor could lead to higher power in the lines and wider comb spectra.

Semiconductor amplifiers can be included between the laser and the the resonator to boost the power but the dynamics of self-injection locking with an SOA needs to be investigated for such configurations.

Heterogeneously integrated microcombs open up new possibilities as now optical Kerr frequency comb sources can be incorporated as a building block into mature heterogeneous silicon photonic platforms. Thus more functionalities including modulation, photodetection, filtering and so on can be applied to generated soliton microcombs. A wide variety of new devices with the capability to generate, manipulate and analyze the microcombs are becoming possible and will be one of the research focus for the next-generation photonic integrated circuits.

Appendix A

Fabrication process of heterogeneous integrated laser on silicon nitride

The heterogeneous Si_3N_4 laser fabrication begins with a thermally grown SiO_2 layer (8 textmu m thick) on a 100-mm diameter Si wafer. Low-pressure chemical vapor deposition ((LPCVD)) deposits a 90-nm thick stoichiometric Si_3N_4 layer. Si_3N_4 waveguide patterning and Si_3N_4 grating fabrication was carried out uSi_3N_4g 248-nm DUV lithography, followed by $CHF_3/CF_4/O_2$ inductively coupled plasma (ICP) etching. The first layer of waveguide cladding is formed by depositing deuterated SiO_2 of 900 nm on top of the Si_3N_4 waveguides.

Chemical-mechanical-polishing (CMP) is used to planarize this cladding layer, resulting in a cladding thickness of about 600 nm. USi_3N_4g oxygen-assisted plasma-activated bonding, a large silicon on insulator (SOI) piece (50 mm x 50 mm) is bonded on the wafer covering areas inlcuding InP/Si and Si_3N_4 photonic circuits. Mechanical lapping and Si Bosch etching are used to remove the Si substrate. With buffered hydrofluoric acid (BHF), the buried oxide layer is removed. DUV stepper and C_4F_8/SF_6 based reactive-ion etching are used to pattern Si waveguides (RIE). Si waveguide etch includes 231 nm-deep etched Si rib waveguide etch, 269-nm thin-core Si waveguide taper etch and 500-nm deep silicon vertical outgasSi_3N_4g channels etch. Following the formation of the Si waveguide,

InP multiple quantum well (MQW) epi is bonded to the laser gain area, followed by mechanical lapping of the InP substrate and HCl acid etching the InP substrate.

The p-InGaAs layer is where the acid wet etching of the substrate stops. $CH_4/H_2/Ar$ based dry etching and H_3PO_4 based wet etching are used to create the InP laser mesa. XeF_2 isotropic gas etch removes excess Si on top of Si_3N_4 photonic circuits. After that, the laser is passivated by 900-nm thick deuterated SiO_2, which also serves as the second layer of Si_3N_4 waveguide cladding. Then, uSi_3N_4g electron-beam deposition and a lift-off process, N-contact metal (Pd/Ge/Pd/Au) and P-contact metal (Pd/Ti/Pd/Au) are deposited. The contact metal formation is followed by proton implantation. The metal for the heater and probe is then deposited and lift-off. The Si_3N_4 inverse taper facet is revealed for laser characterization after the laser chips are diced and polished.

The detailed fabrication process with cross-sectional view is shown in Fig. A.1.

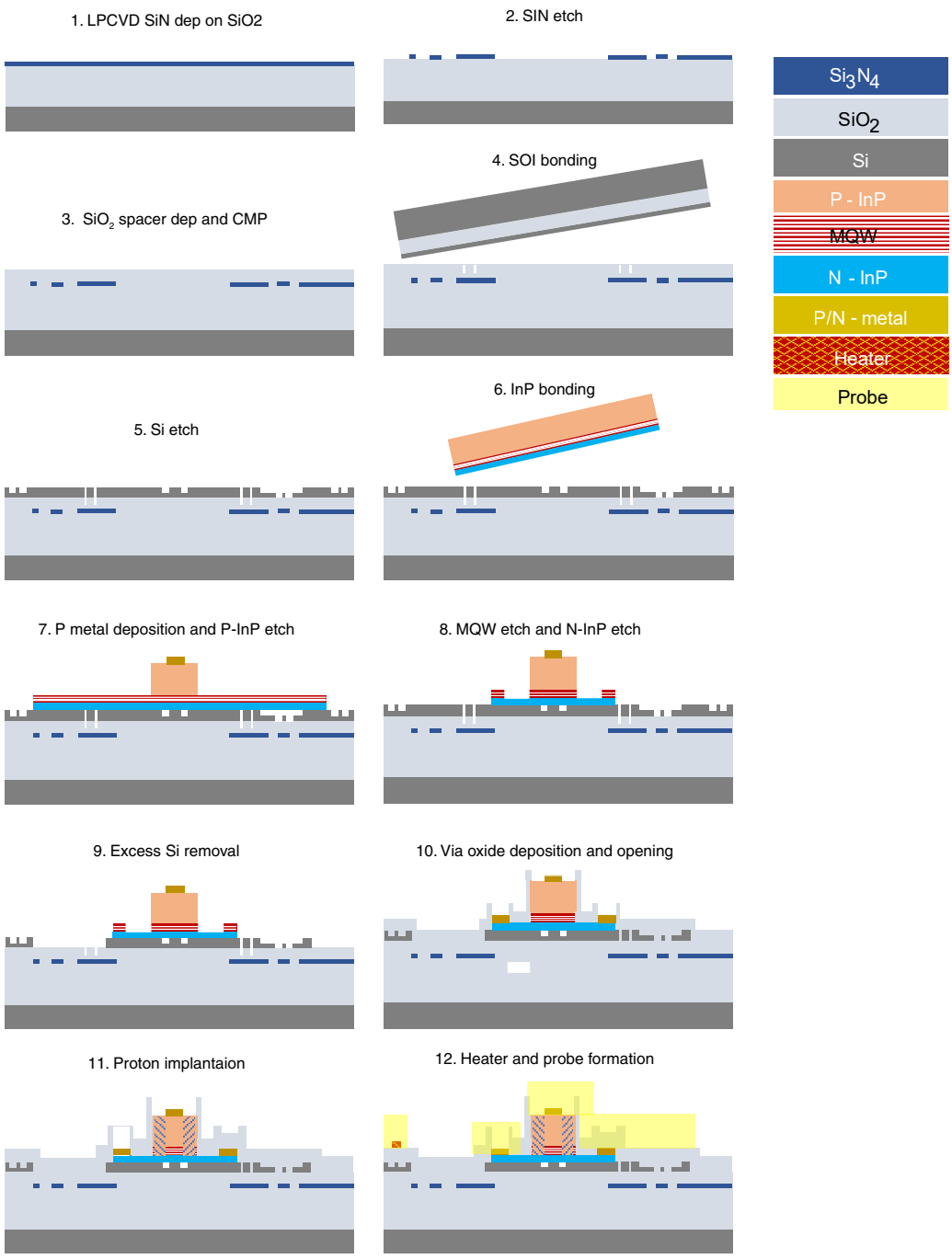

Figure A.1: Cross-sectional view of the heterogeneous laser on Si_3N_4 fabrication process.